REGENERATED SPIDER SILK AS A NEW BIOMATERIAL FOR MICRO-ELECTRO-MECHANICAL SYSTEMS (MEMS) APPLICATIONS

by

JIAMEI BAI

B. Sc., The University of Waterloo, 2004

A THESIS SUBMITTED IN PARTIAL FULFILLMENT OF THE REQUIREMENTS FOR THE DEGREE OF

MASTER OF APPLIED SCIENCE

in

THE FACULTY OF GRADUATE STUDIES

(Mechanical Engineering)

THE UNIVERSITY OF BRITISH COLUMBIA

JUNE 2006

ABSTRACT

The objective of this research is to characterize properties of spider silk in a thin film form and apply it as a new biomaterial for MEMS devices. This research represents a relatively new area of study. Most research to date on spider silk has focused on its fiber form, thus there is a limited understanding of this silk as a film. Furthermore, using spider silk for MEMS applications has never before been realized.

In this study, spider silk was manipulated into a solution and spin coated onto a silicon substrate to form a thin film. A microfabrication technique was then developed to create a free standing microbridge structure. Mechanical properties of the film were obtained by both nanoindenting the film on silicon substrate, and by fracture testing of the microbridge.

Once these mechanical properties were obtained, the magnetic properties were added to the spider silk film to add more functionality to the material. This was done by blending the film with ferromagnetic materials such as Ni and Fe. First, micron sized Ni particles were mixed into the spider silk solution. Using the microfabrication technique developed earlier in this research, cantilever beam were formed from the Ni spider silk material. Studying the magnetic properties of these cantilever beams showed that these beams are susceptible to external magnetic field. Static and dynamic testing of the cantilever beam was performed.

Second, iron pentacarbonyl was mixed with spider silk solution to form an iron spider silk composite. By studying this composite, a new property of spider silk is discovered. Specifically, it was found that by varying the concentration of the spider silk solution and maintaining the same amount of iron pentacarbonyl, the concentration of iron in the final film varied drastically. Most interestingly, nano spheres with diameter size between 150 – 650 nm were formed in this manner. It was found that they consisted of spider silk proteins and low concentration of iron.

In conclusion, this study has provided several preliminary findings regarding the properties of spider silk that have never been revealed before. As well, the fabrication techniques developed in this study can be used as a stepping stone for a more advanced microfabrication processes in the future. MEMS devices such as micro sensors, actuators, and biomembranes are just some of the possible applications that may result from this research. The continuation of this research will offer new options for biomaterials used with MEMS technology, where a high degree of toughness, strength, biocompatibility and biodegradability are required.

TABLE OF CONTENTS

LIST OF TABLES

LIST OF FIGURES

ACKNOWLEDGEMENT

I would like to thank my supervisor Dr Mu Chiao for encouraging and supporting me throughout my Masters degree. I could not have finished without his guidance. I would also like to thank my committee members, Dr. Winnie Chu and Dr. Rizhi Wang. They have helped me tremendously in coming up with solutions and new approaches to problems. They were instrumental in helping me understand various new topics that would had otherwise been much more difficult to grasp.

A great appreciation goes out to the lab technicians who were key in understanding experimental results and making the experiments successful. These special people include Tim Ma, Tom Barnjak and Mary Mager. In addition, I would like to thank our MEMS lab members as well as our summer student Ramin for being such wonderful team players.

A special thanks to my partner in crime Brandon, for comforting me when I'm stressed and taking on most than his share of the house duties.

I would like to acknowledge that this project is supported in part by the Canada Research Chairs Program, Canada Foundation for Innovation and the Natural Sciences and Engineering Research Council of Canada (NSERC) Discovery Program.

Finally, I would like to dedicate this thesis to my parents, who had work so hard to provide me with these wonderful opportunities in life.

CHAPTER 1

Introduction

1.1 Background

One of the strongest natural fibers known to man is the spider's silk. Its combination of high strength and elasticity has opened up an area of study in silk fibers. By learning about its remarkable properties, we can apply them in a wide range of applications (including possible MEMS applications) and mimic them for development of new synthetic biopolymers.

One of the ways spider silk is studied is through analysis of regenerated spider silk. However, the mechanical properties of the two types of silk are not identical. Unlike native spider silk fibers, regenerated spider silk is first harvested from spiders, then dissolved into solvents and re-spun through an orifice. Mechanical properties of the regenerated silk, such as the toughness, are largely dependent on the assembling process of the proteins during the drying process. Therefore, in general, regenerated spider silk material properties are inferior to those of natural silk fibers.

Traditionally, MEMS research has been conducted using polymeric materials such as Polymethylsiloxane (PDMS) and hydrogel to fabricate micromechanical components, such as microfluidic valves and micropump diaphragms. However, the mechanical strength of conventional biopolymer has been unsatisfactory for many biomedical applications [8].

One possible important use for spider silk is as a biomembrane for bioMEMS applications.

However, a limited amount of previous work on spider silk in a film form has been performed. Further more, no study has ever focused on application of the film in MEMS areas.

One work of note on a different type of silk fiber is one performed by *Jin, et. al.*, where *Bombyx Mori* (a type of silk worm) silk fibroins were used to form a composite by blending the silk with PEO (Poly-ethylene-oxide) [91]. In this study, the authors found that pure fibroin film in a dry state is too brittle, but that elasticity could be improved by blending it with other materials. Definable porous film could also be generated by controlling the extraction of the PEO phase. Mechanical testing showed that by increasing the PEO, the elongation increased while the breaking strength decreased. In the end, a slight improvement in toughness was found. So, while this study clearly manipulated the silk worm silk to improve certain desired material properties, it is still not clear whether spider silk would have similar response under the same conditions.

Only two recent published works have actually focused on spider silk films. In those studies, a film was made by spin coating recombinant spider silk proteins which were synthesized in both E-coli [92] and transgenic tobacco plants [93]. *Bombyx Mori* silk was also purified and used to form a film with the same process. Cast film was also formed using a glass ring and plate setup [93]. In study performed by *Junghans et. al.* [93], FTIR results showed a minor influence of the preparation procedures on the final layers. Dynamic microhardness tests were also performed to characterize the film mechanical properties. Recombinant spider silk film was found to have elastic modulus value of 5.5 – 6.3 GPa, and hardness of 230 Nmm^{-2}. Silk worm film had a significantly lower elastic modulus of 491 MPa and hardness of 15 Nmm^{-2}.

1.2 Research Objectives

The objective of the present research is to study and characterize regenerated spider silk in a film form. This study utilizes natural spider silk fibers, instead of recombinant fibroin proteins. Once the mechanical properties of the film are determined, fabrication techniques can be developed to obtain simple microstructures using spider silk film. Finally, by manipulating the film and forming composites consisting of spider silk and ferromagnetic materials, new biocompatible and biodegradable materials can be developed for magnetic actuations in bioMEMS devices. This will open up a new field of study and application for spider silk and fill a void in the research of biomaterials for MEMS.

1.3 Thesis Outline

The thesis is structured as follows.

Chapter 1: Introduction to motivation behind the project. A few similar studies are reviewed and the objective of this thesis is stated.

Chapter 2: Literature review on spider silk. This includes basic biological makeup of spider silk and mechanical properties previously obtained in other studies. It also includes work showing the effects of different conditions, such as solvents or spinning methods that alter the final properties of spider silk.

Chapter 3: Fabrication method of thin film of regenerated spider silk on silicon substrate. Mechanical testing of the film using nano indentation technique is used to obtain properties in elastic modulus, hardness and viscoelasticity. A simple microfabrication technique is developed for the film to obtain free standing microbridges. Fracture testing is performed on the microbridge to obtain the ultimate tensile strength.

Chapter 4: Micron size Ni particles are mixed with the regenerated spider silk film to obtain a new composite. Using microfabrication method previously developed, a free standing Ni beam can be made. Properties such as magnetic hysteresis loop, stress vs. strain curve, and magnetic field vs. bending of the beam are all demonstrated. This shows a complete new method of obtaining magnetically actuated and biocompatible cantilever beams.

Chapter 5: By mixing iron pentacarbonyl with regenerate spider silk, iron can be impregnated into the spider silk film to form a new magnetic composite biomaterial. A fabrication method is developed and outlined in this chapter. By varying the dilution of the regenerated spider silk, three different types of materials are found. They vary in appearance, as well as iron concentration. This illustrates a new method of manipulating the spider silk, not only to mix with iron to form ferromagnetic composite, it also to show how spider silk protein binds to iron under different conditions.

Chapter 6: Conclusion and recommendation for future works.

CHAPTER 2

Literature Review

Spider silk is one of the most attractive biomaterial that is yet to be applied in wider practice. Many studies have shown its amazing high elasticity and high strength which results in incomparable toughness. It is the strongest natural material known, and only a few synthetic materials can compete with it. For example, Kevlar is most famous for its own high modulus value and outstanding mechanical properties. Even though its strength is 4 times larger in comparison to spider silk, the energy required to break Kevlar is only 1/3 of spider silk. This is due to spider silks' ability to allow more extension to abort the energy before rupturing [1].

The strength and elasticity of spider silk lends itself to numerous potential applications such as artificial ligaments or tendons, surgical sutures or biodegradable membranes and bullet proof vests. However, there have been many problems in mass producing the spider silk through mimicking farming techniques used for silkworms. Unlike sheep or silkworms, spiders cannot be penned in together or raised as a group. This in combination with their territorial and cannibalistic nature makes them hard to domesticate.

Much work has been done to obtain spider silk genomes by various means. Using the gene synthesis approach, recombinant protein has been generated through transgenic tobacco and potato plants. [2] It has also been reported that Nexia technology Inc. has successfully inserted genes from spider silk into mammals such as goats to produce the protein in their milk. The proteins are then isolated and purified for subsequent spinning into fibers [3, 4]. Nexia foresees tapping into the $500 million market for fishing materials as well as the $1.6 billion market for

industrial fibers in the near future [5]. It has also drawn attention of the US military where it has a potential of building an entire armors vest out of goat silk. Due to its light weight and toughness, the spider silk vest can perform its bullet stopping functionalities, while reducing the load that a soldier has to carry.

2.1 Biological make up of spider silk

Due to its attractive properties, spider silk has been intensely studied around the world. The silk emerges from the body as a liquid and form a single thread by the spinnerets on the underside of the spider abdomen. The amino acid sequence of two different, but similar fibroins builds up the silk fibers [6]. The main amino acids contained in the fibroins are glycine and alanine.

In the secondary structure of these proteins, regions of the alternating gly-ala sequences organize into β-sheets which form the core of crystalline structures held together by hydrogen bonds. This is said to be responsible for its high strength. The glycine rich regions produces a spiral shaped sequence that is less ordered, and it is this combination of crystalline and amorphous regions that are responsible for the strength and extensibility of the silk [7-9].

2.2 Material property of native spider silk

In general, orb-web spiders have in total, 7 different glands that produce silk. Every spider contains at least 3 of these types, and they are used in different applications such as draglines, swathing silk or for constructing the egg sac. Among these orb-weavers, the most frequently studied dragline silk comes from the golden orb-weaver breed of *Nephila Clavipes* and *Araneus diadematus*. This is due to its availability and outstanding mechanical properties. Usually, 150 yards of silk per spider can be collected. It would take the work of 415 spiders to make a square yard of cloth [10]. In table 1 below is a list for comparison between natural fibers and several high performance synthetic materials [11].

Table 1: Comparison between natural fibers and high performance synthetic materials [11]

Fiber Type	Density (g/cm^3)	Modulus of Elasticity E (GPa)	Tensile Strength (GPa)	Breaking Strain (%)	Resilience (MJ/m^3)
Spider silk *Nephilas Clavipes*	1.3	1-10	1.8	30	130
Silkworm Silk *Bombyx mori*	1.3	5	0.6	12	50
Nylon 6.6	1.1	5	0.9	18	80
Kevlar 49	1.4	130	3.6	3	50
Steel	7.8	200	3	2	6

Dragline silk of the golden orb weaver has an elastic modulus starting from 10 GPa, elongation to break of 15-30%, and tensile strength of 1.1-1.4 GPa. This however depends on the environmental factor, strain rate and method in which the fibers were obtained. Even though, the tensile strength is similar to that of stainless steel, spider silk is less than 1/3 in density, thus, in weight comparison, it is much stronger.

Spider silk's viscoelastic property has been reported to approach that of rubber [12, 13]. Since rubber is considered a non-linear material, typical method of obtaining some mechanical properties from stress-strain curve can not be applied.

2.3 Material property of regenerated spider silk

Regenerated spider silk has been used to study the self assembling nature of the spider silk proteins. As previously mentioned, it has been shown that the amino sequence and alignment of the proteins greatly affect the mechanical properties of spider silk. Thus, significant work has been done examining this self assembly process. The results of the spider silk was found to be approximately 1/3 of the original (table 2) [14].

Table 2: Comparison between native and regenerated *N.Clavipes* spider silk

	Elastic Modulus (GPa)	Tenacity (GPa)	Strain break (%)
Dragline of *N.Clavipes*	22	1.3	12
Regenerated silk of *N. Clavipes*	8	0.32	

2.4 Silk as a biomaterial

Study of local tolerance and biocompatibility has been tested for spider silk and silk worm materials. Using pigs as test subjects, 4 different types of spider silk were tested while being compared to typical synthetic materials such as polyurethane film, gauze pads and collagen dressings. The study demonstrated that animal tissue tolerates natural and untreated spider silk in ways comparable to routine surgery materials. It embodies biodegradability and immunotolerance that equals typical implantables commonly used [15].

2.5 Effect of spinning on spider silk

The process where spiders make their mechanically superior fiber involves the removal of solvent (water) from a concentrated protein solution while the solution flows through a progressively narrowing spinning canal [16]. Although, much work has been established in understanding the genetic make up of the proteins, the actual spinning process remains undefined. However, it is understood that the mechanical properties depend on the spin of the silk [17]. It has been shown that a combination of the aqueous environment and stretching can produce a wide range of tensile properties [18]. Work has also been performed in modeling the water removal under the assumption that the rapid diffusion of water through the canal wall occur throughout the spinning canals. Since, the artificial spinning process has not be able to mimic similar methods, manufactured spider silk spun from silk protein remain to be less in turns of mechanical properties [3, 19].

2.6 Effect of solvent on spider silk

One of the main features of spider silk is its supercontraction behaviour when submerged into solvents, especially water [20]. Supercontraction is referred to as a large shrinkage in water at room temperature of silk fibers, and it is first observed by *Work* [21]. Similar behaviours have been shown in artificial polymers when emerged in organic solvents or under thermal conditions

that causes shrinkage [20, 22]. It has been shown that water ruptures the hydrogen bonds between the amino acids and carboxyl group and thus produces swelling in radial direction, and supercontraction in fiber length [6]. This effect is also called plasticisation where the plasticiser insinuates itself into the polymer and reduce the interaction between the polymer chains [20].

In work related to supercontraction, *Shao* and *Vollrath* [20] had shown that polar solvents strongly affect the mechanical behaviour of several of the bench mark dragline silks, ex *Nephila, Araneus*. With an increase in solvent polarity, Young's modulus and breaking strength decreases, where elongation increases slightly. They have also shown in recent work, [22] that there is a correlation between variability in mechanical properties such as initial modulus and breaking strain and its ability to supercontract. Both properties are dependent on the hydrogen-bonded amorphous, yet oriented area of the silk.

When unstrained, the silk generally shrink to 50-60% of its originally length [23, 24]. When strained, a supercontraction stress is build up in the fiber. When measured using relative humidity (RH) and the stress found in the fiber, a transition point at 70 -75& RH is noted. Once relative humidity has reached this point for around 60 second, a jump in supercontraction stress can be experienced [23]. A lower supercontraction force is found in naturally produced fiber in comparison by forced silking [25]. However, this difference in supercontraction behaviour can be used to manipulate silk obtained from forced silking. When the supercontraction length is restricted to 7.5-25%, the mechanical stress-strain of the forced silk becomes similar to those of naturally spun silk [23].

2.7 Other environmental effect on spider silk

Temperature

Spider silk fiber had shown remarkable increase in strength and elongation when temperature is cooled down to -60C°. This property had not been observed in most synthetic fibers. When the fiber is heated up to 150 C°, little change in tensile behaviour is observed. However, the elongation at break decreases with an increase in temperature up to a minimum at 70 C°. [26].

UV

UV rays have been shown to decompose protein molecules of natural silks such as silkworm silks. Since spider silk captures insects in daytime, the exposure to sunlight may have effect on the mechanical strength of spider silk webs. Experiments were carried out by *S. Osaki* [27] to test the effect of 3 ranges of UV light on spider silk.

They found that Dragline samples kept under no UV irradiation had no changes in breaking stress (BS) over period of 3 months. When exposed to UV rays, with increase in UV range (going from 200-400 nm), an increase in BS is shown. When looking at the mechanical BS, the time dependence of UV irradiation was also shown to be optimal at higher wavelengths. However, the peak BS occur for higher wavelength (320-400 nm) peaked at around 8 hrs, and then continue to decrease as irradiation time increases. This indicates that UV exposure also decompose the material after an optimal irradiation time has passed.

CHAPTER 3

Spider Silk as a New Biomaterial for MEMS

Mechanical strength of conventional biopolymers is unsatisfactory for many biomedical applications [8]. As one of the strongest natural materials, spider drag-line silk is introduced for the first time as a new biomaterial for Micro-Electro-Mechanical Systems (MEMS). The tasks accomplished in this chapter are focused on mechanical characterization of regenerated spider silk under two conditions: (1) spin-coated thin film formed onto a silicon substrate; (2) formation of a free-standing microbridge (800 x 800 x 40 μm^3) obtained by a surface micromachining process. Micro-mechanical testing using a nano indentation machine showed the spider silk film having an elastic modulus of 7.3 GPa, a loss tangent of 0.044 and an ultimate tensile strength of 85.1 MPa.

3.1 Thin Film Spider Silk

3.1.1 Experimental Methods

Thin-film spider silk is formed onto a substrate. The thin-film spin-on processing technique can be easily adopted by MEMS industry for batch fabrications. The Spider drag-line silk is first harvested from the golden orb weaving spider *N. clavipes* from central Florida. The silking technique is in a manner similar to the procedure described by *Work* and *Emerson* [28]. The cut silk samples are provided in courtesy of Dr Carl Michal from the department of Physics, UBC. The actual method of silking are briefly stated here.

Two or three times a week, the spiders are taped down to a plate as depicted in Figure1. All of the spider legs are retrained to prevent interference with the silking collection process. The draglines usually protrude from the backside spinneret, and this initiate the pulling process. If none is visible, gently stimulating the spinneret with tweezers usually produces dragline. The silk is then wrapped around the mandrel for continuous silking. From viewing through the dissecting microscope, the minor ampullate silk is prevented from contaminating the dragline silk by separating the two and taping the ampullate silk aside. The drawing of the silk is completed at a rate of 2-4 cm/sec. The spider is fed before, during and after the silking process, as well as on non-silking days.

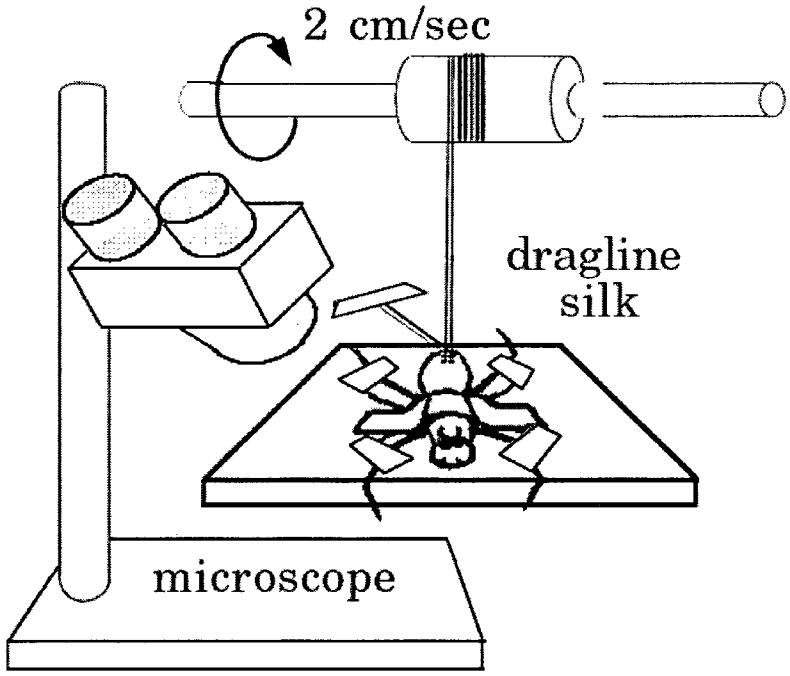

Figure 1: Extraction of silk samples. (Courtesy of D. Hijirida)

The spider is fed with Dubellos' modified Eagle Medium (Gibco) enriched with 10% w/v L-alanine-3,3,3-$^{2}H_{2}$ (Cambridge Isotopes Labs, Andover, MA).

The silk was dissolved in a 1,1,1,3,3,3 hexafluoro-2-propanol (HFIP) solution (Sigma-Aldrich) with a ratio of either 1% w/w or 0.5% w/w [29]. For example, if 1 mg of raw spider silk is used,

given the density of the solvent is 1.596 g/cc, the amount of solvent that is required for mixing with the fibers is calculated as follows:

1 mg = 0.001 g = 1% of final solution

Total mass of solution = 0.001 / 1% = 0.1 g

(0.1 g – 1 mg) / 1.596 g/cc = 0.062 cc = **62 μl**

Formic acid has been previously reported as a solvent that dissolves spider silk [30]. However, there are several disadvantages to using this solvent. First, it is a strong and much more toxic acid which is much harder to handle than HFIP (which is an alcohol). Secondly, formic acid dries slower than HFIP. This longer drying process may provide more opportunity for abnormal behaviors during formation of the membrane. We could counteract this by using heating/oven to speed up drying. However, this process will alter the material since spider silk is sensitive to temperature [26].

A number of other solvent has also been tested to see whether or not it can dissolve spider silk. The test is performed by putting one 5 μl droplet of 1%w/w spider silk solution (dissolved in HFIP) on a glass plate. This droplet is then mix with 5 μl droplet of the solvent under question. If the mixture becomes cloudy, precipitation occurs, and the spider silk is therefore not soluble in this particulate solvent. None of the five solvents tested were successful. Table 3 tabulates the findings. Please note that perhaps the volume added reached saturation point for the solvent, therefore resulted in precipitation. Due to small reserve of silk, we could not perform test with raw silk with all the solvents.

3.1.1.1 Thin film experiment parameters

The solution was allowed to dissolve for approximately 24 hours at ambient temperature before spin-coating onto a silicon wafer. A 10 μl droplet was spun at approximately 500 rpm for 30 seconds. It was then air dried for further thin-film mechanical measurements.

Parameters involved in the thin film preparation process were initially tested.

Table 3: Solubility test for spider silk with 5 possible solvents

SOLVENT	RESULTS
Acetonitile	The droplets on the edges showed definite separation of the two solvents, droplets formed in the center of the membrane did mixed and formed cloudy film immediately
Methanol	Slightly cloudy, better than Acetonitile, part of the droplet stayed on top of the film, and did not dissolve.
Isopropanol	Cloudy
Methanol Chloride	Cloudy
Chloroform	Slightly cloudy

1. Length of time needed for dissolving the spider silk

By eye inspection, the spider silk was completely dissolved in approximately 50 minutes. When waited over night, no significant difference can be seem in the solution. However, the thin film formed using the over night sample appear to be slightly smoother then the ones formed using the shorter mixing time. Both film had ripple like surface, which will be shown in figures later on the chapter.

2. Spin coating speed

1% w/w solution was first used. When no spin coating was performed - simple droplet formed on silicon substrate – it resulted in a coffee stain like surface, where the darker ring on the outer edges can be seemed. When spin coating was introduced at 500-750 rpm, the surface appeared to be smoother; the shape appeared to be more circular. However, due to the viscosity of the solution, once the rpm was increased up to 1200 rpm, the solution started gather to the edges, and created a donut shaped surface. 0.5% w/w solution was found to be more susceptible to spin coating speeds close to 1000 rpm.

3. Spin coating time

The solution is fairly sticky and viscous in nature. Once exposed to air, the film also dries quickly due to the solvent volatility and the nature of the silk. Therefore, it is important to spin coat immediately after depositing the droplet onto the spin coater. It is found that after 30 seconds of spin coating, the film surface started to dry and was no longer susceptible to spin coating. Therefore, all samples were completed with spin coating time of 30 seconds.

3.1.1.2 FTIR

FTIR review

Infrared spectroscopy can be used for almost any type of samples as long as the material is composed of, or contains compounds (rather then pure elements) [31]. It relates physical properties to chemical analysis by measuring infrared intensity versus wavenumber of light. The IR detects the vibration characteristics of chemical functional groups. When an infrared light interacts with the matter, chemical bonds will stretch, contract and bend. As a result, a chemical functional group tends to absorb infrared radiation in a specific wavenumber range regardless of the structure of the rest of the molecule. This can therefore be used to detect functional groups in material. The FTIR first collect an interferrogram which measures all the infrared frequency simultaneously. The signal is then digitized, and Fourier transform is performed on the signal. Finally, a single spectrum is outputted by the FTIR [32].

FTIR test

FTIR (Fourier Transform Infrared-Red) measurement is used to characterize the spin-on spider silk film. In this study, 40 μl of spider silk solution with 1% w/w ratio were deposited using a pipette onto a potassium bromide crystal plate. It is important to cover the exposure area completely to avoid noise. The film was allowed to dry for 24 hours, and was then inserted into the Bomen MB100 120 FTIR spectrophotometer with a 4 cm^{-1} resolution.

Before the sample is tested, a background is taken using pure Potassium Bromide crystal plate. This way, the background could be subtracted from the spider silk sample to obtain the final graph. The peaks are then chosen by using the arrows on the computer.

3.1.1.3 Nano indenter for thin film mechanical testing

Nano indenter Review

Indentation method is one of the most common methods of measuring mechanical properties of materials. Earlier indentation methods require the area of the indentation be visible for calculating the properties. However, with introduction of depth sensing indentation methods, the properties can be observed with only knowing the load and displacement of the indentation tip [33].

Instrumented indentation - the general name for depth sensing or nanoindention has become increasingly popular in providing the mechanical responses of materials from metals and ceramics to polymeric and biological materials [34]. Many systems can be generalized in terms of schematic shown in Figure 2.

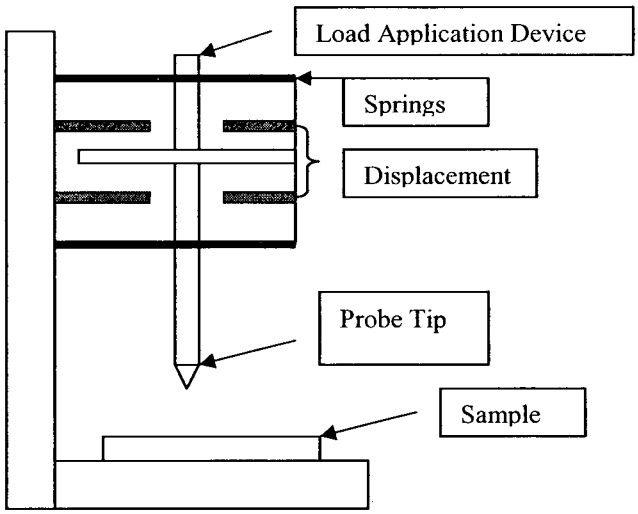

Figure 2: Schematic illustration of an instrumented indentation system

Typically, force is applied using either electromagnetic or electrostatic actuation. A capacitive sensor is used to measure displacement. In MTS nano instruments, the axis of the indentation is vertical, and in some other cases, it can be horizontal. Most indentation is force driven devices, such that the force history is most easily controlled with displacement control, achieved through signal feedback [34].

In this work, mechanical properties of the regenerated spider silk were tested using a nano indentation machine (Nano Indenter XP, MTS, USA). The indentation tip is a Berkovich diamond tip shaped as a regular tetrahedron [35]. An optical transducer and a force transducer are used to record the distance and resistance force experienced by the tip during indentation experiments. The nano indenter is programmed to measure material properties in a Continuous Stiffness Measurement (CSM) mode. The CSM is accomplished by imposing a small sinusoidal varying signal on top of a DC signal that drives the motion of the indentation tip. This allows continuous measurement data to be obtained along any point of the loading curve and not just at the point of unloading as in the conventional measurement [36].

Main mechanical properties obtained through nano indentation are hardness and modulus values. However, the TestWork software can be programmed to collect property such as viscoelasticity. The machine also has application in measuring adhesion properties through two possible methods: one is evaluating the size of a blister created by the indentation; the second is the more popular method of making a scratch while continuously increasing the load on the indenter and evaluating the force at which the film fails catastrophically. However, the second method is very qualitative and only work well for weak film-substrate interfaces [37].

Several unconventional application of the nano indentation method has also been introduced by MTS. For example, a universal testing system named NANOBionix, which has been able to characterize the spider silk fiber with great accuracy and repeatability. It is a tensile testing machine that is capable of measuring force and extension on the nano scale with high noise control [95].

A MEMS application using the nano indenter XP and the software TestWorks EXPLORER was also developed based on customer demands. A semiconductor circuit probe is tested similar to Figure 3 below, where the maximum lateral force is found in order to predict its in-service performance [38].

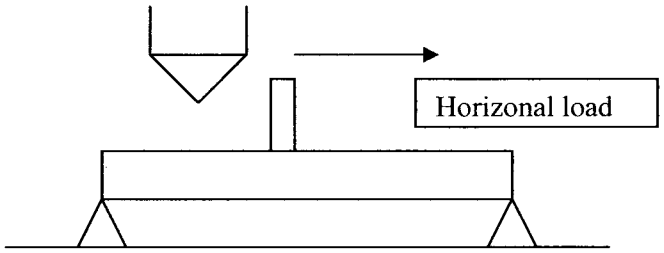

Figure 3: Schematic of test. Cube-corner face shears through probe tip.

Thin film test

Two samples of 1% and 0.5% w/w dilution thin film were used with indentation depth of 500 and 200 nm, respectively. The rest of the parameters are left in its default setting. The preset drift is often found to be difficult to obtain during day time testing. A drift value up to 0.5 nm has been used and showed not significance in final test data. Two sets of sample data (horizontal and vertical from edge to edge) were collected for each film. Each has 8-10 indentation points. Hardness, elastic modulus and viscoelasticity of the film were obtained.

3.1.2 Results and Discussion

3.1.2.1 FTIR

Previously, FTIR measurements of native spider silk fibers have shown peaks corresponding to Amide I, II and III vibration modes. These peaks correspond to the strength and arrangement of polypeptide that are present in its secondary structure. The material properties of spider silk have been shown to be strongly linked to its secondary structures [9, 30]. FTIR peaks at 1652 and 1669 cm^{-1} in the Amide I region have been assigned to α-helical and β-sheet backbone conformations respectively [9, 39]. A peak at 1540 cm^{-1} in the Amide II band corresponds to disordered conformations,[40] while peaks at 1230 and 1240 cm^{-1} in Amide III are associated with β-sheets and disordered conformations [9].

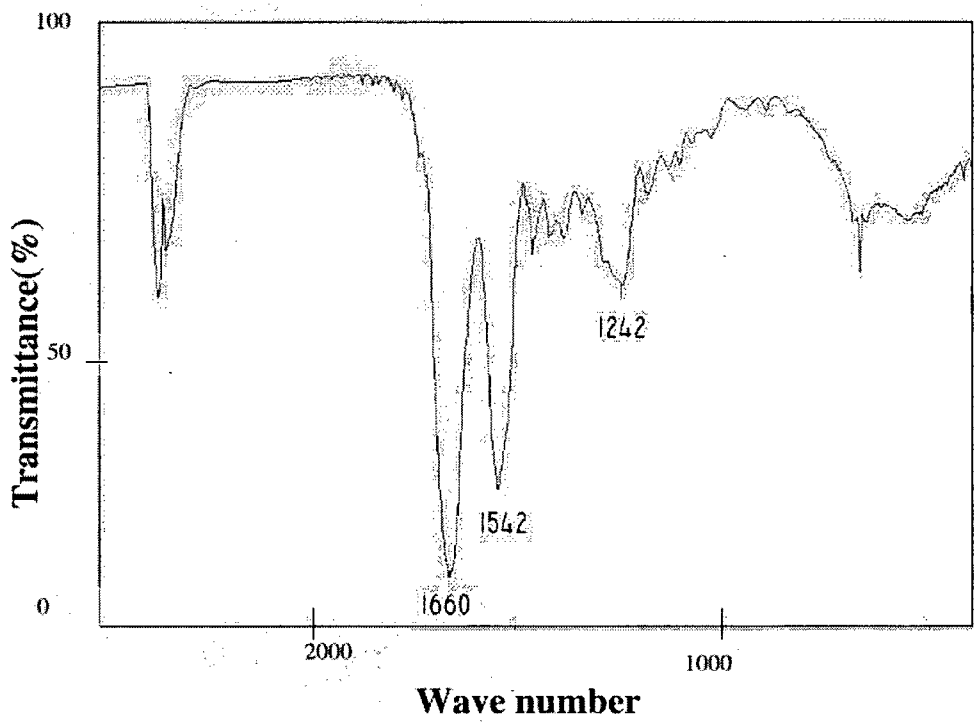

Figure 4: FTIR spectra of spider silk thin film

As shown in Figure 4, the FTIR spectrum of the regenerated spider silk thin film obtained from a spin-on process shows peaks at 1660, 1542 and 1242 cm^{-1}. The three peaks ranging in intensity from moderate to strong, indicate the presence of α -helical and random conformation components. The β -Sheet conformation, which is suggested to be responsible for the high stiffness and strength of the material [6], is not strongly present in this work. This indicates a change in the material's secondary structure in comparison to the native fiber state.

3.1.2.2 Thin film surface and cross sectional view

Figure 5 illustrate the visual differences between the two diluted samples. Figure 5(b) shows the much smoother edge obtained from 0.5% w/w sample in comparison to Figure 5(a), the 1% w/w sample. Figure 5(c) show one of few voids appeared in the 1% w/w solution. This is suspected to be a result of viscous solution spun at high rotational speeds. Figure 5(d) shows a small visible piece of fiber that was not dissolved into the solvent. Previous study has reported similar findings [6].

Treatments mentioned Seidel. A (1998) suggested filtering of the solution with filter pore size of 1 μ m. Subsequent evaporation of the solution was suggested at ambient temperature over a 24 hour time period and further annealed in a vacuum for 60 $°C$ for 16 hours to obtain a fiber. However, overall, the number of fiber pieces within the film was small, thus it is not a significant indication of low solubility, or will not have any major effect on the overall film properties.

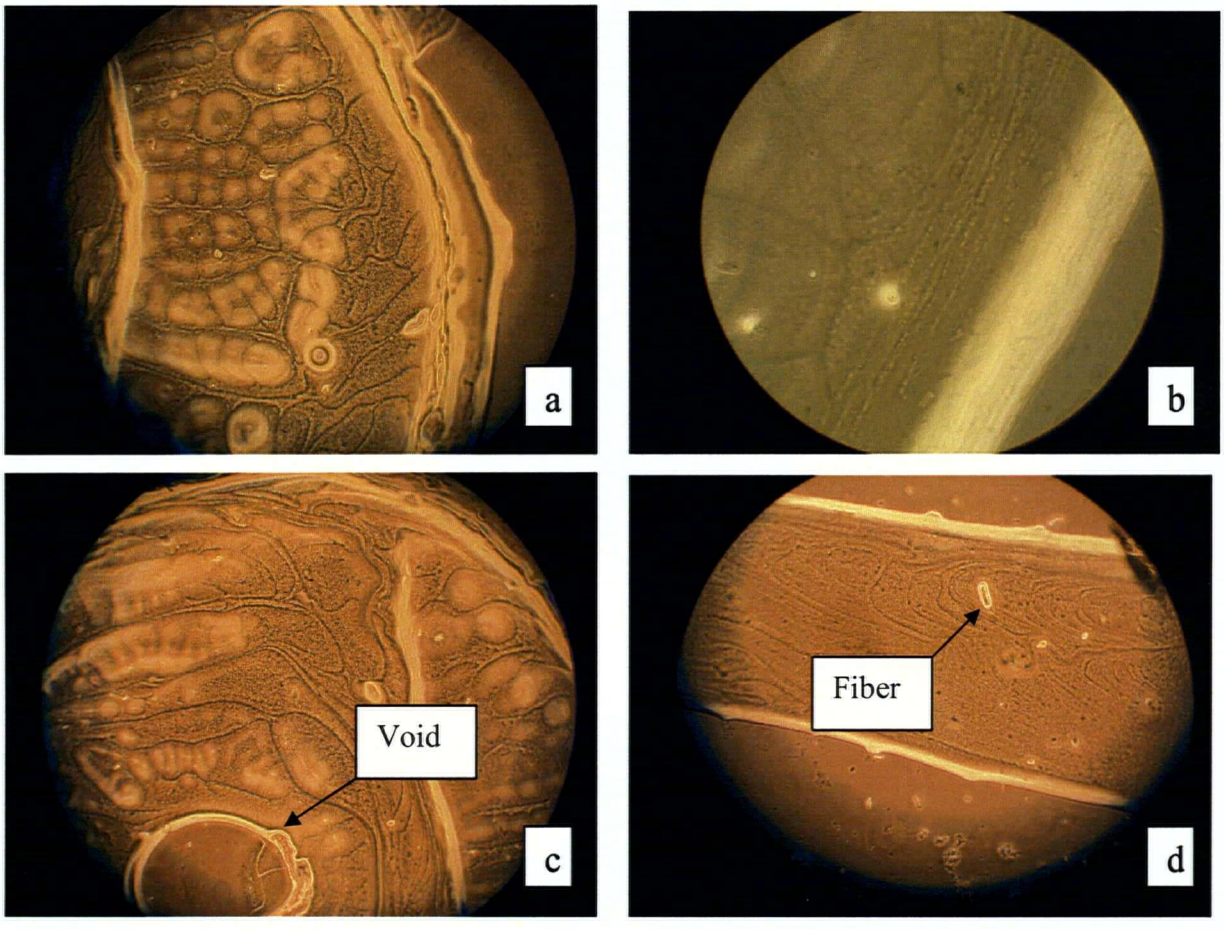

Figure 5: Microscopic picture (magnification x100) of spider silk thin film edges
a) sample 1%w/w; b) sample 0.5% w/w; c) 1% w/w with large void; d) 1% w/w with short undissovled fibers

Figure 6 are SEM images of the thin films which shows cracking and surface roughness that is much more prominent within the 1%w/w sample.

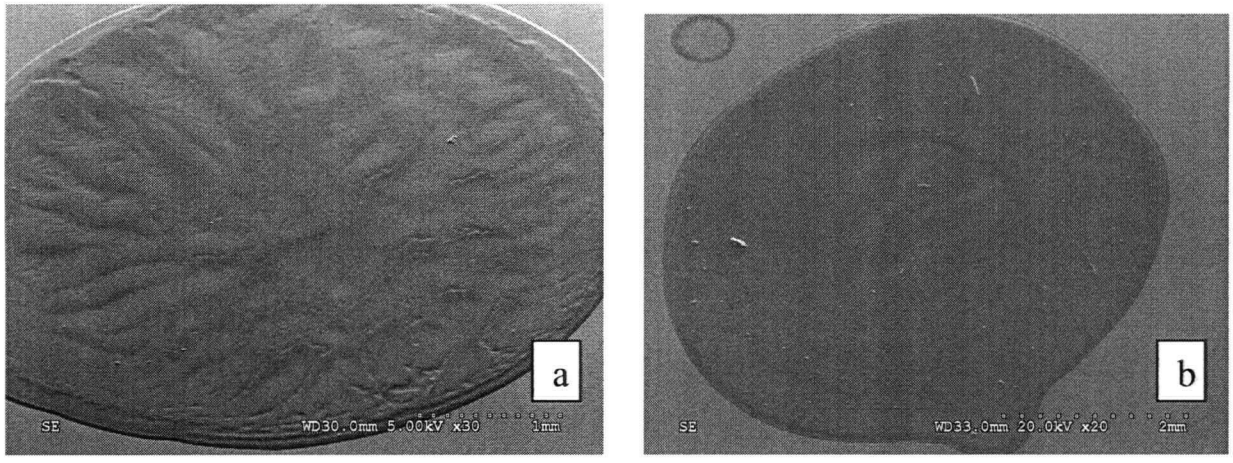

Figure 6: SEM picture of thin film spider silk a) sample 1% w/w b) sample 0.5% w/w

Figure 7 shows a cross-sectional view of the thin-film spider silk. Porosity is consistent throughout the film, and there is no significant porosity difference between the two diluted solutions (1% and 0.5% w/w). These voids can be explained by the evaporation of the HFIP solvent, which is present in both films. It is also evident that the film surface is not completely smooth. Grey pore like features or asperities are scattered throughout the surface.

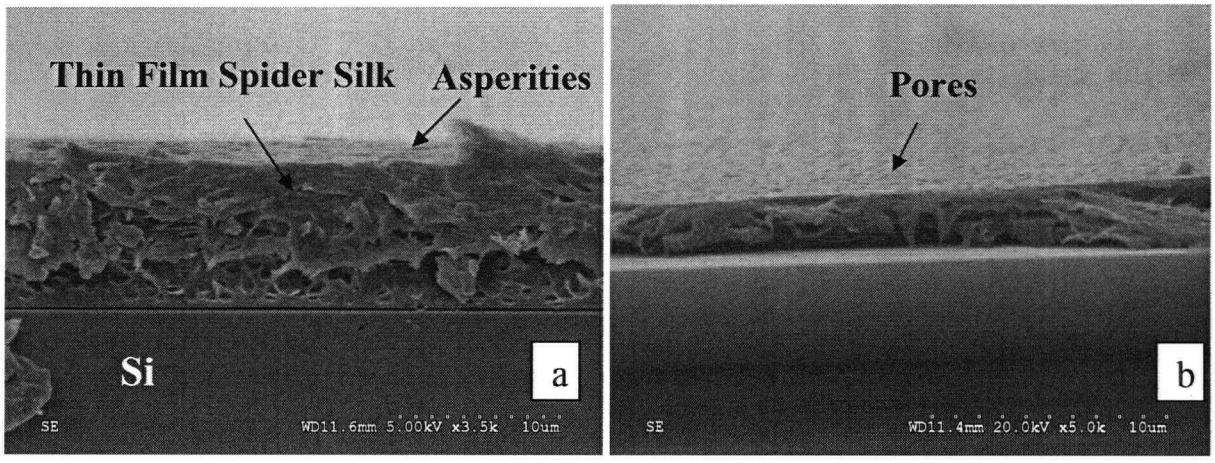

Figure 7: Thin film cross section of (a) 1% w/w (b) 0.5% w/w spider silk

Smooth thin film was also obtained through 0.25% dilution. Figure 8 shows the cross section of the thin film. The thin film thickness range from 3 μm around the edges to 500 nm near the center of the film. This shows that with a reduction in dilution, smoother and thinner film can be made using spin coating techniques.

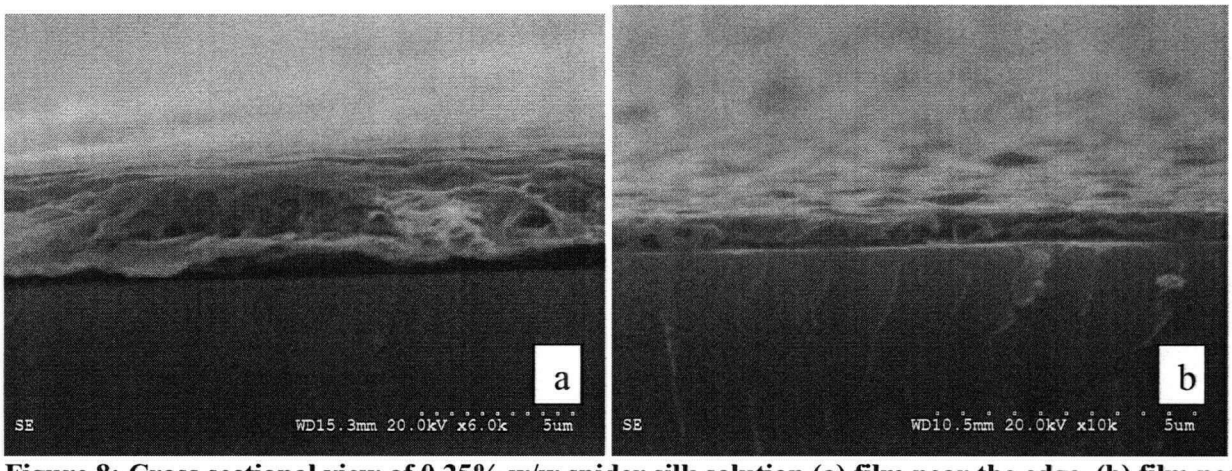

Figure 8: Cross sectional view of 0.25% w/w spider silk solution (a) film near the edge, (b) film near center

3.1.2.3 Mechanical Testing

Results from mechanical testing of the film are obtained by nano indentation method. Please note that elastic modulus is obtained using this method, rather than using properties observed from a stress and strain curve. This is based on the fact that spider silk material property is similar to rubber [13], which exhibits nonlinear elastic behavior [41]. Therefore, when determining the elastic properties, linear assumption used for material such as steel or aluminum can not be applied here.

The data collected using nano indentation has taken into consideration of the substrate effect on thin film tests. This has been previously documented in many studies [42, 43]. Using a widely accepted rule of thumb, the intrinsic property of the film can be reasonably detected with minimal effect from the substrate when the indentation depth is kept to 10% of the film thickness [44]. In addition to this rule of thumb, the relative properties between the film and the substrate are also very important. The more disparate these properties are, the shallower the data needs to be taken. For thin films less than 1 um, there is truly no measurement of the film that is 100% substrate independent. However, the best measurements taken are within the first 10% of the film thickness. For a 5 um film, the film begins to behave much more like a bulk material, maintaining the displacements from indentation experiment within the film [45]. Since the thickness of our sample is between 5 and 10 μm, the material should act more similar to a bulk material. In addition, only consistent mechanical property data within this region is used in this work, which should improve the accuracy of the nano indentation data.

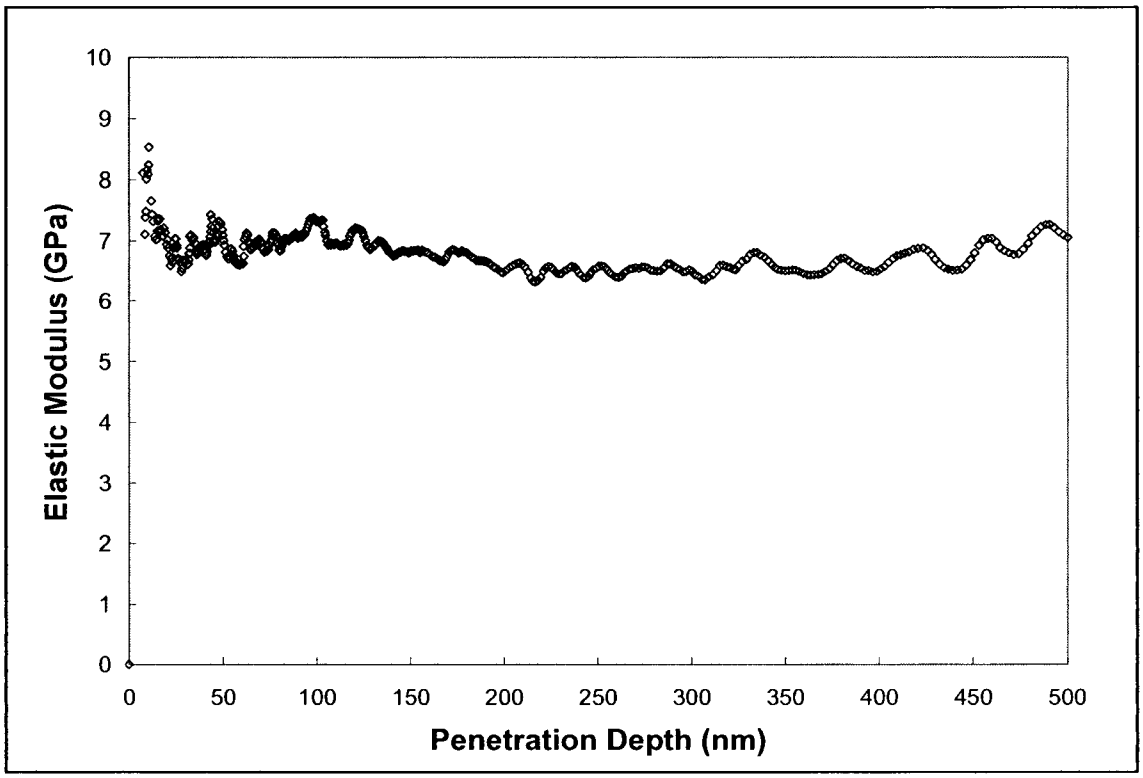

Figure 9: Elastic modulus value vs. penetration depth for central point

Elastic modulus data for a center point is shown in Figure 9. The data is found to be fairly consistent during the first 500nm. Noise in the initial 50nm is often present, therefore, value collected within this region was not considered.

Since our sample is consist of soft material on hard substrate, as the penetration depth increases, the substrate effect will become more prominent. We expect to see an increase in the modulus value until we reach data point that represents modulus value of the pure substrate. This effect was found and shown in Figure 10.

Because the sample was circular, two sets of sample data (horizontal and vertical edge to edge) were collected. The two data sets are perpendicular to each, with 7-8 points each evenly spaced. This set up will check to see whether a change of properties can be detected across the diameter of the film.

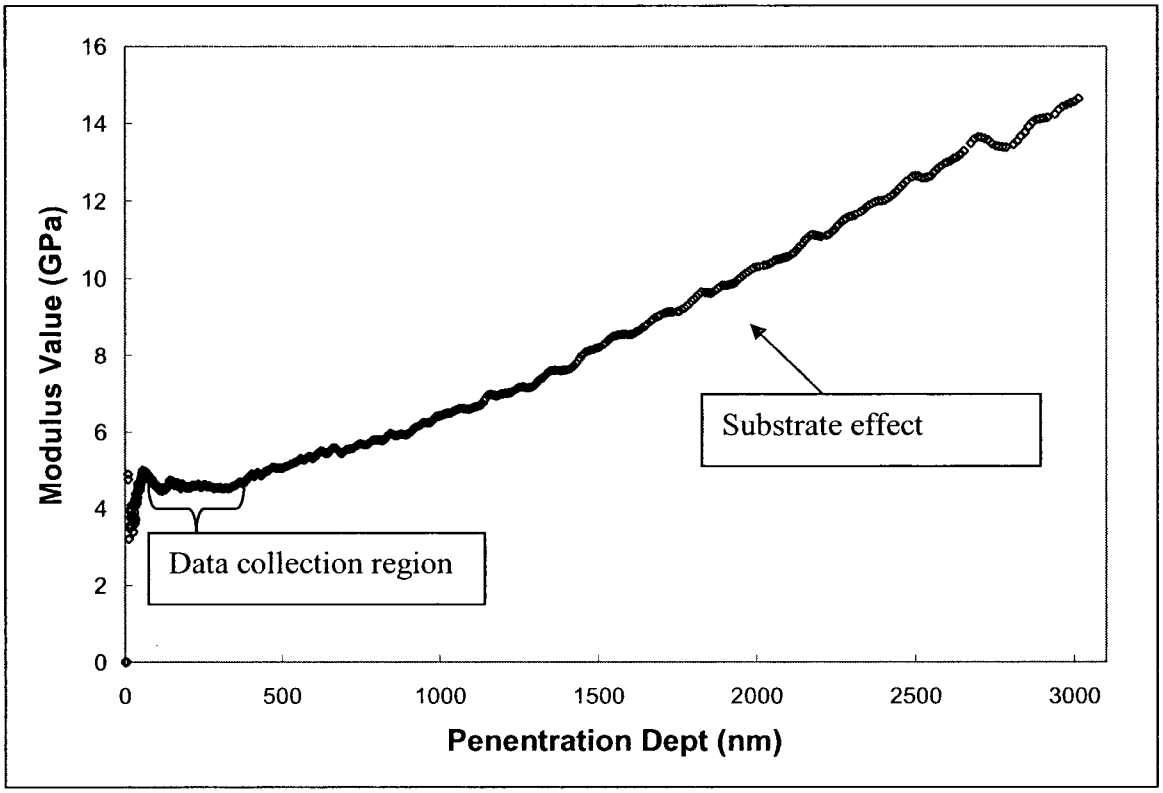

Figure 10: Substrate effect for 0.5% w/w spider silk film sample with 3000 nm penetration dept

Figure 11 shows the averaged modulus value for each penetration point on the vertical and on the horizontal line. These 2 values were comparably close, especially for the more central points. This is expected, since, from the microscopic pictures, it can be seen that the surface consistency of the material around the edge of the sample is not as homogeneous as the central areas. Overall, the elastic modulus was found to have a mean value of 6.266 GPa with a standard deviation of 0.674 for the horizontal data set, and 6.032 GPa with a standard deviation of 0.773 for the vertical data set.

Hardness of the material was also tested. Similar to Figure 11, Figure 12 is constructed based on hardness values. The horizontal data appeared to be more consistent than the vertical dataset. This is slightly unexpected; however, this follows the trend of the modulus data, since its vertical dataset also had a larger standard deviation. Perhaps, the vertical data points are slightly less smooth then horizontal points, which can affect the final values. Overall, the hardness test data for the horizontal data set was found to have a mean value of 0.293 GPa with a standard

deviation of 0.023. The vertical dataset was found to have a mean of 0.31 GPa with a standard deviation of 0.065.

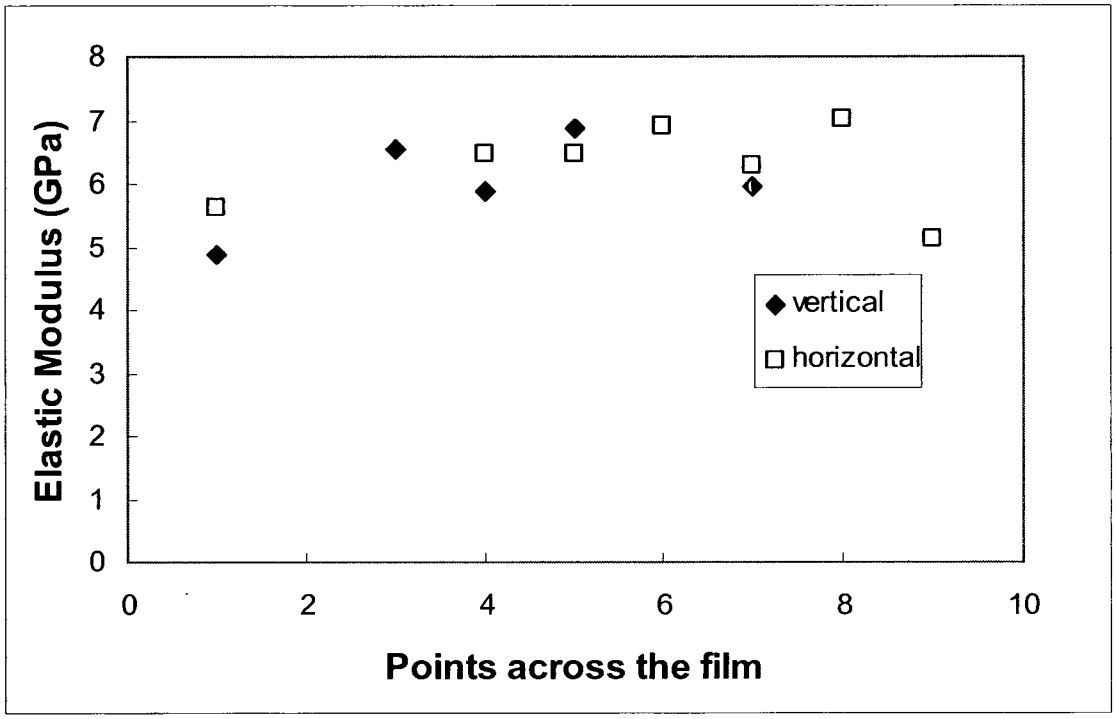

Figure 11 : Elastic modulus value collected across the film in vertical and horizontal directions

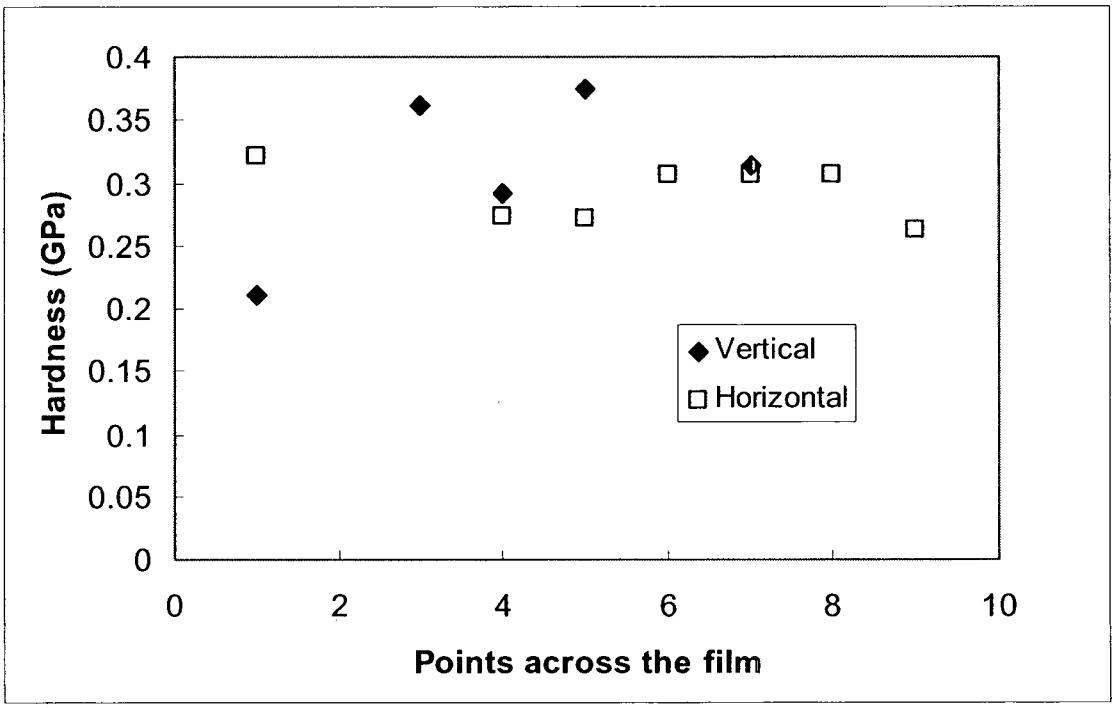

Figure 12: Hardness value collected across the film in the vertical and horizontal directions

Further testing was completed using nano indenter where the viscoelastic data was also collected. This is presented in table 4.

Table 4: Mechanical testing of thin film spider silk

SAMPLE	ELASTIC MODULUS (GPA) [STD]	HARDNESS (GPA) [STD]	VISCOELASTICITY (LOSS TANGENT) [STD]
1% w/w	7.251 [0.494]	0.276 [0.005]	0.0436 [0.0065]
0.5% w/w	4.41 [0.342]	0.182 [0.012]	0.0442 [0.0012]

The elastic modulus and hardness decrease as the %w/w ratio of silk to solvent decreases. This is likely due to the difference in fibroin concentration. However, an advantage of the 0.5% w/w solution is its film consistency, reduction in surface roughness, and its increased sensitivity to the effect of spin-coating speed.

As shown in Figure 7, the film porosity appears to be less prominent on the upper region than the lower region of the cross section. The mechanical testing data are mostly collected on the upper region of the film thickness (the first 500nm), and this could be a contributing factor in the high Young's modulus value that is not common in porous materials.

Data on the viscoelastic properties (loss tangent) of the film are obtained for the first time in this experiment. The loss tangent showed no dependency on %w/w dilution in the range used and was found to be similar to the loss tangent of human bone specimens (0.05) [46].

3.2 Spider Silk Microbridge

A surface micromachining technique was developed to fabricate a spider silk microbridge and fracture testing was performed. Stress and strain plots were obtained.

3.2.1 Experimental Methods

Microfabrication

Spider drag-line silk is dissolved in 1,1,1,3,3,3 hexafluoro-2-propanol (HFIP) solution with a ratio of 1% w/w. In order to demonstrate a first micromachined spider silk microstructure, a

modified surface micromachining process with a sacrificial etching technique [47] was carried out to fabricate a free-standing spider silk microbridge.

Figure 13(a), shows a silicon substrate that is anisotropically etched to form a cavity. Sugar solution (50% wt) was poured into the cavity and air dried to form a sacrificial layer (Figure 13(b)). The spider silk solution was then deposited using a 2 μl needle syringe and air dried (Figure13(c)). Finally, the silicon substrate was immersed in water to "etch" away the sugar (Figure 13(d)), leaving the free-standing spider silk microbridge shown in Figure 13(d).

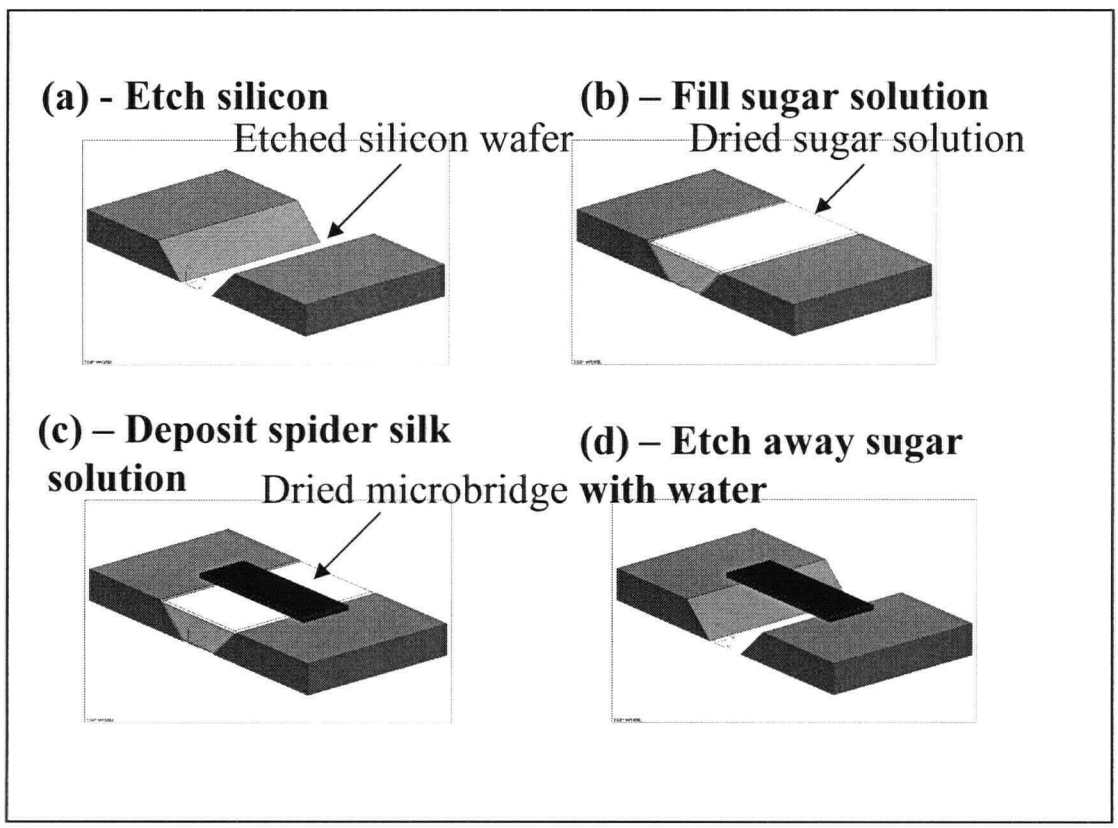

Figure 13: Sacrificial etching process steps to fabricate spider silk microbridge

The use of sugar is spun from the idea that spider silk does not dissolve in several polar solvents, including ethanol, methanol and water (in the order of increasing polarity). However, the solvents affect the material properties of the silk. Research has demonstrated that with increase in polarity, a decrease in modulus and breaking strength can be found [20]. Originally, methanol and ethanol were more desirable choices because they have lesser effect on spider silk. However,

these alcohols are best known for dissolving organic materials such as natural of synthetic resins or oils. Therefore, it was difficult to find a suitable material that will dissolve in these two alcohols, and still be able to crystallize to form a sacrificial layer. Water was then chosen because it dissolves a variety of different crystals. In order to find the best lifting solution, the following materials were tested. Sugar was chosen for its fast crystallization and low cost.

Table 5: Material tested for lifting solution

MATERIAL	OVERNIGHT RESULTS
Sodium Carbonate	Small island of crystals, donut shape
Sodium bi-carbonate	Liquid
Ammonium sulphate	Crystallized fast
Calcium chloride	Liquid
Potassium chloride	Partly crystallized
Sugar (glucose)	Crystallized fast
Salt (sodium chloride)	Solid salt need to be grown from a seed, or else its solution dries to become particles

A 50/50 sugar to water solution was mixed until all the sugar crystals were completely dissolved. Initially, the sugar drops were deposited into the etched slot on the substrate through one of its openings. The sugar was evaporated, crystallized and solidified. This left a convex shape to the sugar surface (Figure 14). More sugar solution was added, and the step was repeated until the dried sugar filled the opening. Due to water tension, the final sugar layer has a concave surface (Figure 14). The protruding sugar crystal is then sanded away or carefully removed by a knife.

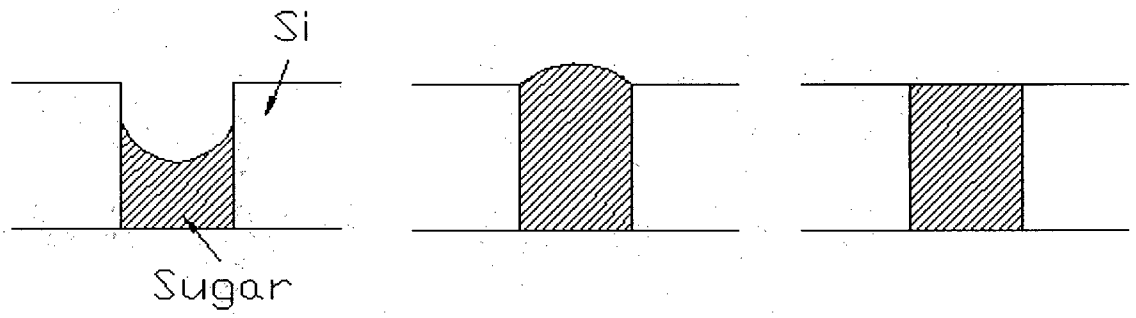

Figure 14: Initial sugar hardening process

These steps were long and tedious; it took up to several days at a time. An improved method was developed by using the hotplate to speed up the drying process. A piece of Teflon tape act as a bottom seal which keeps the sugar solution within the slot. The hotplate is kept at minimum temperature, and the sugar is essentially baked and hardened. This process takes approximately 3-4 hours. Once finished, Teflon tape is removed, revealing a flat sugar surface ready for deposition of the spider silk beam.

Fracture Testing

The nano indentation machine was used to perform fracture testing on the microbridge sample. The high load method was used to apply a concentrated load in the center of the microbridge by the indenter tip. In order to prevent indentation occurring in the spider silk layer, a large silicon chip (approx. 500 x 800 x 1000 μm^3) was inserted between the nano indentation tip and the microbridge during the nano indentation process. The load was gradually increased until the microbridge had fractured. The results of load versus displacement curve were converted into stress-strain curves.

A nano indentation machine was used for a loading-unloading test on the spider silk microbridge and the results are shown in Figure 15. The microbridge was first loaded up to 5 mN and unloaded. A second loading-unloading cycle with a larger maximum force of 100 mN was then applied and released. The unloading did not follow the path of the loading curve. It can be concluded that plastic deformation appear to have occurred with the loading of 5 mN. To examine more closely, the 100 mN loading-unloading cycle overlaps with the 5 mN load when the initial displacement is small. This contradicts the previous statement that plastic deformation has occurred. From this overlap, it seems that the film was able to eventually recover the deformation caused by the 5 mN loading cycle. This is an evidence of load hysteresis. In this study, a minimum of 15 minutes was allowed between each cycle. To examine whether time between loads was part of the equation for spider silk recovery process, an additional sample was tested where no time was allowed between the loading cycles.

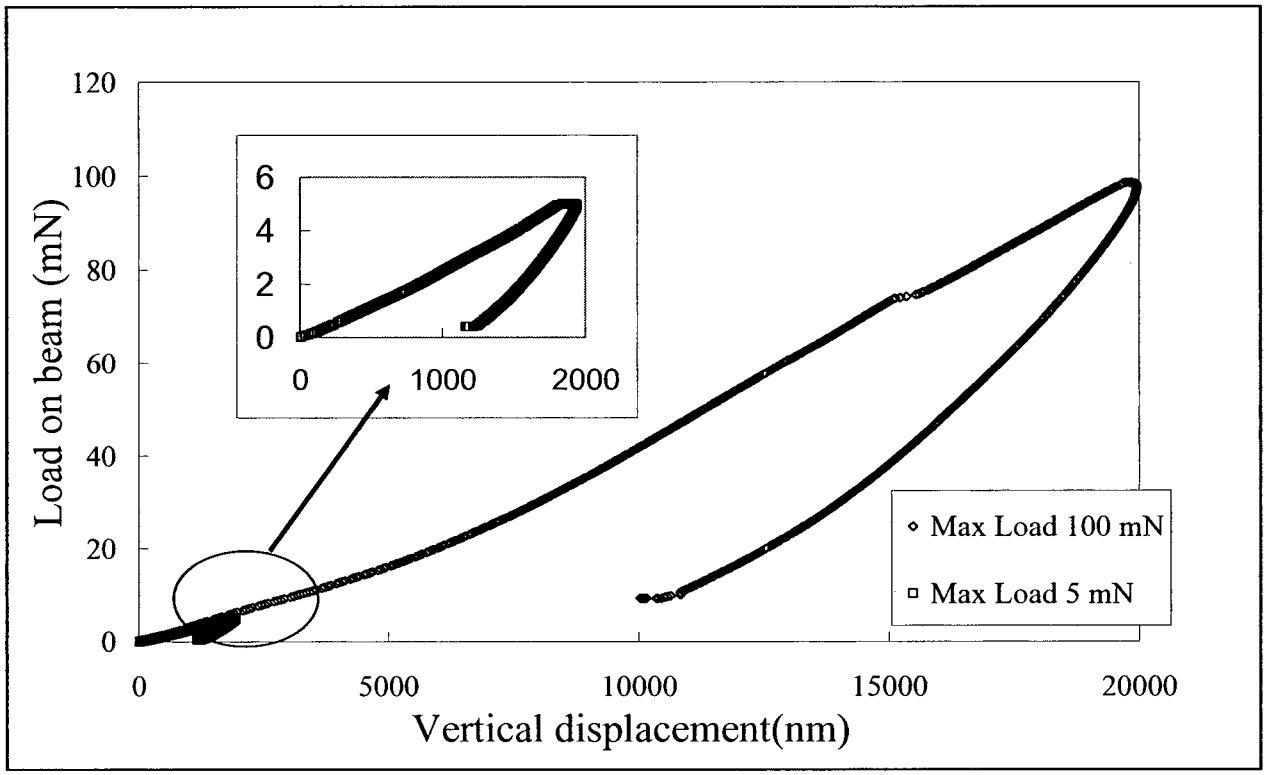

Figure 15: Loading and unloading tests. Two maximum loads were reached and released.

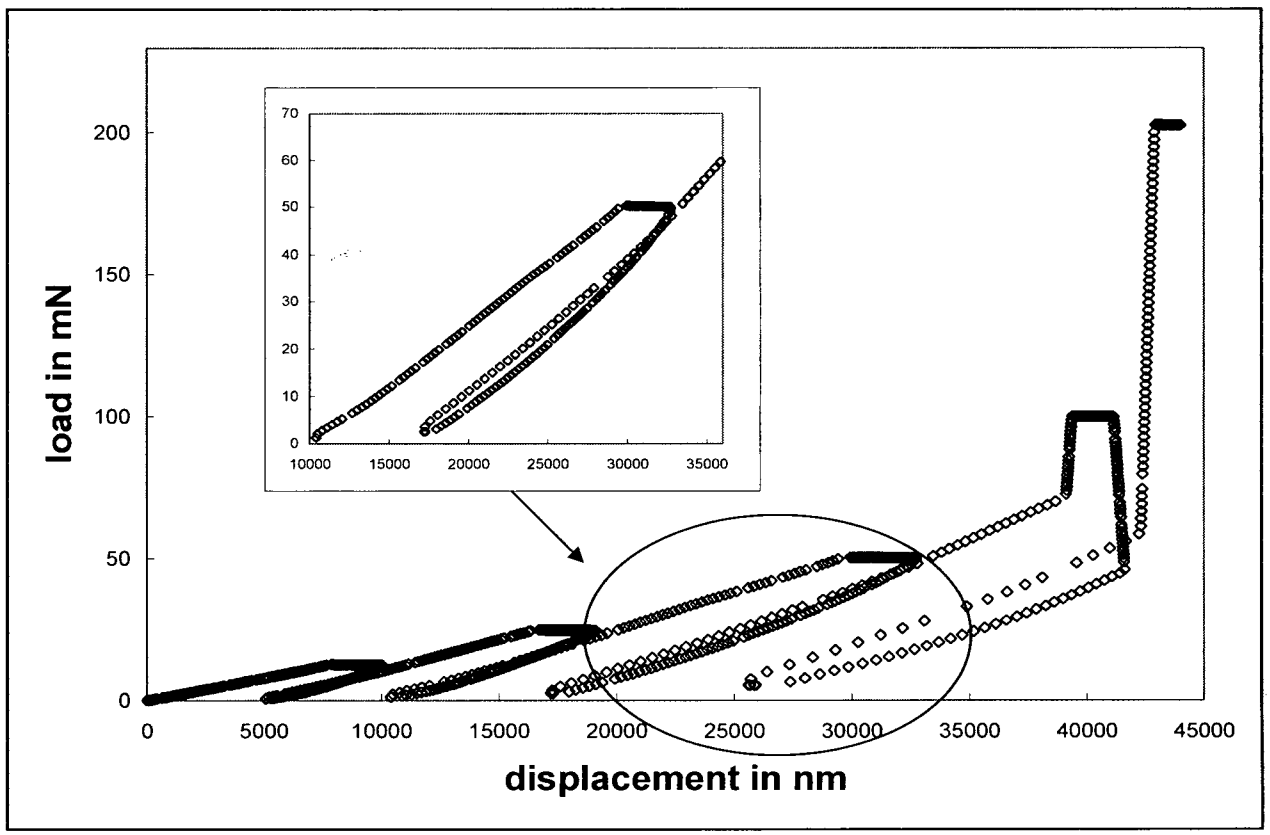

Figure 16: Loading and unloading with hold time of 30 seconds

Shown in Figure 16, the sample is allowed to stay at maximum applied load for 30 seconds before unloading is performed. A higher stress was reached with every subsequent loading. The unloading stops at 90% of the total maximum load and reload with the next cycle. Taking a closer look at the unloading of cycle 3 and loading of cycle 4, we can see that the slope of cycle 3 unloading is slightly different than the loading, however, the spider silk was able to recover, and the loading of cycle 4 appear to be very similar to loading of cycle 3. This also is evident between cycle 4 and cycle 5. In this case, the time between the loading and unloading did not play any significant role in the hysteresis curve. Additional test should be completed to better map the hysteresis by loading the sample to near maximum load and unloading to 0 with several repeated loadings.

A fracture test was carried out on the spider silk microbridge using a nano indentation machine. The loading force was increased gradually and the displacement was recorded until the beam fractured. It is assumed that the spider silk microbridge is a beam like structural member, with fixed-fixed ends. Since the load is applied on to the beam through a large silicon chip, the beam experiences a distributed load instead of a point load.

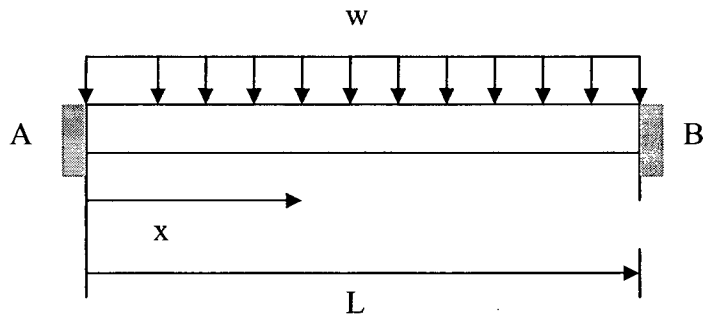

The maximum moment will be experienced by the two fixed ends. Using method of integration for statically indeterminate beams, the maximum moment is calculated below [41]:

$$EI\frac{d^2v}{dx} = \frac{wL}{2}x - \frac{w}{2}x^2 - M$$

$$EI\frac{dv}{dx} = \frac{wL}{4}x^2 - \frac{w}{6}x^3 - Mx + C_1$$

$$EIv = \frac{wL}{12}x^3 - \frac{w}{24}x^4 - \frac{M}{2}x^2 + C_1x + C_2$$

With three unknown, and three boundary conditions:

1) $v = 0$ at x = 0 2) $\frac{dv}{dx}$=0 at x = 0 3) $v = 0$ at x = L

M can be solved as,

$$M = \frac{F \cdot L}{12}$$

where M is the maximum moment at the fixed-ends, F is the loading force applied by the indentation tip and L is the length of the original beam. The normal stress can then be calculated using [41]

$$\sigma = \frac{M \cdot c}{I}$$

where σ is the maximum stress, c is half of the thickness of the beam, and I is the moment of inertia of the cross section area (which in this case assumed to be rectangular) of the beam. The strain is calculated following the Pythagorean theorem.

$$l^2 + B^2 = C^2$$

where, B is the vertical distance traveled by the nano indentation tip, and C is the new length of the beam. Therefore, the change in beam length, Δ is equal to C-l. The strain is then calculated by $\frac{\Delta}{L}$. The first fracture test results are shown in Figure 17. The SEM of the actual microbridge is shown in Figure 18. The release of the beam was difficult to control as the beam deposited on the sacrificial layer vary in size. Some of the failed attempts were also imaged using SEM, and this can be reviewed in Appendix A. This appendix also includes side view of a microbridge, where the thickness can be estimated.

3.2.2 Results

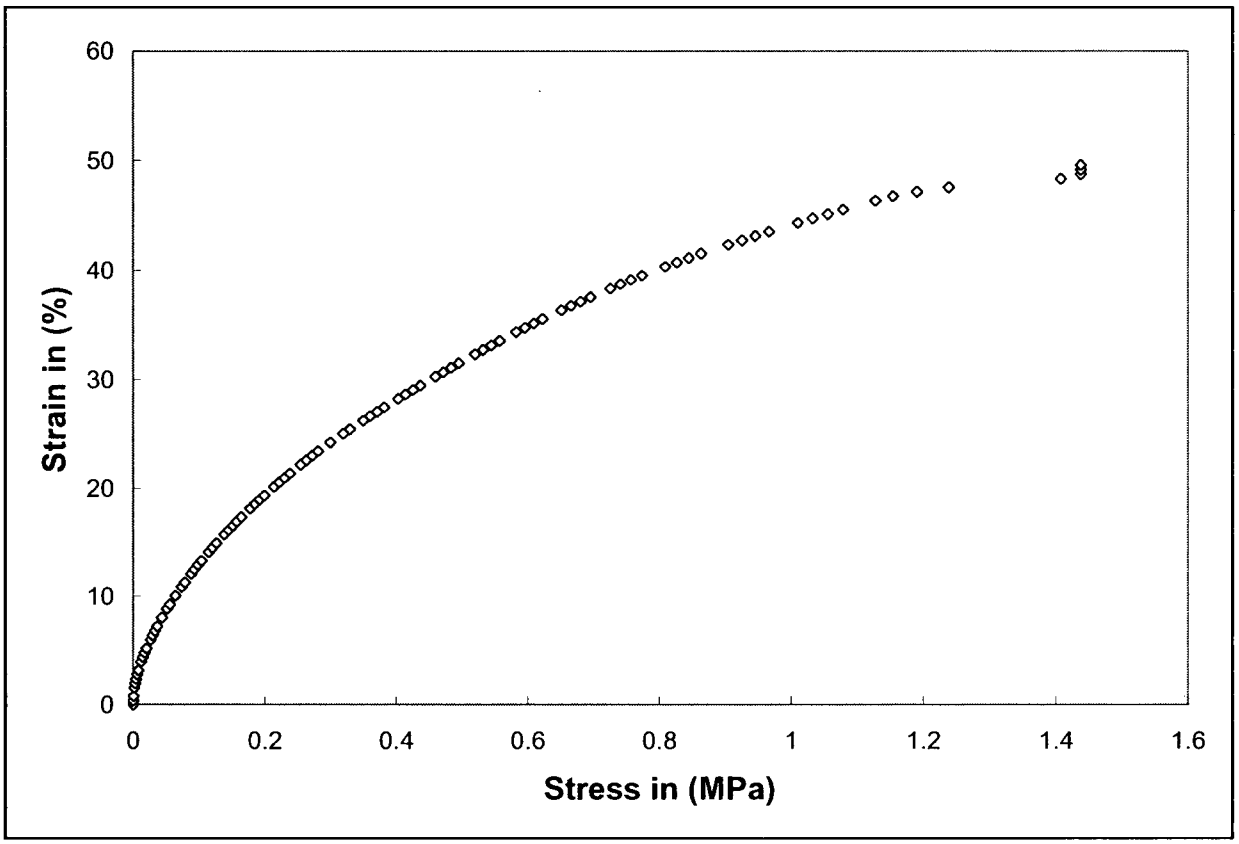

Figure 17: Initial Fracture testing result

The fractures occurred at the fixed-ends where maximum moment and maximum normal stress occurred. This is clearly shown in Figure 18(b). The initial fracture test showed a maximum stress of 50.8 MPa and a strain of 1.44%. Additional tests were performed following the same methods to verify the data, as well as to verify the repeatability of the test method. Figure 19 shows a stress-strain curve obtained from the fracture testing. Three microbridges were tested. The fractured strength was found to be in the range of 65.6-85.1 MPa with a strain range of 1.84-2.4%. One main contributing factor in the differences observed between the three sets of fracture data is due to the variations in the dimensions of the microbridges. These microstructures are immersed in water in order to be released from the sugar sacrificial layer. The volumetric change of the microbridge depends on the time in which it is in contact with water, therefore it is difficult to control.

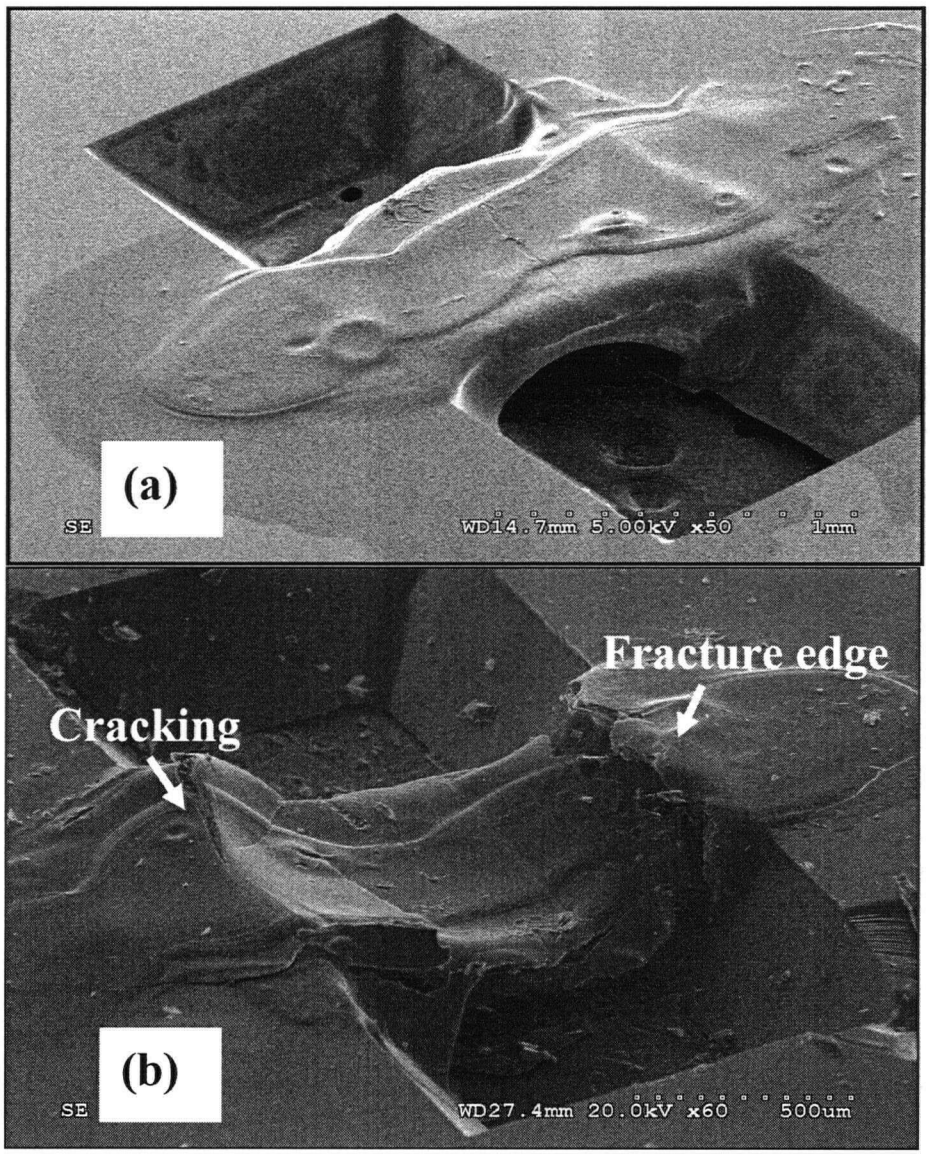

Figure 18: SEM photo of the spider silk microbridge (800 x 800 x 40) before (a) and after (b) a fracture test

The reported regenerated spider silk in a fiber form had UTS of 320 MPa and breaking strain of approximately 10-14% [48]. The material properties (UTS and breaking strain) obtained in this work is significantly lower. This difference could be explained by the lack of post-drawing process involved in the spider silk thin film spin-on formation, as compared to fiber formation with repeated post drawing steps [29, 48].

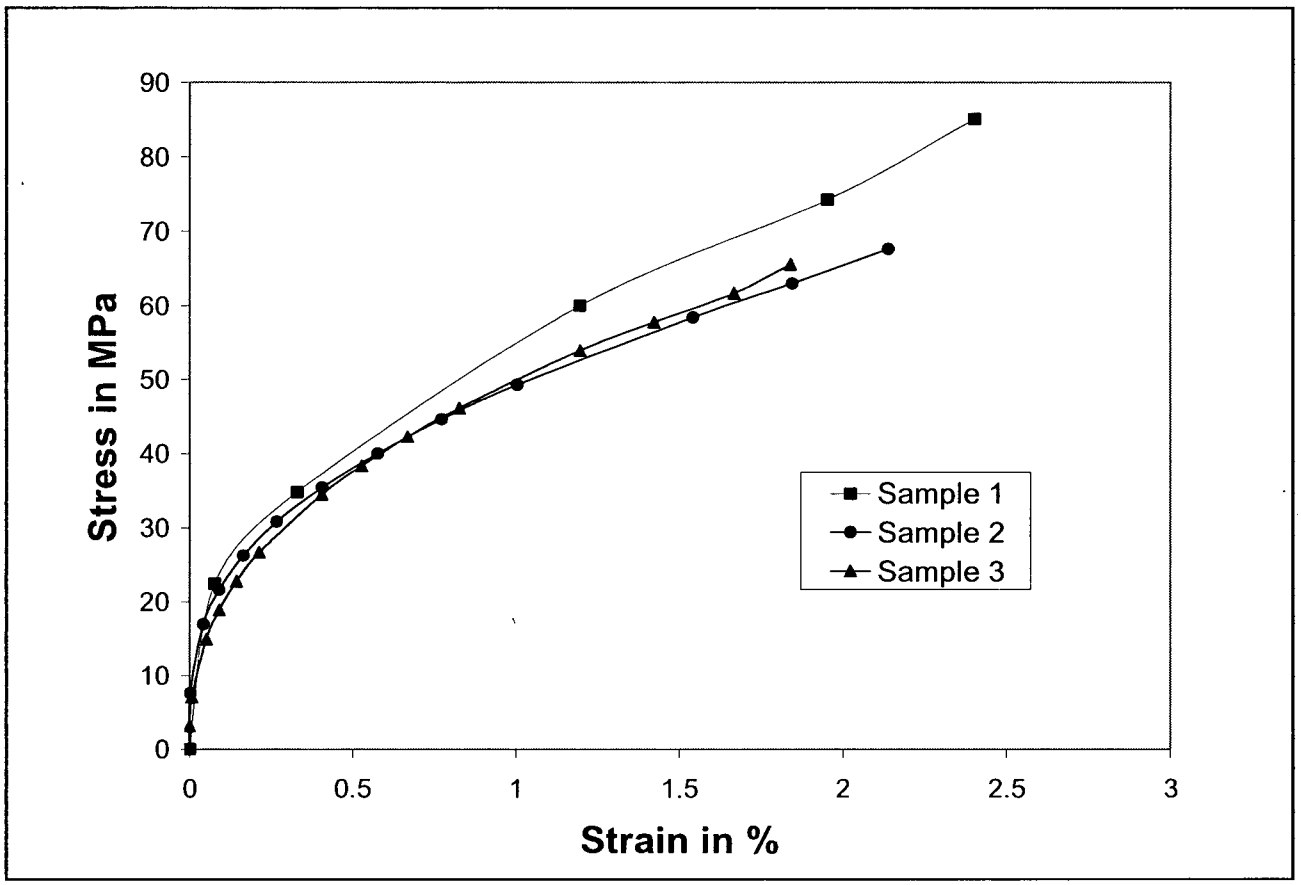

Figure 19: Stress and strain curve of a spider silk microbridge. The UTS' were measured as 65.6, 67.6, and 85.1 MPa, for the three samples with microbridge widths of 0.9, 0.8 and 0.4 mm respectively. The other dimensions are identical between the three samples

An additional factor to consider is the effect of water on the spider silk film. In this experiment, the microbridge must be immersed in water in order for it to be released. Previous studies have shown that water causes changes in the arrangement of the silk fibroins and causes super contraction of the silk fibers that can decrease the ultimate tensile stress and increase the brittleness of the material [29, 39, 49]. When regenerated fibers were stretched in water, their ultimate tensile stress was reduced to 25 MPa [29]. It is unlikely that our silk structures would super contract in the same fashion that native fibers do, however the immersion in water likely does allow some rearrangement of the protein polymer backbone. With evidence showing the importance of post drawing and the effect of water on the spider silk, it can be concluded that the reduction in elasticity as well as UTS are a product of these two effects. However, the regenerated spider silk thin-film studied in this work has a much higher ultimate tensile stress

compare to hydrogel (with UTS in the range of 10 MPa [50]) and PDMS (with UTS in the range of 2.4-7 MPa [51]).

In order to avoid the usage of water (due to its effect on the material properties) and to obtain better control over the size of the microbridge, new micromachining process should be implemented in the future. Inkjet printing has been widely used to produce many polymeric microstructures for MEMS. This technique avoids the difficulty in controlling the etching surface of polymers. This inkjet technique was also implemented in this study. However, due to the lack of spider silk supply, this set of experiments could not be completed. The preliminary work including experimental design, setup, and results are shown in Appendix B.

3.3. Summary

This chapter presented regenerated spider silk as a biomaterial for MEMS. Thin-film formation using a spin-on process and a surface micromachined spider silk microbridge were demonstrated. Mechanical testing on both the thin-film and spider silk microbridge were performed using a nano indentation machine. The elastic modulus of the thin-film spider silk was found to be 7.251 GPa. A viscoelastic property, loss tangent, was found to be 0.044 and is close to the value of human bone. The ultimate tensile strength was found as 85.1 MPa by fracturing a spider silk microbridge and is 2 to 10 times higher than conventional biopolymers such as hydrogel that have been used in MEMS fabrication.

The method for fracture testing should be improved for future work. A setup resembles an Instrum machine should be fabricated. In this case, the two ends of the free standing microbridge will be attached to two separate pieces. As the pieces are being pulled apart, strain and stress measurement can be made.

The currently sacrificial layer consists of sugar where the silk is exposed to water. In order to reduce or eliminate the effect of supercontraction, it is desirable to find a new sacrificial material which can be a solution that will crystallize and eventually dissolve into a solvent that is less polar than water, for example ethanol.

CHAPTER 4

Spider Silk Beam Using Ni for Magnetic Actuation

A magnetic beam is formed by creating a new composite material consists of spider silk as the matrix with Ni particles embedded within. The beam is designed and fabrication steps were developed. Its magnetic properties were measured along with its material properties. Its mechanical properties were tested using a static bending test. The fabrication requires small number of steps and no expensive processes or equipment. This demonstrated a proof-of-concept design for potential MEMS applications such as sensors or drug delivery devices.

4.1 Magnetic theory

Integration of magnetic components into MEMS as a way of acquiring additional functionality has long been studied and reviewed [52]. Devices using magnetically actuated optical fibers and sensors have been found to be feasible due to advantages of low power consumption, long-distance movement and large actuation force [53-56]. Magnetic particles used for ferromagnetic composites have also been used in MEMS application [57, 58]. Incorporating these existing technologies, we present here a spider silk magnetic beam for potential biomedical applications.

Magnetic behaviour of a material is governed by the interaction between the dipole moment of its atoms and the external magnetic field. Based on this behaviour, materials can be categorized into diamagnetic, paramagnetic or ferromagnetic. Diamagnetic material has no permanent magnetic moments, where as the other two maintain permanent magnetic moments [59]. Paramagnetic material exhibit a magnetization that is in the direction of the applied field, and is

proportional to this applied field. Ferromagnetic materials possess large permanent magnetizations even in the absence of an applied magnetic field. When under an external magnetic field, it tends to stay magnetized even if the external field is removed, and this tendency is called hysteresis. The percentage of the saturation magnetization that is retained after the removal of external field is called the remanence [60].

Engineering materials are typically classified as either soft or hard magnetic materials. Soft magnetic materials such as Iron and Nickel require relatively low magnetic field intensities to magnetize and demagnetize. These materials are often suitable for applications where the magnetic field varies cyclically, such as electric motors [59, 61]. Hard magnetic materials such as rare earth cobalt, Strontium ferrite have a wider hysteresis loop than soft magnetic materials, thus, requires high magnetic field intensities to magnetize and demagnetize. It tends to have very large coercivity and remanent magnetic field. They are often used as permanent magnets for motors and generators. [59, 61]

In order to characterize its properties, an M (magnetization) versus H (magnetizing field) hysteresis loop is plotted for each material. Using the definition of the M-H curve, a good soft magnetic material would have low coercivity (H_c) and high permeability(μ) [57]. Low coercivity means the magnetization field required to totally demagnetize the sample is small, and thus requires low power consumption. High permeability means it is easy for the magnetic field to penetrate a medium, thus creating a higher magnetic force [61]. Typical ferromagnetic materials such as Ni or Fe are chosen here for these desirable properties. Without going into details of magnetic theory, a typical conversion table for magnetic properties can be found in Appendix C.

Recent work by *Hans et.al*, has shown fabrication and characterization of a magnetically actuated fiber scanner. Such optical scanner can be used in vitro for imaging of surface tissues. By mechanically steering the fiber using external magnetic field, it consumes low power, and reduces the size by eliminating conventional electric wirings. They achieve this by coating the optical fiber with a ferromagnetic gel consist of Ni powder and epoxy. They were successful in actuating the fiber optic under an applied magnetic field with movement in 10^{-1} millimeter

scale. The following table was presented in *Hans* work. It clearly illustrates some advantages of using electromagnetic actuations in MEMS [58].

Table 6: Comparison Chart of different actuation method used in MEMS

ACTUATION METHOD	POWER /VOLTAGE	SPEED /MOTION
Piezoelectric [62]	300 V	100 Hz, 1mm
Electrostatic Comb Drive [63]	80 V	200-10K Hz
Electrothermal [64]	5280 mW	20 Hz, 140 μm
Electrostatic [65]	75 V	> 100Hz
Electromagnetic [66]	9 mW	> 500 Hz

Fabrication of magnetic spider silk has also been previously reported. In 1998 work by *Mayes et. al*, silk's reversible transformation to a supercontracted state when placed in polar organic solvent is used to functionalize the fibers in an aqueous based interaction [67]. Natural spider silk fiber obtained from *Nephila edulis* is dipped into a water or water/methanol sol containing 10 – 20 nm diameter superparamagnetic magnetite particles for 2 minutes. The fiber is then withdrawn and allowed to dry in ambient temperature. The result is a dark brown fiber coated with magnetite nanocrystallites. Spider silk was able to be functionalized with several other forms of material or magnetites. With no detailed magnetic characterization, the material was found to be magnetic by using image of a functionalized fiber being attracted to a permanent magnet. However, using energy disperse X-ray, they were able to find concentration of iron in the finished coating, thus, support the new found method in functionalizing the silk fiber.

In this particular chapter, a new fabrication method and characterization will be outlined for making of a magnetic spider silk beam using regenerated spider silk solution and ferromagnetic particles.

4.2 Fabrication Method for Composite Beam

Particles were purchased from Electronic Space Product International. Two samples were obtained: Fe/Ni 1:1 powder (with no specification on particle size) and Ni powder with 2.6 micron specifications. The silk was dissolved in a 1,1,1,3,3,3 hexafluoro-2-propanol (HFIP)

solution (Sigma-Aldrich) with a ratio of 1% w/w. Once dissolved, the powders were physically mixed with the solution.

4.2.1 Fe/Ni 50% Powder

The Fe/Ni sample was significantly larger than the Ni particles by eye inspection. Once the particles are mixed into the spider silk solution, they immediately fell to the bottom due to weight. Sonication for 1 minute was incorporate into the process in attempt to suspend the particles. However, due to low viscosity of the solution, this method was not effective. The solution was then increased in spider silk concentration up to 5%. It appears that not enough solvent is used to adequately dissolve the silk, thus can not be mixed properly. Therefore, the dilution was reduced to 3% w/w. The particles remain to be too heavy for suspension after stirring and mixing.

Since mixing the solution is not an option, another method was implemented to obtain a magnetic beam. One layer of the spider silk solution was deposited onto the sugar filled hole as illustrated in Figure 20. The Fe/Ni particle was then sprinkled onto the wet beam by hand, as evenly as possible. Then, another layer of the spider silk solution was deposited on top to create a sandwich like structure, where a thin layer of particles are coated on both side with a layer of spider silk solution. Once this beam is hardened, it was release by water. Detail of fabricating a micro bridge is illustrated in chapter 2.

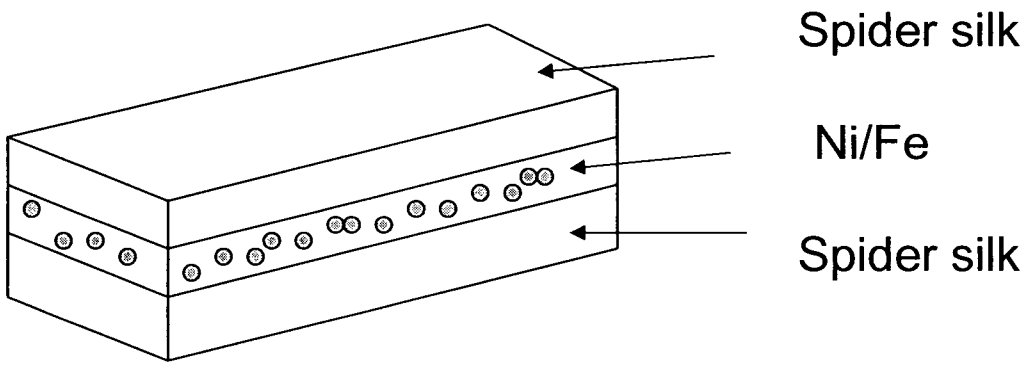

Figure 20: Illustration of Fe/Ni beam

4.2.2 Ni powder with 2.6 microns in diameter

The Ni powder, smaller in size, was easily mixed with the 1% w/w spider silk solution with a dilution of 15% w/w. Due to the particle density, after stirring and shaking the mixture, the particles slowly precipitated to the bottom. This takes approximately 30 seconds. This time window is long enough to collect the mixture in a syringe and deposit it to form a beam structure.

Previous research had used ferromagnetic gel consist of 30% Ni particles by weight mixed with epoxy to coat optical fibers [57, 58]. This mixing model is not realistic in this case because the volumetric ratio of particles to solution is higher, so a 30% w/w mixture would completely saturate the solution matrix resulting in wetted particles, rather than a mixed solution. Through gradually adding Ni particles to the solution, a mixture of approximately 15% w/w dilution appears to be acceptable.

4.3 Fe/Ni Beam

Figure 21 below shows the beam movement in the presence of an external magnetic field. A plastic fixture is made in order to obtain a longer beam for easier detection of the beam movements.

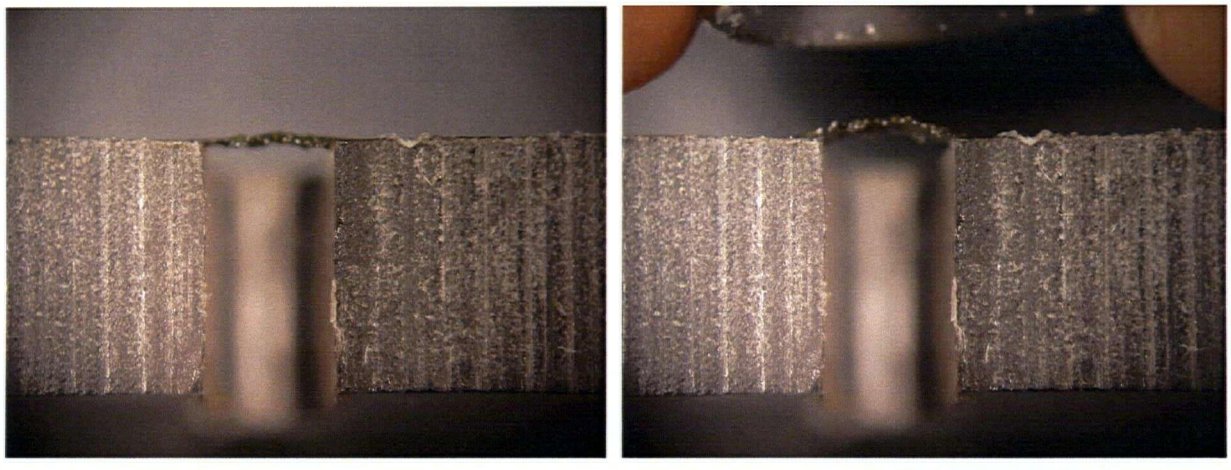

Figure 21: Fe/Ni 50% spider silk beam

The final beam is mainly consist of particles, thus the surface appear very rough and reflective. It was also difficult to obtain an evenly distributed particle layer as the amount and the location of the particles were hard to control. Therefore, the beam does not only move up and down, it also

tilts on an angle depending on the distribution of Fe/Ni particles. This method was successful in showing the design concept, however, there is a lack of control over the beam movements, therefore, no additional experiments were performed on the Fe/Ni spider silk beam.

4.4 Ni particle beam

Ni spider silk solution performed better in forming a more evenly distributed composite beam. The beam appears black in colour, and have no large visible particles, like the ones seen in Fe/Ni beams.

4.4.1 SEM image

SEM images were taken to examine the Ni spider silk film deposited on silicon substrate.

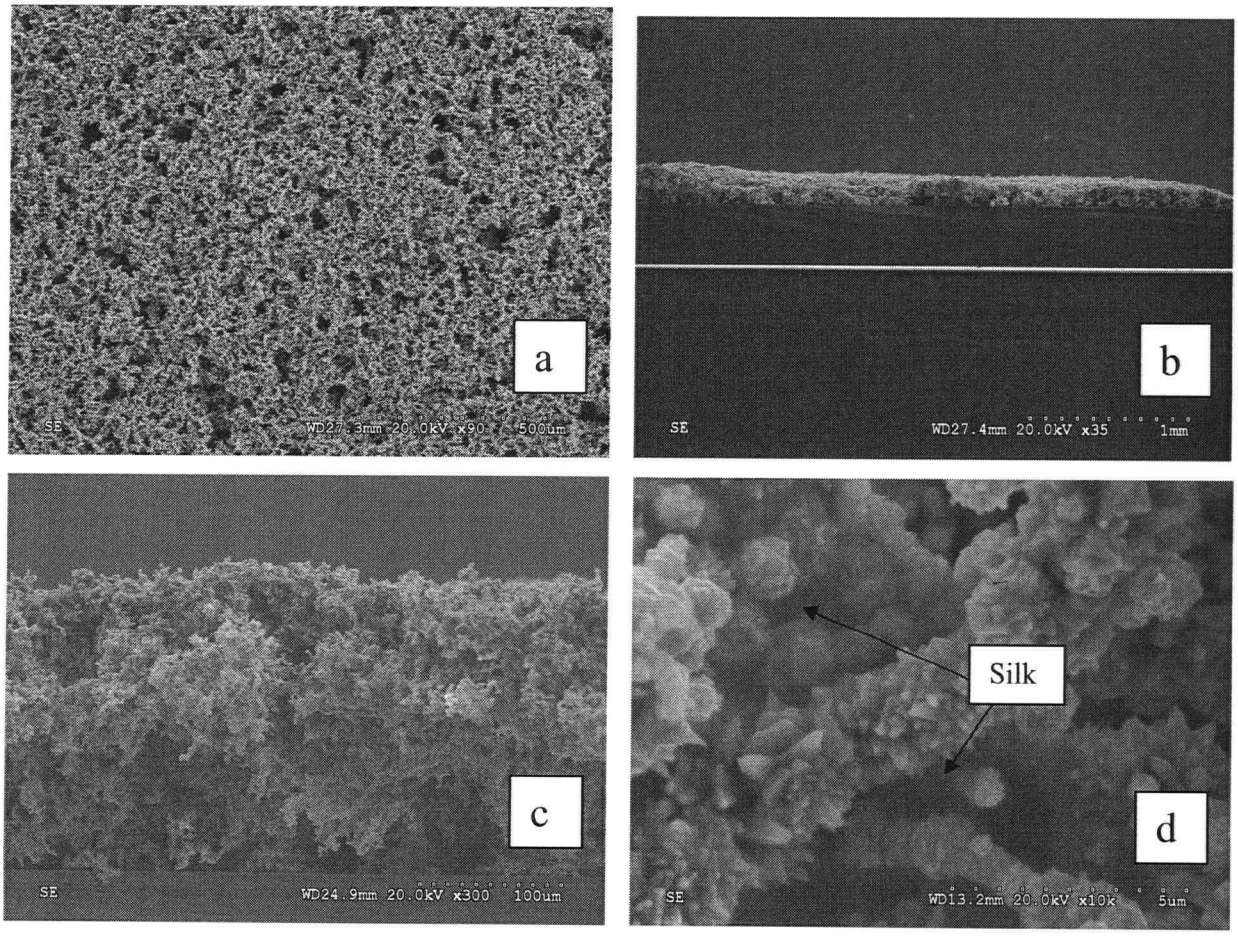

Figure 22: SEM imaging of Ni-spider silk film (a) x90 top view (b) x35 cross section view (c) x300 cross section view (d) x10k top view

The film was found to be porous with rough surfaces. Figure 22(a) and (b) illustrate the top and cross sectional view of the film respectively. The porosity of the film is clearly illustrated in the

two figures. By increasing the magnification (Figure 22(c)), we can see that the porosity is consistent throughout the film. The structure also shows conformation where the particles are branching in all directions. In Figure 22(d), which shows the film at 10k magnification, we can see that the particles are either covered or joined together by spider silk. The silk appear in the gray areas pointed out in Figure 22 (d). The silk thus plays an important role in providing structure support.

In order to understand whether this morphology is a result of the spider silk, or of the Ni particles, a SEM image of pure Ni sample was taken. The film was formed by using pure Ni particles and dissolving them into methanol. This mixture was then deposited onto a silicon chip. The methanol evaporated immediately, leaving a layer of Ni powder.

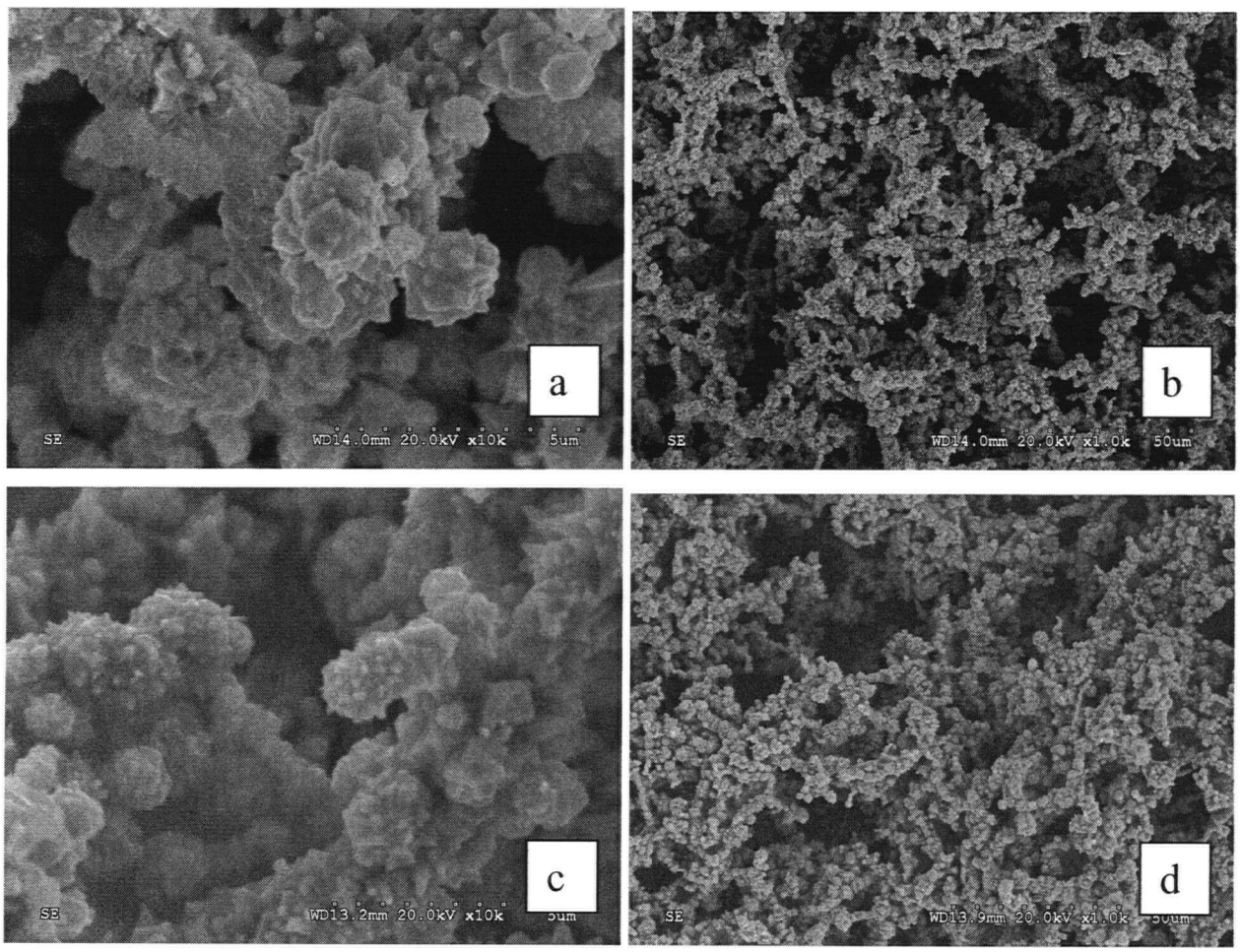

Figure 23: Comparison between pure Ni sample and Ni-spider silk sample a) x10k Ni b) x1k Ni c) x10k Ni-Spider silk d) x1k Ni-spider silk

Figure 23 compares the morphology of pure Ni film with Ni spider silk film. The pure Ni particles

in figures 23(a) and 23(b) are likely to be held together by van der Waals forces. This stacking formation is apparent in both pure Ni and Ni spider silk film. This confirms that the morphology of the Ni spider silk material follows the packing preferences of the Ni particles, with the spider silk film working as a glue-like matrix to maintain the structure. The spikes shown on the particles are inherent of the Ni samples, and are not a result of spider silk coating. These spikes appear less distinctive in 23 (c) in comparison to 23 (a), this further confirms that the spider silk material is dispersed amount the particles, thus reveal less details of the particle shapes.

4.4.2 Mechanical property

A fracture test was performed on the Ni-spider silk bridge using a nano indenter. This process was outlined in chapter 3. The material properties of the film are significantly lower than regenerated spider silk. The ultimate tensile stress and strain were found to be 2.1 MPa and 1.1% respectively.

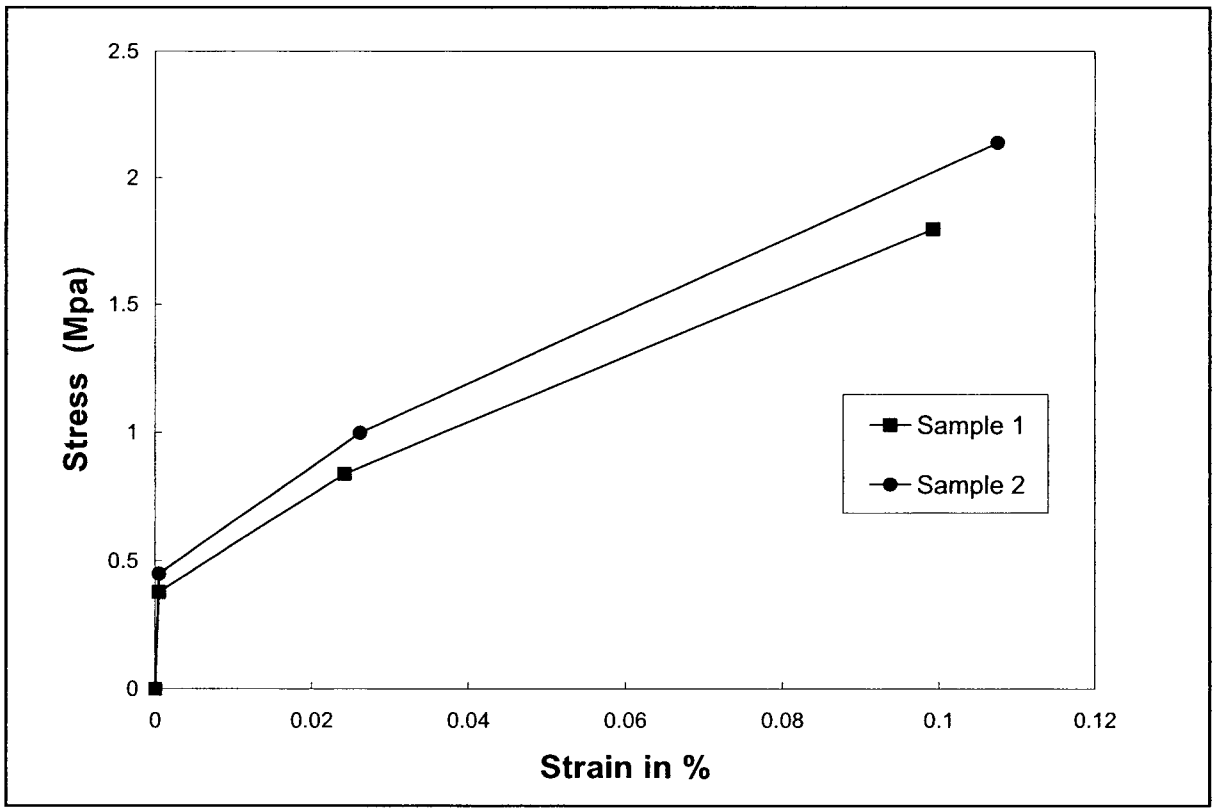

Figure 24: Fracture test stress vs. strain curve

This significant drop in material property in comparison to regenerated spider silk film (discussed in chapter 3) is due to the porosity of the material, where its morphology resulted in a

high number of stress concentrations found throughout the film. With such low maximum strain, the material is shown to be very low in ductility. The material property should improve if the dilution was reduced significantly. In this initial study, the maximum dilution was used in order to increase the material's magnetic properties

4.4.3 Magnetic property

Review on SQUID magnetometer

The Superconducting Quantum Interference Device (SQUID) is the most sensitive instrument for measuring magnetic field [68, 69]. It is based on the electric currents and magnetic fields interaction which occurs when certain material are cooled below the super conducting transition temperature [69]. This is the temperature at which material has no resistance to electricity flow.

The setup consists of two super conductors separated by thin insulating layers to form two parallel Josephson junction. Device based on this characteristic are used in high speed circuits. The functions can be designed to switch in times of a few picoseconds. A current is induced in the super conductors, and oscillating voltage is measured at the two junctions. Any magnetic flux change as a result of the sample will be sensed by a change in this oscillating voltage [60].

Experimental methods

A Quantum Design RSO SQUID magnetometer at 300K was used to test the film samples. The Reciprocating Sample Option (RSO) allow DC magnetization data with faster acquisition time while maintain high sensitivity [70].

The Ni spider silk solution was mixed at 1% ratio, and was then deposited onto a 3x3 mm^2 silicon chip. The sample piece is considered to be point source, therefore by specification, the sample must be smaller than 5x5 mm^2 in size. The sample is mounted onto a Quartz rod using a General Electric made special resin. Once securely attached, a clear straw was used to cover this sample mounted rod. Oxygen has paramagnetic properties, and thus is not desired in the SQUID. In order to avoid any oxygen trapped within the sample rod and the straw, small holes were placed along the straw cover. Once the sample was ready, it was attached to a carbon fiber rod

and inserted into the magnetometer chamber carefully. The temperature in the SQUID is controlled by helium heating. The sample is initially tested at 0 Oe and 300K.

Once data is collected, a correction factor due to the silicon substrate must be incorporated. The raw data obtained from the SQUID is the total magnetization. This is the result of magnetization of the thin film (ferromagnetic) plus that of the silicon substrate (diamagnetic). This is shown in figure below.

$$M_{total} = M_{thin\ film} + M_{Si}$$

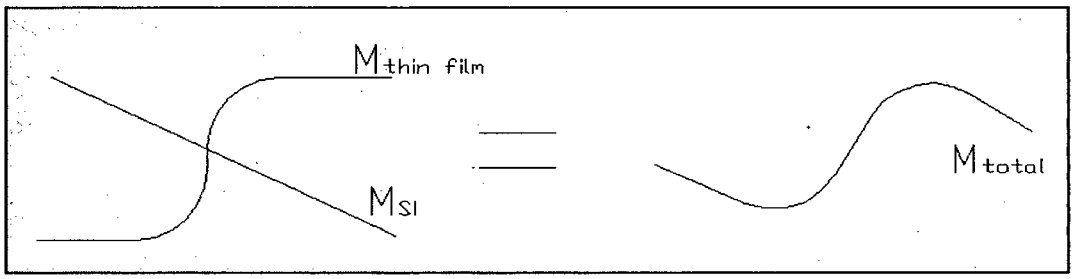

Figure 25: Final moment curve is consist of moment curve of the thin film and of the silicon substrate

Assuming that each end point of the M_{total} hysteresis curve represent the saturation magnetization, and its slope represent the slope of the M_{si} curve; if the M_{si} curve has a linear slope,

$$M_{Si} = x \bullet H$$

$$\approx \frac{\Delta M}{\Delta H} \bullet H$$

where H is the magnetization field and M is the magnetization of the sample.

Therefore, using the average value of the slope at the end points of the M_{total} curve, a correction factor can be found. This factor is then used to convert M_{total} data to $M_{thin\ film}$ data.

$$M_{thin\ film} = M_{total} - M_{si} = M_{total} - \text{avg}\left(\frac{\Delta M}{\Delta H}\right) \bullet H$$

Result

Figure 26 shows the magnetic hysteresis loop measured using a Quantum Design RSO SQUID magnetometer at 300K. The saturation magnetization (Ms), coercivity, and remenance ratio (Mr/Ms) were found to be 0.028 emu/g, 74 Oe and 13.4%, respectively. These measurements were performed on a 14% w/w mixed sample. Compare these data with bulk Ni, which has Ms,

coercivity and remenance ratio of 55 emu/g, 100 Oe and 5% respectively [101], we can see that the saturation magnetization for our samples is significantly lower than bulk Ni. The hysteresis loop shows the material to be ferromagnetic. It has a low coercivity similar to that of pure Ni, showing that it is a soft magnetic material.

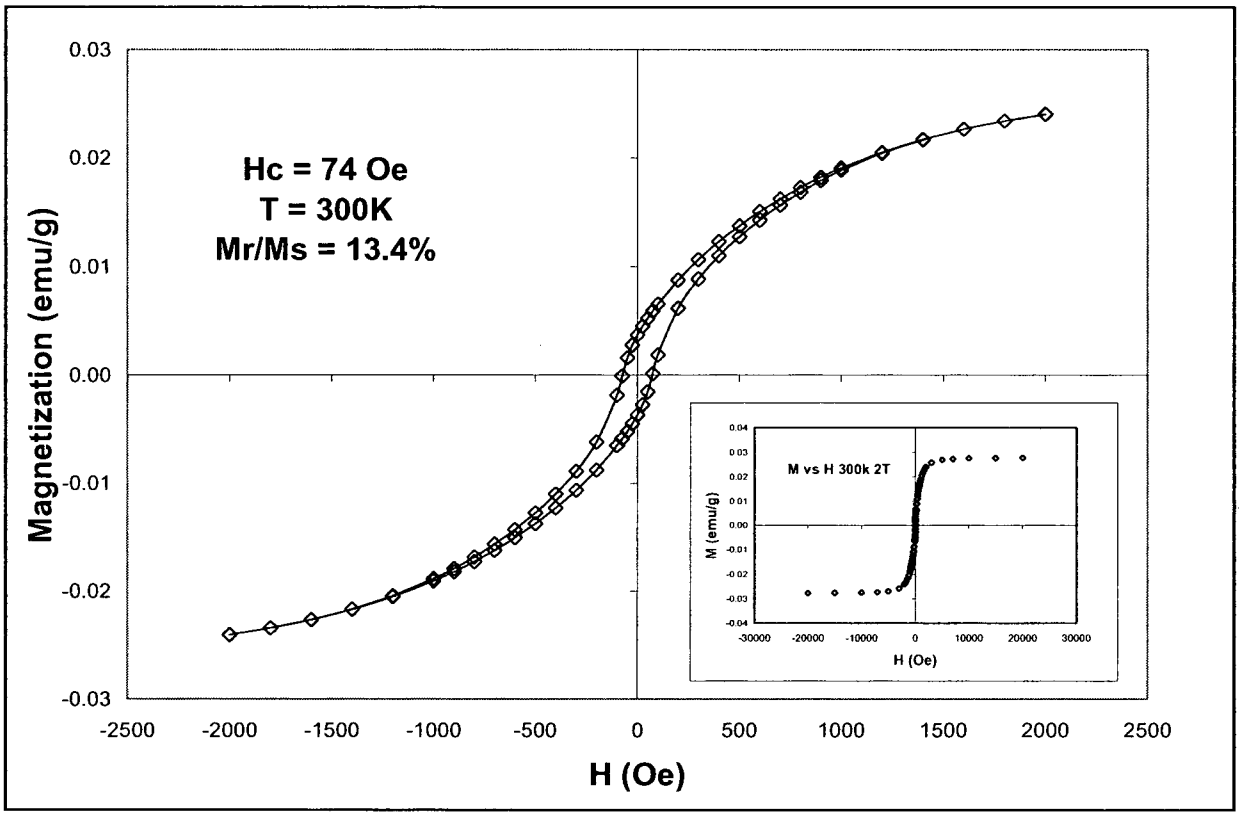

Figure 26: Ni-spider silk M-H hysteresis loop

4.5 Magnetic actuated beam

4.5.1 Experimental method

A free standing microbridge was formed using sugar as a sacrificial layer. Once the beam was stiffened slightly (approximately 15-20 minutes after release), a scalpel was used to lightly remove one fixed end. This created a cantilever beam, which will be more susceptible to the external magnetic field. The sample was then dried in ambient temperature for 75 minutes and the static testing was carried out. Once this was completed, the test was repeated at a drying time of 7.5 hours and 24 hours.

The static testing involved use of a microscope, a plastic sample holder, and a fixture where the magnetic field can be varied by moving the permanent magnet. The setup is shown in Figure 27.

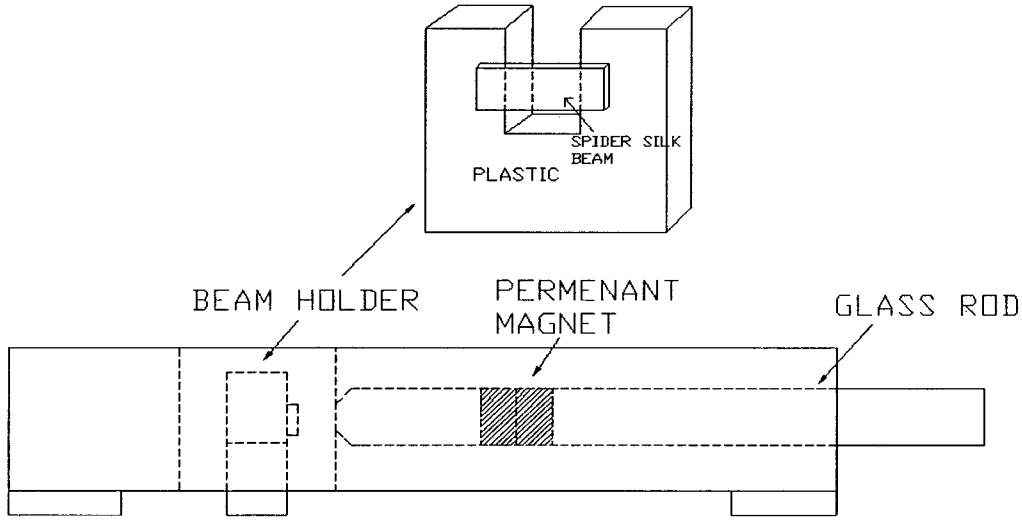

Figure 27: Bending Test Set Up diagram

Two cylindrically shaped permanent magnets were stacked on top of each other, with one side attached to a glass rod using epoxy. A glass rod was chosen to maintain a strong magnetic field. If the holder contained metallic or magnetic material, the magnetic field created by the two permanent magnets could be dispersed. A simple illustration of the magnetic fields is shown in Figure 28.

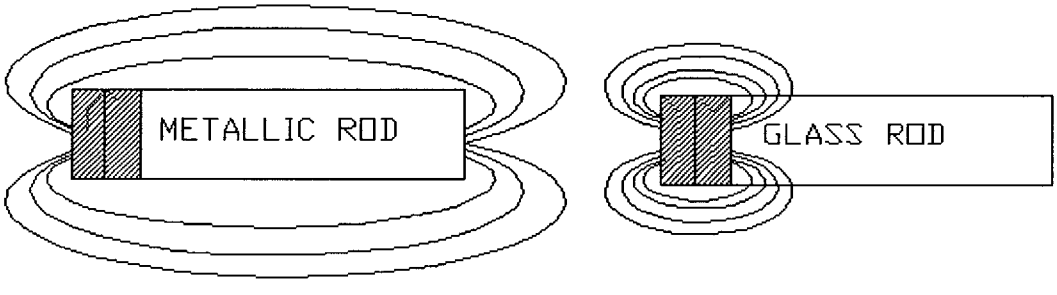

Figure 28: Illustration of magnetic flux lines along metallic and glass rods

4.5.2 Static bending data results and discussion

The magnetic induction created by the permanent magnet was mapped using a FW BELL handheld gaussmeter model 4048. As the distance from the permanent magnet decreased, the magnetic induction increased.

Review of hall effect gaussmeter

The gaussmeter uses the Hall Effect phenomenon to detect the magnetic field (flux density) of both AC and DC fields. It uses a transverse or an axial probe to give the magnetic strength reading. Mounted on the tip of the probe is a hall generator which is made of a four terminal semiconductor. An input current is applied to the hall generator and an output signal is produced. This signal is proportional to the magnetic field passing through it [69, 71]. The basic make up of the probe is shown in Figure 29. Figure 30 illustrate the mapping of the magnetic field using a transverse probe.

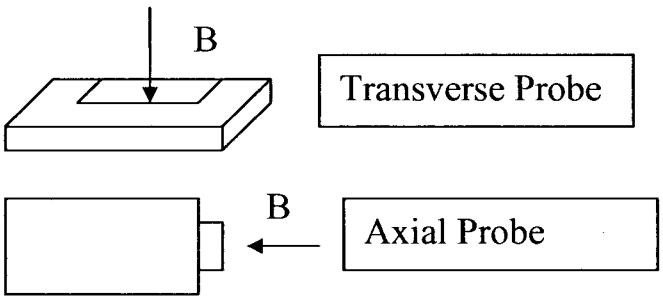

Figure 29: Illustration of transverse and axial probes [71]

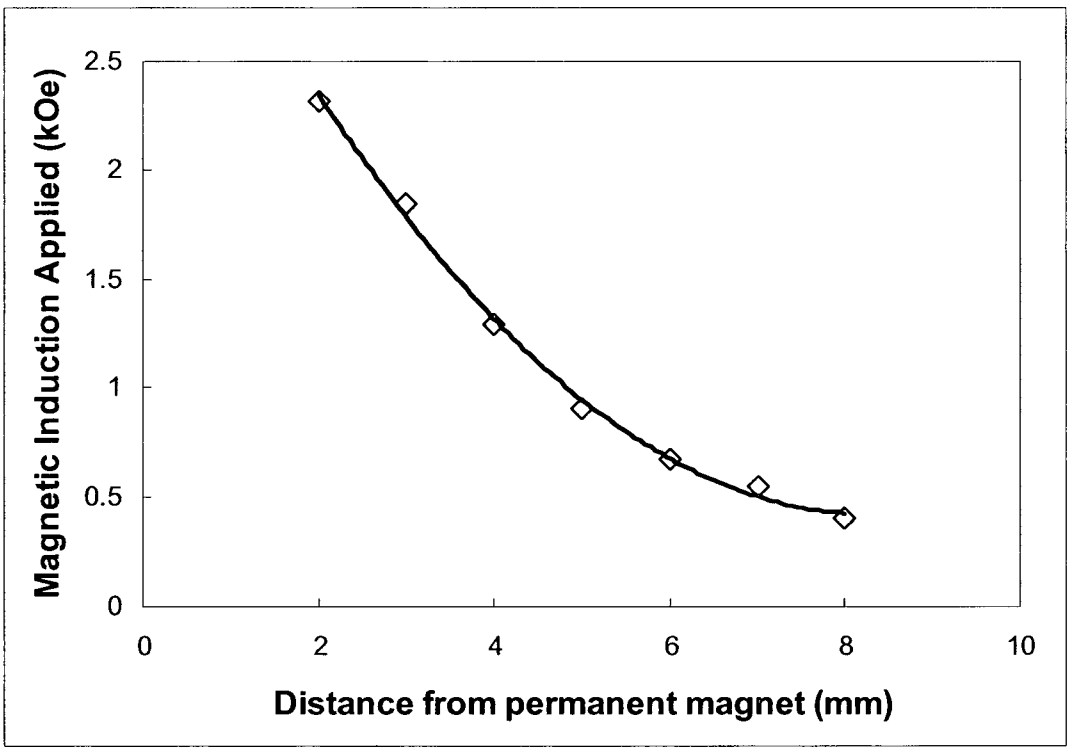

Figure 30: Magnetic induction (field) applied by the permanent magnet as the distance changes

We can now predict the magnetic field strength of the permanent magnets by knowing the distance between the beam and the magnets. This change in field strength can then be plotted against the amount of bending in the beam. Figure 31 provides sample pictures used to measure the amount of bending that occurred.

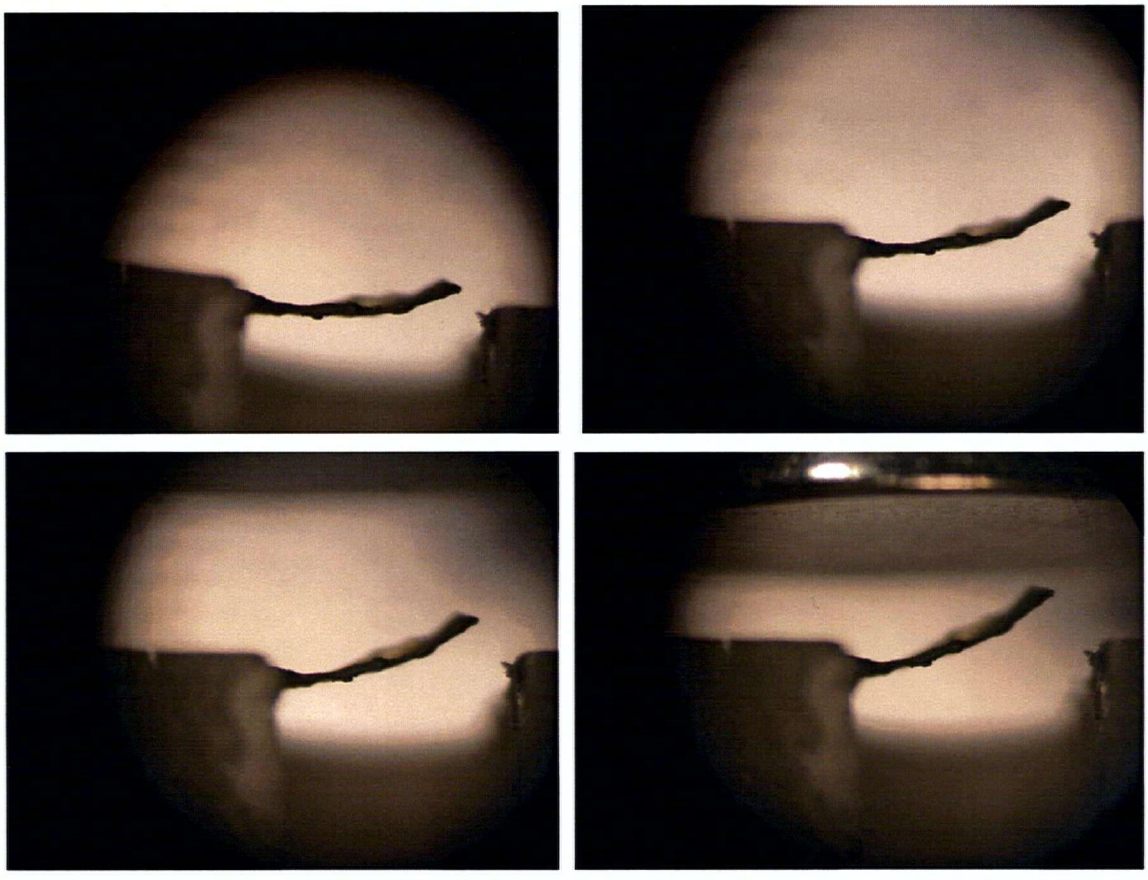

Figure 31: Images used to measure bending movement of the beam under increasing magnetic field. Sample size 3.25 x 0.98 x 0.17 mm (Length x Width x Thickness)

Figure 32 illustrates the displacement of the beam as the magnetic field strength increases. There does not seem to be any significant difference between the samples. The error bars of the three data sets overlap each other, except for the points lying on 1.3 kG magnetic induction. The error bars are provided based on the maximum and minimum value collected for the same image. Overall, no significant differences can be seen across the bending results for their allotted drying time provided that there is a minimum drying time of 75 minutes.

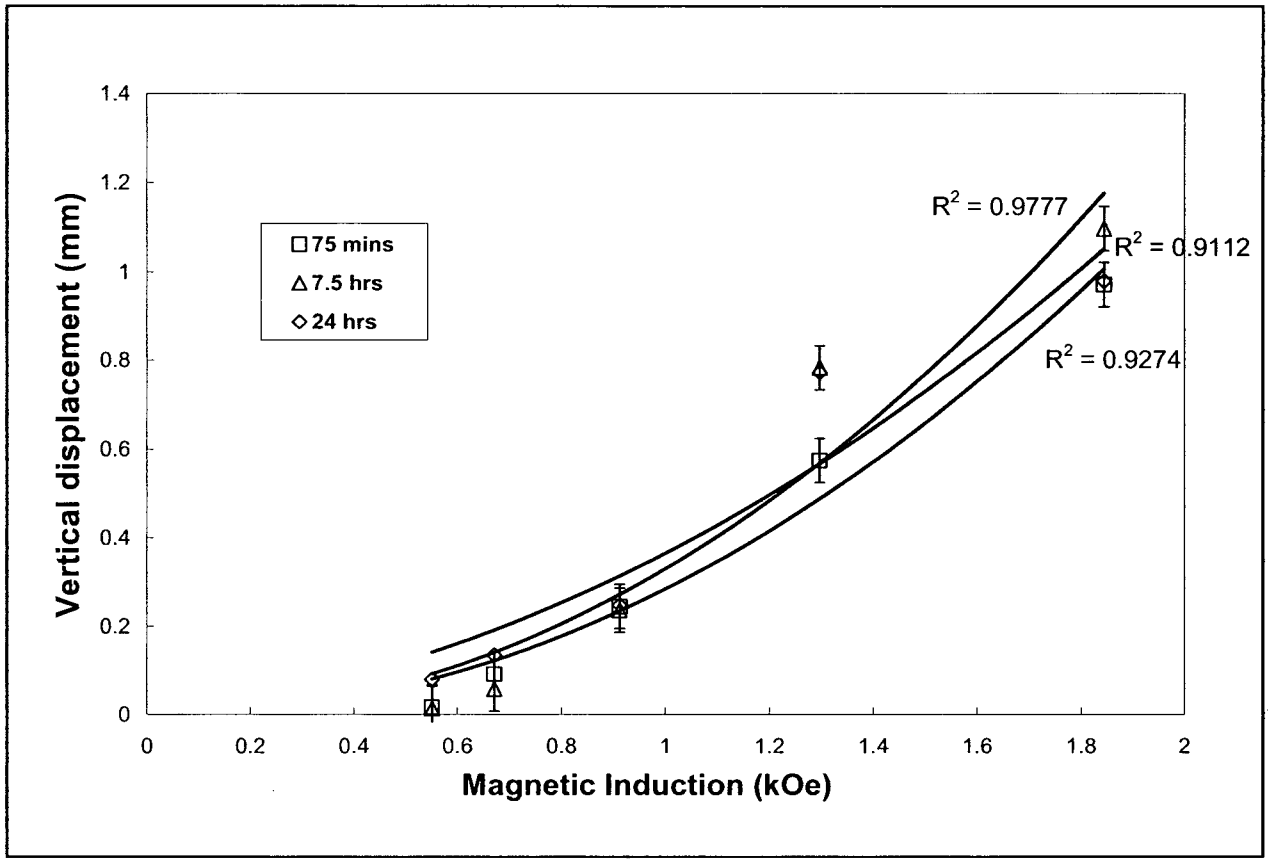

Figure 32: Bending distance as magnetic induction (field) increases

4.5.3 Dynamic bending data results and discussion

Using a Laser Doppler Vibrometer (LDV), a dynamic testing was performed. A solenoid with external magnetic field of 0.6 mT was used to actuate the Ni spider silk beam. It was purchased from Magnetic Sensor Systems. As the LDV shined a laser ray onto the Ni spider silk beam, the beam's movement actuated by the solenoid was detected and sent to the output signal port. The response of the Ni spider silk beam is shown in Figure 33 below. The Top signal is the response, and the bottom signal is the sinusoidal input signal from the solenoid. We can see that the maximum peak to peak obtained in this case is 1.6 μm. This is found using a conversion of 2 μm per Volt.

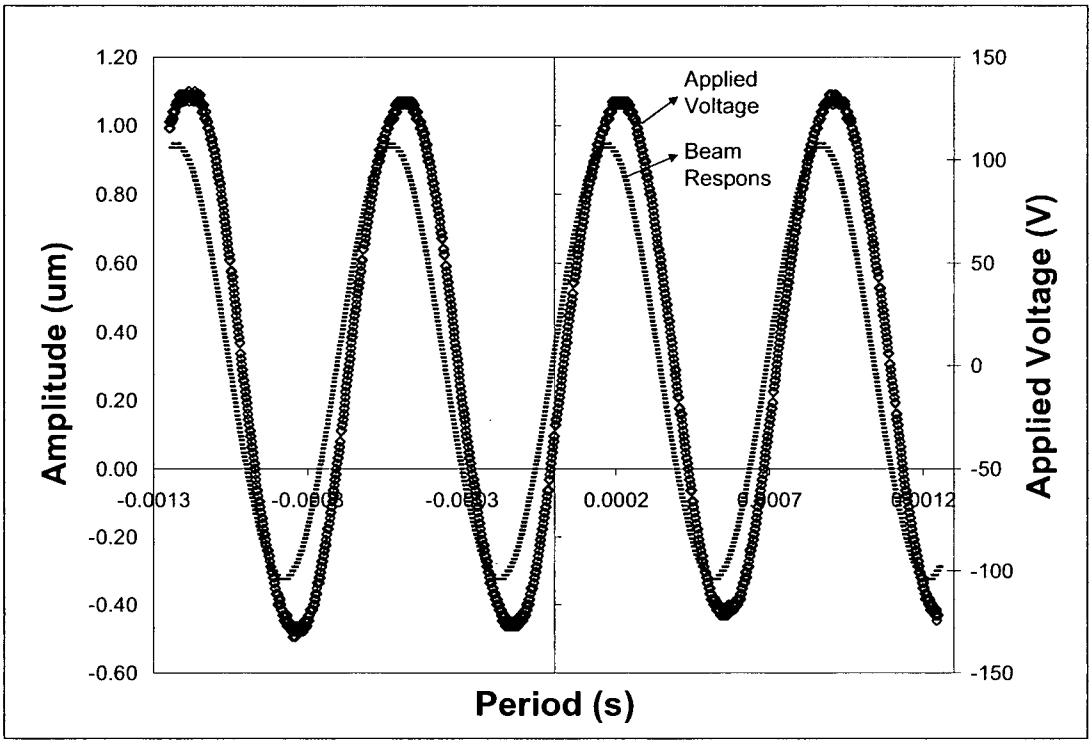

Figure 33: Dynamic test data using solenoid. Top signal is response of Ni spider silk beam, bottom signal is the applied signal from the solenoid.

4.6 Summary

This work has demonstrated that spider silk can be used as a matrix for creating new composite biomaterials. By mixing Ni particles within this matrix, we have shown a proof-of-concept method of creating a magnetically actuated spider silk composite. In addition, we have characterized its material, magnetic and static bending properties.

The amount of Ni powder used in this experiment led to a near maximum dilution. This contributed to the material's porosity, and thus resulted in a brittle composite. In future work, in order to increase its material properties, smaller Ni dilution can be tested. However, this will lead to a reduction in magnetic properties. The final goal will be to strike a balance between magnetic and material properties by varying the dilution.

It is recommended that additional methods be incorporated into the experiments. For example, oleic acid may be used to coat the particle. Since it is a fatty acid, similar to that of lard, it might help the particles to be more dispersed in solution. It has been used in processes of forming nano size particles. [75] This could help to improve suspension of Ni particles in spider silk solutions.

CHAPTER 5

Spider Silk Beam Using Iron Carbonyl for Magnetic Actuation

In this chapter, a fabrication method is outlined for creating a magnetic composite using spider silk as the matrix. By eliminating usage of particles, improvements in uniformity as well as mechanical property can be seen. Therefore, iron pentacarbonyl solution is used here to create an iron spider silk composite. By using different concentrations of regenerated spider silk solution, both the film itself and nano spheres containing iron can be formed. Some of these particles form on top of films, and some form as clusters of iron/iron oxide bound by spider silk proteins. This special binding property between spider silk proteins and iron/iron oxide is shown here for the first time.

5.1 Theory

Iron

Iron is an active component in many living systems. It is responsible for oxygen transport and electron transport and it is found in many proteins that exist in our bodies. Important iron-containing proteins such as hemoglobin, transferrin and ferritin, perform important functions in the transport and storage of iron [72].

One of iron's uses is for therapeutic purposes. Oral and intravenous methods of delivery have been developed to help chronic health problems such as renal anemia and cardiovascular complications. Of the two, the oral delivery method is the more common, partly because it is viewed as the safer option. Iron is generally given orally in iron sucrose that is absorbed into the

bloodstream and binds to transferring protein. It is then transported to bone marrow for storage or use. In other situations, it has been used to bind and form heme, which subsequently forms hemoglobin molecules [73]. This binding process between iron and proteins is something that is common in our bodies. An example of a heme group containing iron is shown in Figure 34. As iron sucrose is dissolved into the body, Fe^{2+} ion atom formed. It is then bonded to 4 neighboring nitrogen atoms to form heme. The heme will then bind with polypeptides to form final hemoglobin proteins.

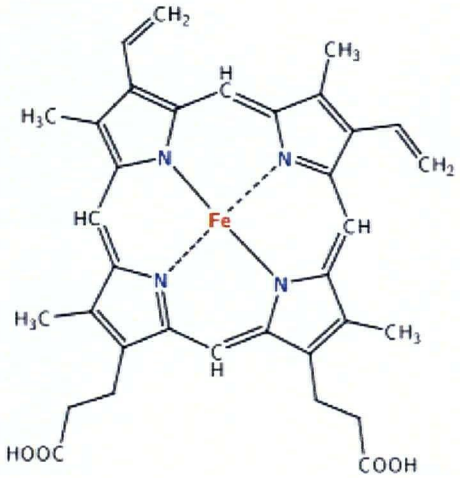

Figure 34: Illustration of heme group, showing binding of iron to rest of the heme group molecules

Iron has also been used in concert with protein and peptides for biomedical applications, specifically for diagnostic and therapeutic purposes. Iron also has the potential to be turned into magnetic ink or fluids, or used in recording media for diagnostic purposes [74]. Further more, iron containing biomaterials can be used for magnetically activated micro-sensors and actuators for biomedical applications.

Iron is also an abundant element around us. Being one of the three main ferromagnetic materials (Ni, Co, Fe), it has been widely applied for its magnetic properties.

Iron Pentacarbonyl

Iron pentacarbonyl belongs to the homoleptic group of chemical compounds. This means that it is a metal compound with all ligands identical (CO ligands). Reflecting its symmetrical structure, $Fe(CO)_5$ is volatile, and one of the most frequently encountered liquid metal complexes.

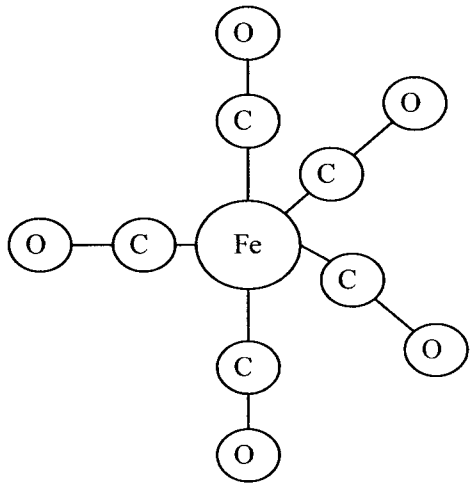

Figure 35: 3-D model of $Fe(CO)_5$

Several magnetic oxide nanoparticles, including γ-Fe_2O_3 and magnetite, have been synthesized by using microemulsion, electrochemical deposition, and other methods [75, 76]. Nanoparticle sizes between 4-16 nm have been observed. Composite films consisting of iron-iron oxide have also been achieved through chemical vapour deposition of iron pentacarbonyl [77]. More importantly, polymer coated magnetic nanoparticles have been fabricated using thermal deposition. This is performed in presence of ammonia and polymeric dispersants. These dispersant include polyisobutylene, polyethylene, a short polyethleneimine chain and polystyrene chains functionalized with tetraehtylenepentamine [74, 78].

In this work, instead of thermally or chemically decomposing iron pentacarbonyl, UV light is used to break the bond between the Fe and the CO groups. Once this bond is broken, carbonyl will evaporate, leaving Fe atom to form particles. Since iron is hardly ever found in its elemental state, it is like to see particles appearing in forms of iron oxide or with binding to iron such as heme shown in Figure 34. These nanoparticles will be formed within the spider silk film to create a new magnetic spider silk composite. This will be performed under normal room temperature without high pressured conditions.

5.2 Experimental Method

5.2.1 General method

Iron pentacarbonyl was purchased from *Sigma Aldrich*. When purchased, it was in a liquid state with a low boiling point and sensitivity to UV light. Therefore, it had to be kept refrigerated, and far from any light source with UV components. The mixture was diluted in 2:1 v/v (spider silk solution vs. $Fe(CO)_5$), as well as 1:1 v/v ratio. Once the two solutions were mixed, the mixture was then deposited onto silicon for forming thin films. These films were then exposed under an Entela model UVG-54 handheld short wave UV lamp. This was performed for 2 to 3 hours.

5.2.2 Discussion on experimental methods

The iron pentacarbonyl solution had an orange colour, which was carried through into the final mixtures. The two solutions appeared to mix well together, and no phase separation was observed. Since the work was completed under white light, it was important to try to minimize the amount of light exposure to the solution. This was done by either wrapping the bottle in tin foil or keeping the sample in a closed box.

It was found that after approximately 25 minutes (this time length shorter if the volume/amount of the mixed solution being observed is smaller), the solution became a gel-like substance, exhibiting sol-gel properties. In addition, as it changed state, the material changed colour from orange to dark brown. Due to this colour change, the solution had to be freshly mixed and deposited immediately after mixing was completed when creating the thin films or free standing bridges.

Since the mixture of $FeCO_5$ and spider silk has not been studied before, minimum amount of UV exposure time necessary to break the Fe-CO bond was unknown prior to this study. Therefore, a FTIR was completed for samples at different exposure times to study the reduction in peaks for the Fe-CO bond. The peaks for metal carbonyl, indicated in *Infrared and Raman Spectra of Inorganic and coordination compounds* [79] were 2116, 2030 or 1989 (cm^{-1}). The FTIR results are shown in Figure 36.

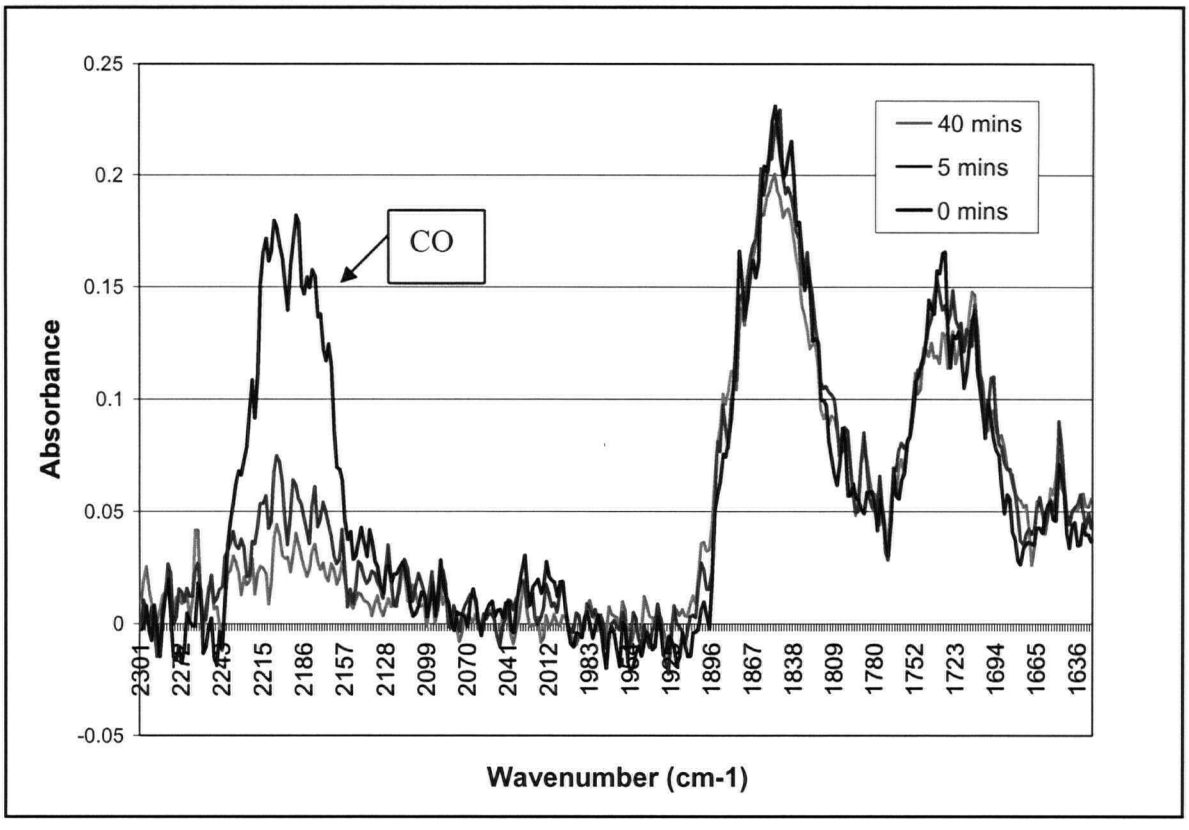

Figure 36: FTIR for determining UV exposure time

The carbonyl had a strong peak in the initial sample. Once the sample was subjected to UV light, the carbonyl immediately dropped in absorbance. After another 35 minutes, the carbonyl intensity decreased slowly until the peaks blended into the background noise. The test was performed on silicon substrate, and the noise was significantly higher than what might be found using Potassium Bromide plates instead. Even though this spectrum cannot be used for detailed FTIR analysis, it does provide a quick approximation of the necessary UV exposure time. The significant drop that occurred within the first 5 minutes is largely contributed by sublimation of $FeCO_5$, showing the high volatility of the solution.

It should also be noted that this sample was completed in yellow room with no UV rays, which is not the normal lab condition where most fabrication would take place. Under normal lab conditions, the material could be evaporating before it is deposited. This volatility reinforces the necessity of depositing the film onto the substrate immediately after mixing, as it is difficult to control sublimation in the lab conditions used in this study. Finally, since the noise level in this particular FTIR measurement was high, thus is it inconclusive as to exactly how long the

exposure time is needed. Therefore extra time was being allowed for UV exposure during experiments to ensure the maximum amount of Fe-CO bonds would be broken.

5.3 Fe spider silk thin film (1% w/w spider silk solution)

5.3.1 SEM image

SEM images were taken to examine the Fe spider silk film deposited on the silicon substrate. The sample appeared to exist in two phases: film and porous/fibrous-like area. This is indicated in Figure 37(a). The film area appears to be very thin because with 20KV exposure, we can see fiber-like subsurface materials that are similar in nature to the exposed fibrous areas. Since this opaqueness was never seen in pure spider silk films, we can suspect that the thickness of this film is less than 1 or 2 μm. Also visible are areas which appear to be a porous film, without the web-like features found in Figure 37(a). A higher magnification of this area is shown in Figure 37(b).

Both the fibrous and porous material could be partially explained by the solvents used. Both HFIP and $Fe(CO)_5$ are volatile solutions. They were mixed with a ratio of 1:1 v/v, resulting in more than 99.5% of the solution containing volatile solvents. As the solvent quickly evaporated, it mimicked the solvent extraction method used in creating porous materials [96].

However, the solvent volatility cannot be the only reason for formation of fibrous material. This is clear because when using the 0.5% w/w ratio of pure spider silk solution (with 99.5% of HFIP as the volatile solvent), a thin film was formed without any additional features. The same can be said when dilution that is even lower, as demonstrated by the images found in chapter 3. Therefore, it must be the particular use of $Fe(CO)_5$ that is responsible for the fibrous materials.

Figure 37(c) and (d) show a higher magnification, where spheres can be seen on the fiber-like material. These particles are approximately 0.1 - 1 μm in diameter. They appear to be brighter than the rest of the film. It is suspected that, since heavier elements tend to show up brighter in SEM (as they generate more back-scattered electrons used to image), the brighter area in the figures represents a higher concentration of Fe. This conclusion is bolstered by the fact that biomaterial on

its own is difficult to examine under SEM, as it is not conductive, and therefore any material that is dimmer in colour is expected to be less in Fe concentration. However, it is also necessary to keep in mind that due to the spherical shape of the particles, more back scattered electrons will also be produced for imaging. Therefore, this brightness could be a result of its shape, and not because of its conductivity.

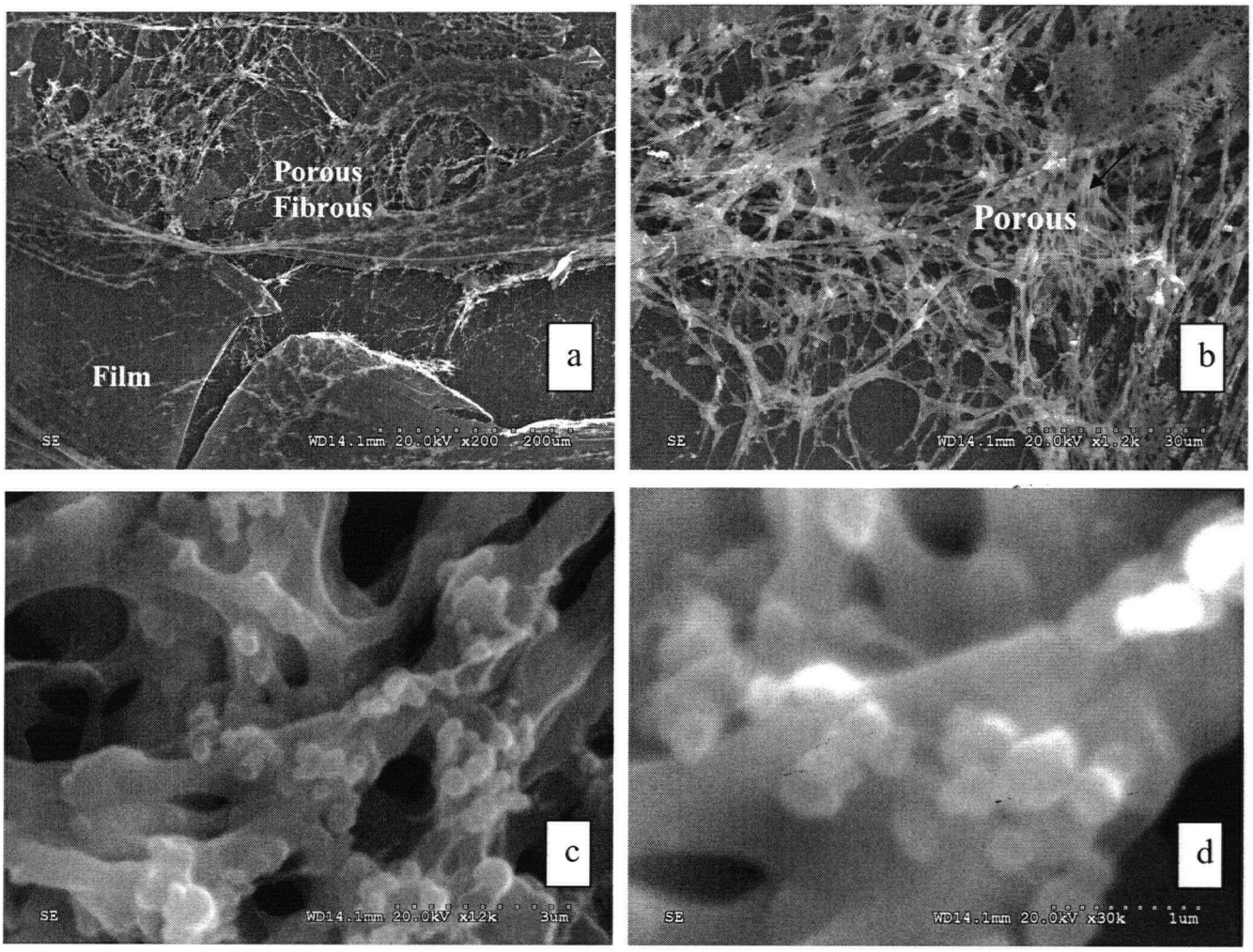

Figure 37: SEM image of 1% w/w silk mixed with $Fe(CO)_5$ with 1:1 v/v

The spheres in this image could not properly be studied without knowing what iron oxide particles look like. Therefore, a simple method of creating iron oxide particles was performed using pure $Fe(CO)_5$. From the literature on the subject, it was known that using pure $Fe(CO)_5$, nano particles can be produced in the form of iron oxide with a 10-30 nm diameter [97]. However, this method used in other studies is different than what was used here. Therefore, for comparative purposes in

this study, the UV exposure method outlined for iron spider silk film was performed on the pure $Fe(CO)_5$ solution. Using this method, the images in Figure 38 were obtained. The particles were found to be between 0.1 - 1 μm in diameter, which is similar in size when compared to the spheres formed on the iron spider silk film. The initial conclusion was that the spheres appearing in iron-spider silk solution were iron oxide particles.

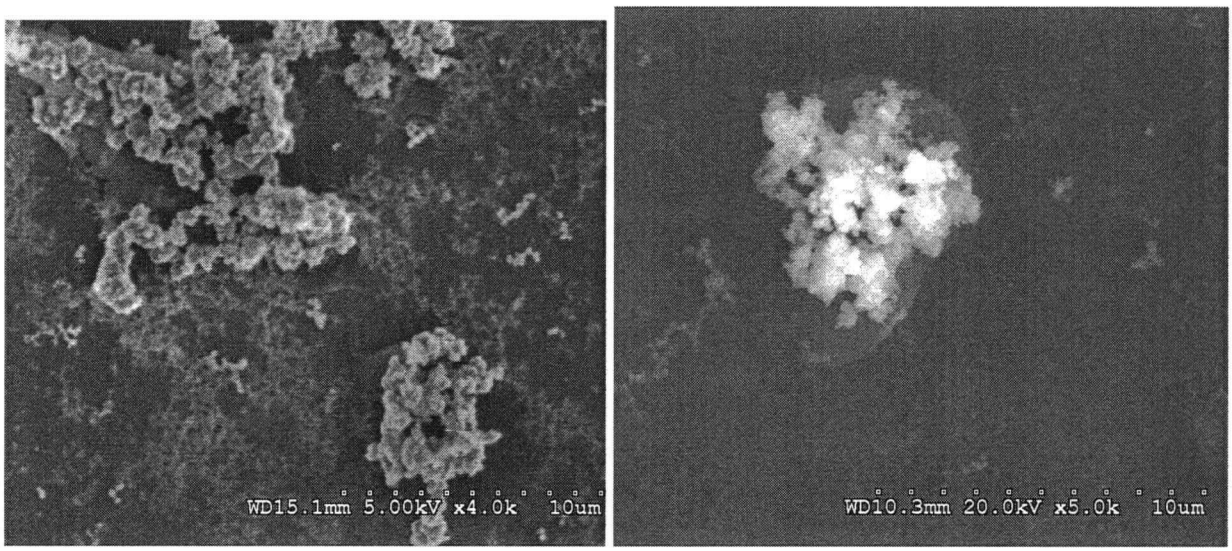

Figure 38: Iron Oxide particles formed after UV exposure of pure $Fe(CO)_5$

However, in reviewing Figure 37 and Figure 38, it is clear that surface appearance of the iron oxide spheres is much rougher than the ones created by the iron-spider silk solution. The shape of the spheres is also different. The iron-spider silk spheres appear much rounder with distinct spheres close to each other, whereas the particles shown in Figure 38 are closely packed with a large variety of spheres.

When comparing the spheres, it must also be remembered that diffusion is a factor that influences the final formation of iron oxide. In a pure $Fe(CO)_5$ sample, there is a higher concentration of iron atoms readily available for binding with oxygen, and thus forming oxide particles. In such a situation, it is easy for iron atoms to diffuse through the solution, and bind with others to form larger and closely packed particles. On the other hand, in our study, iron concentration within the iron spider silk solution was much lower. For iron to form iron oxide and then particles, it had to first diffuse through the spider silk solution. It is unusual then, that

the particles formed from iron spider silk solution would be similar in size to that of pure $Fe(CO)_5$. Accordingly, to demonstrate that the particles are different, we proceeded to examine the concentration of iron within the respective samples using X-ray EDS.

5.3.2 X-ray EDS

Review of X-ray EDS

An X-ray Energy Diffraction Spectroscopy (EDS) was performed by a Quartz X-one system integrated with a Hitachi S-300N Scanning Electron Microscope (SEM) [80]. The X-ray EDS is capable of obtaining information such as element composition and concentration.

This X-ray system analyzes element composition and concentration as follows: As the electron beam hits the sample, secondary back scattered electrons obtained from the SEM images are emitted. As the electrons bounce out of its position, the atom becomes unstable. Electrons in the outer shell then drop down into the inner shell in order to fill the recently created hole. Since outer shell electrons have more energy, the atom releases energy in the form of X-ray as these electrons drop into the inner shell. The energy and wavenumber of the X-ray indicate both its parent element and the identity of the shell the electron dropped from.

When one looks at an EDS spectrum, certain elements have several different X-ray peaks. This occurs because as the atomic number increases, so does the number of shells, and thus number of peaks are available for this element. The elements are quantified using the areas under each peak, and taking into account the accelerating beam voltage. A sensitivity factor is then produced and is used in converting these areas into concentration in weight percentage [81-83]. These weight percentages are obtained from the volume that is examined by the EDS. However, volume varies depending on the film property and beam voltage.

Accordingly, a Monte Carlo simulation is used to more accurately estimate the volume. When using the same bean voltage, heavier materials have a smaller penetration diameter in comparison to that of a lighter material. For example, under 20kV, Aluminum and carbon have a penetration depth of 5 micron and 10 micron respectively. Figure 39 illustrates the volume that is typically covered by EDS for carbon. Under the same film properties, a lower beam voltage will

cover a smaller volume. For example, Aluminum oxide can penetrate 2 microns with 20kV beam voltage, whereas a 5kV beam voltage will penetrate only 0.5 microns.

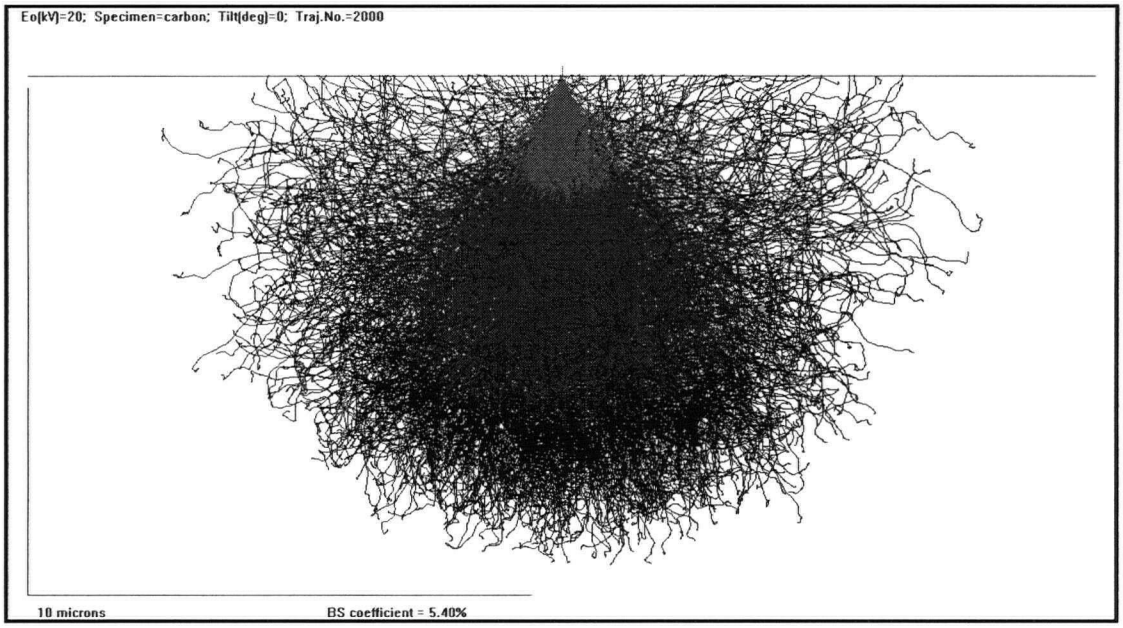

Figure 39: Monte Carlo simulation of carbon under 20kV beam exposure, 10 μ m is found as the exposure diameter

Results

Figure 40 represents the area used by the X-ray EDS. Three different locations were examined. Table 7 shows the iron concentration found at locations A, B and C.

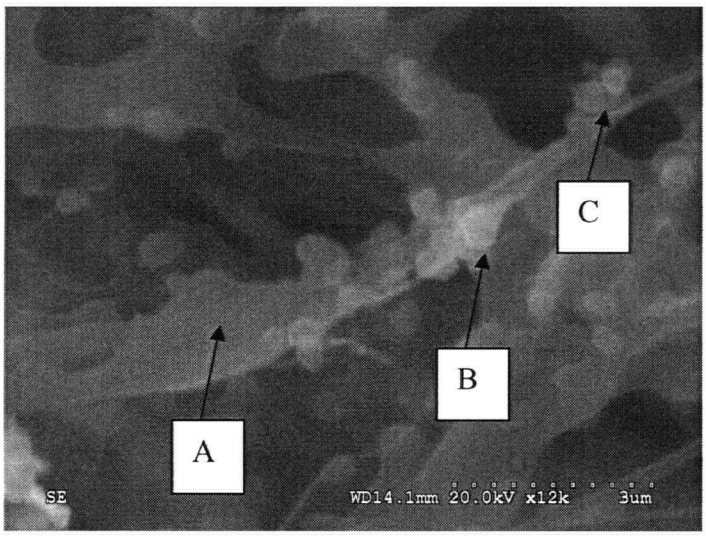

Figure 40: Image of the area used by X-ray EDS

Table 7: Fe wt% found using X-ray EDS at three locations indicated in Figure 40

	A	B	C
FE (wt%)	2.07	1.52	3.55

The spectroscopy identified all the elements found within the sample spectrum. A list of the main elements is found below in table 8.

Table 8: Concentration of main elements found within the X-ray EDS spectrum

	Concentration (wt%)	**Normalized Concentration (wt%)**
Carbon	33.93	40.62
Oxygen	7.26	18.91
Nitrogen	2.64	28.33
Fluorine	0.57	6.44
Aluminum	0.16	NA
Silicon	52.91	NA
Iron	**0.50**	**2.07**
Palladium	1.87	NA
Gold	0.15	NA

Carbon, oxygen and nitrogen represent organic material, in this case the spider silk. The large percentages of these organic elements found in the results shows that the particles are not mainly made up of iron, but rather spider silk. The solvent used in the spider silk solution contains fluorine, which explains its existence in the chart. Also, silicon appears predominantly in the sample. As the film is deposited on silicon substrate, this must mean that the EDS beam completely penetrated the material and reached into the silicon substrate. As for the remaining elements found in the sample, the gold and palladium were coated onto the film to help improve the imaging quality of biomaterial under SEM, and the aluminum comes from the sample holder. Once the elements were defined, materials that were not relevant to the sample (such as aluminum, silicon, gold and palladium) were deleted, and the wt% was normalized against the

remaining elements. The normalization was performed by the EDX after indicating the elements that were being eliminated.

The results show that low concentrations of Fe existed at all three locations. Originally, it was suspected that the brighter particle (B) would contain more Fe than the dimmer areas, C and A. The conflicting result could be explained by the fact that the material is very light and thus the EDS beam may have penetrated a large portion of the volume of the sample, preventing us from achieving accurate localized results. The actual coverage area of the EDX is difficult to predict since the Monte Carlo simulation require extensive material properties. However, since it is a lighter element than carbon, it is likely, that the coverage diameter is in the area of 10 μm or larger. Since it is possible that there are spheres on the under side of area A, or perhaps there is iron within the fiber-like area, it is difficult to distinguish where the iron peaks are coming from.

The initial concentration of iron contained in the mixture was 13.9 wt% (see the calculations in Appendix D). The final iron concentration is much more difficult to predict, since much of the HFIP and iron pentacarbonyl would likely to be evaporated prior to measurement. However, since the initial estimate is significantly higher than what was found in the material, we can conclude that the main content of the sphere and the fibrous material is spider silk.

Two types of iron oxide occur naturally: Fe_2O_3 or Fe_3O_4. Both contain ferromagnetic properties [98]. Relying on the molar mass of Fe and O, the concentration of Fe within these two oxides would be expected to be between 35%- 72%. It is more likely that based on the orange colour of the solution, which is normally seen on corroded iron (Fe_2O_3), we can suspect that iron oxide had formed in the film. This colour was found throughout the iron spider silk film. Iron oxide particles produced by pure $Fe(CO)_5$ showed a 36.2 wt% concentration of iron. This is significantly higher than what is found in iron spider silk material, and confirms that the spheres created by iron spider silk solution mainly contained spider silk material.

The EDS results and a sample spectrum for particles formed from pure $Fe(CO)_5$ are shown in table 9. The carbon content could be explained by carbonyl that was trapped in the film sample.

Table 9: Iron Oxide X-ray EDS wt% concentration of main elements

	Concentration (wt%)
Carbon	28.24
Oxygen	35.55
Iron	**36.21**

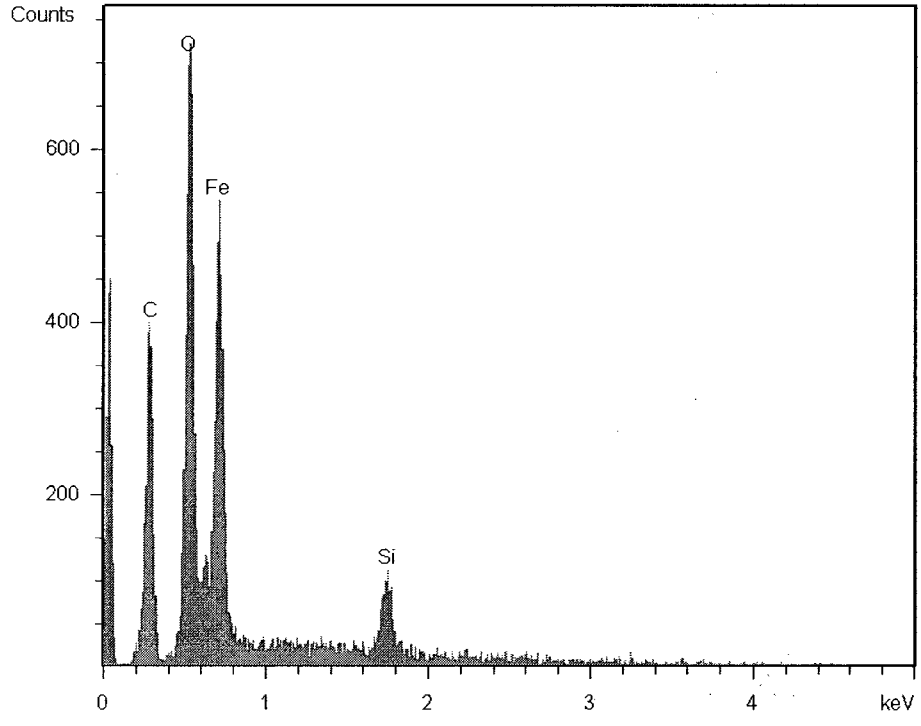

Figure 41: EDS spectrum of iron oxide formed from pure $Fe(CO)_5$

5.3.3 TEM images

Transmission Electron Microscope (TEM) images were taken by a Hitachi H-800 Electron Microscope. This was performed to specifically examine the spheres formed from the iron spider silk solution. TEM operates similar to that of shining a light (in this case an electron beam) through a material. The area that absorbs (blocks) light will show up darker and the area that is hollow will allow the light to either fully or partially shine through. When negatives of a TEM image are obtained, the colours are reversed: the light areas show substances that absorb more of the electron beam, and the darker areas are the less dense areas.

For our study, the iron spider silk solution was first dropped onto a 2x2 mm copper sheet with grids in the center. The sheet was coated with carbon in order to trap the samples as it dried. The sample was exposed to UV for 3 hour. The TEM films were developed in a dark room and then scanned in positively.

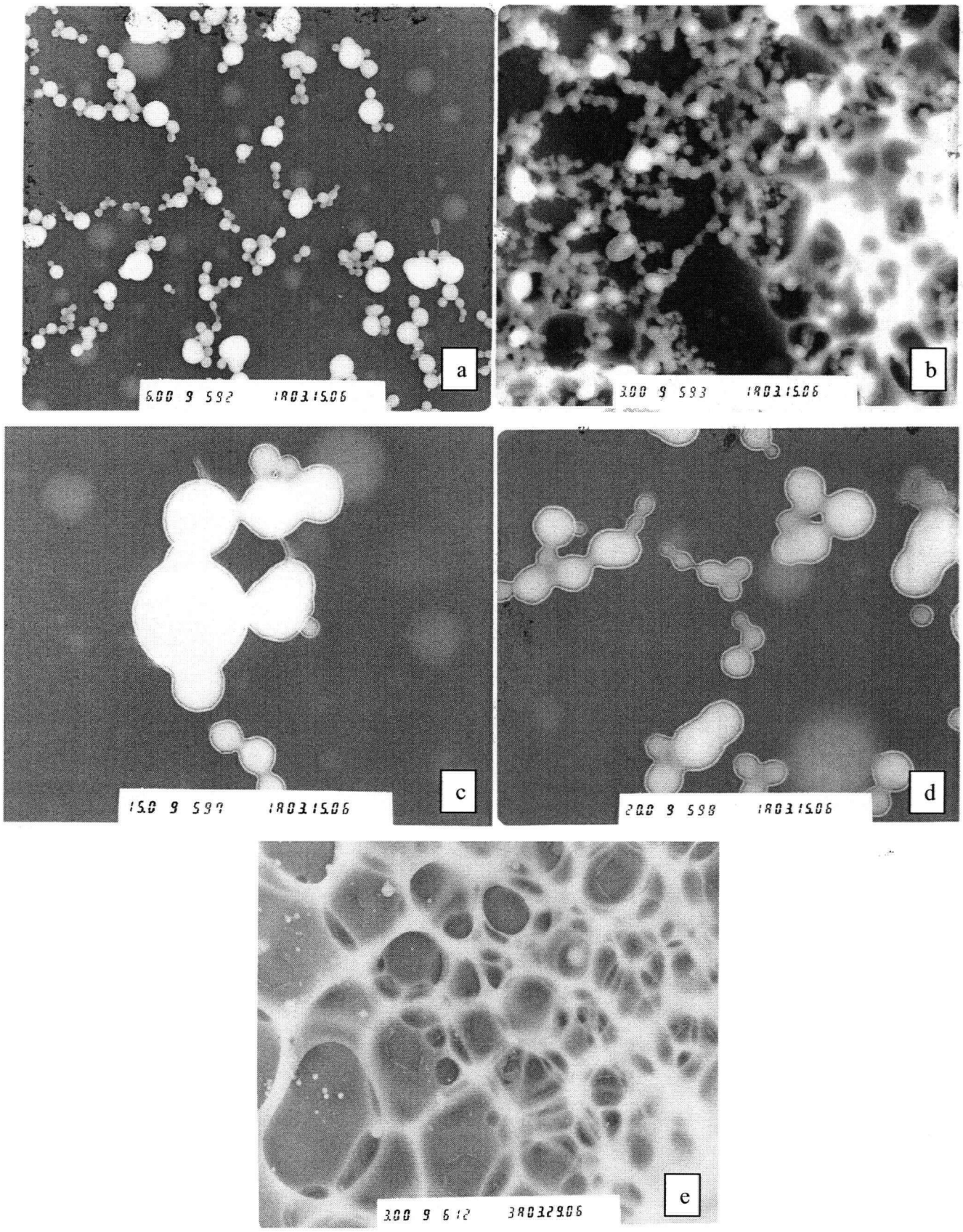

Figure 42: TEM images of spheres (a) x6k (b) x3k (c) x15k (d) x20k (e) x3k magnification

As Figure 42 demonstrates, the spherical particles vary in diameter, approximately between 150 to 650 nm. A select few are as large as 1.4 μm. The particles are not dispersed in any orderly fashion, they do however appear to connect and form chains or clusters: Figure 42(a) and (b). Note that, particularly in Figure 42(b), the spheres appear to blend in with each other forming fibrous structures, with the more transparent materials between the spheres appearing to join them together. It is possible, then, that the spheres not only exist on the surface, but also within the fiber-like material. However, in areas that are more concentrated with spider silk material (see Figure 42(e)), spheres exist in fewer numbers and smaller sizes. These smaller particles could be a result of Fe particles not being able to bind with oxygen more easily, making diffusion within a higher concentrated spider silk region more difficult.

When exposed under TEM, the level of transparency of the film depends on the mass and the density of the material. Using Figure 42(d) as an example, it is clear that the smaller spheres are more transparent than the larger spheres. This occurs because the mass of the spheres are dominating the transparency of the material. Figure 42(d) also shows that the spheres themselves contain light material, such as spider silk. If the sphere consisted of mainly iron or iron oxide, all the spheres will appear with the same level of transparency regardless of their size. With that said, the spheres clearly absorb electron energy better than the rest of the film, which leads us to believe that they have a higher concentration of iron and is a more densely packed than the film-like area of the material.

Since a spot test using X-ray EDS covers a large volume of the material, a mapping using the same instrument was performed under TEM imaging to see whether the spheres contained a higher concentration of iron. The area of interest is shown on top left of Figure 43. The EDS scans the area repeatedly, and every scan will identify any area that contains Fe by putting a yellow dot on the map. This scatter map is shown on the top right of Figure 43. We can see two concentrated areas of Fe in the middle left and bottom right of the map, which overlap with the area of the spheres. Since the concentrated areas are not clearly outlined, we can say that the spheres contain a higher concentration (although not a significant one) of Fe than the rest of the film.

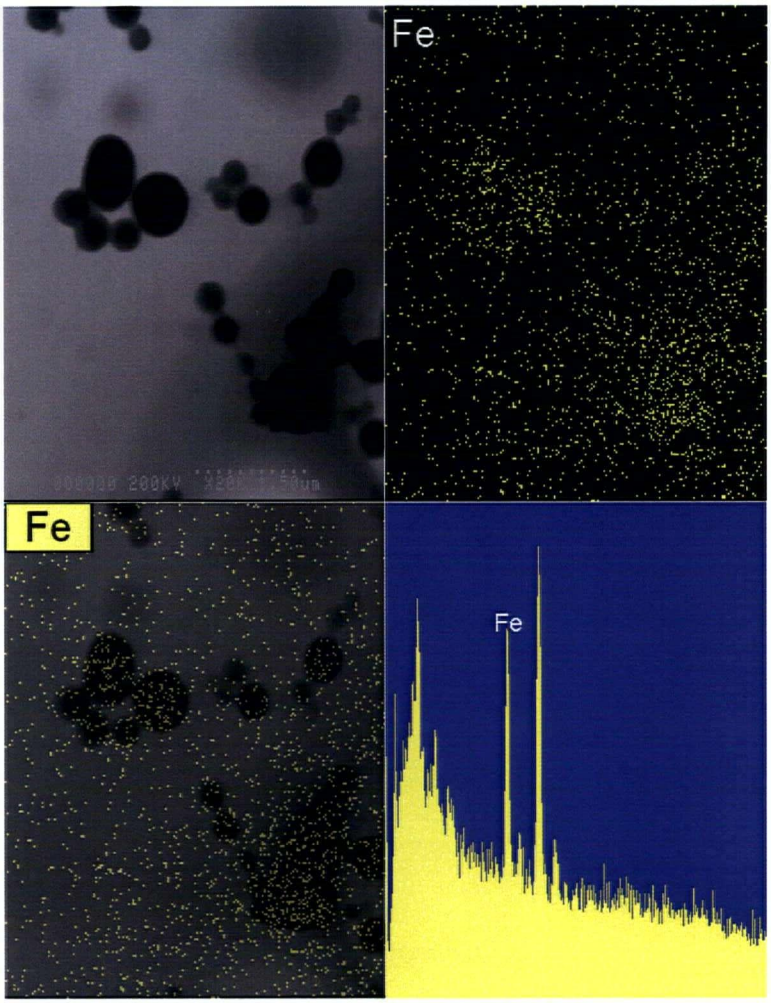

Figure 43: X-ray EDS mapping of a TEM image

5.3.4 Electron Diffraction

To further explore the form in which iron oxide exists within these spheres, an electron diffraction using the TEM was performed.

Review on electron diffraction

Electron diffraction has been used to examine the structure of various materials. This technique originated from the hypothesis that a moving electron should possess wave-like properties [82]. Earlier diffraction techniques used low energy electrons (30-600 eV) which can only penetrate a few atom layers. Current electron diffractions are performed under high energy electrons (10-60kV) [82], and can accordingly penetrate much thicker materials. Transmission electron diffractions performed with in TEM are carried out with thin films that are less than 1 mm thick.

Electron diffraction works because of the scattering of electrons when matter is struck [84]. The electron waves scatter off the matter similar to that of light scattering off of a diffraction grating. The way the incoming beam is diffracted by the material can be observed to examine the crystallography of the material.

Single crystal matter such as diamond will appear in clear spots on the resulting image. Polycrystalline structures are made up of many single crystal grains, and therefore, will appear less ordered on an image than a single crystal structure. Instead, such structures appear as a super position of several different single crystal grains, with the final images generally appearing as rings of spots that are closely grouped. Since such amorphous material is completely disordered, the diffraction patterns appear as blurry rings [82, 85].

Results

In our study, the image generated (Figure 42) shows an amorphous structure within the spheres. This indicates that the iron oxide within the spheres is randomly distributed. Such a finding is consistent with the previous finding of a low concentration in iron, since higher concentration of iron would be more likely to show a crystalline structures.

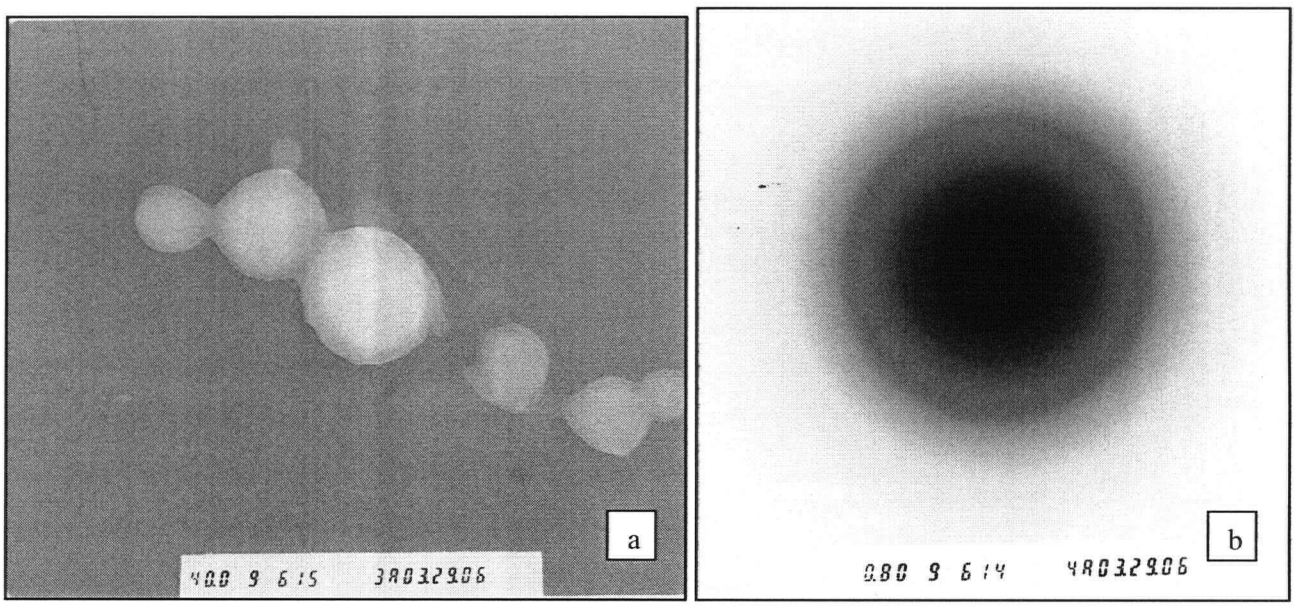

Figure 44: (a) Sphere used for electron diffraction (b) Electron diffraction showing amorphous structure

5.3.5 FTIR

So far, our testing has shown that the formation of the observed spheres is a direct result of mixing iron pentacarbonyl with regenerated spider silk solution. The spheres contain a concentration of Fe that is slightly higher than the rest of the material. Fibrous and porous material containing a low concentration of iron also formed as a result of this mixed solution. In order to further explore the reason behind this phenomenon, an FTIR was performed to study any binding that could have occurred between the iron particles and the spider silk proteins.

An FTIR was performed using the Bomen MB100 120 FTIR spectrophotometer with a 4 cm^{-1} resolution. The iron spider silk solution was deposited onto a potassium bromide plate. The entire area was covered with solutions and then exposed to UV light. However, the film formed by this solution is very porous and thus transmittance intensity would be significantly affected. Therefore, the FTIR steps were repeated until the transmittance was around 50%. Another good indication of a successful spectrum was the disappearance of the noise introduced by carbon dioxide in the lab's atmosphere, amounting to around 2000 (cm^{-1}). The final FTIR spectrum is shown in Figure 45. The top spectrum represents the newest iron spider silk sample and the bottom spectrum was previously obtained from a sample of pure regenerated spider silk.

Peaks below 1450 were not resolved and lacked distinctiveness, thus they are not addressed here. The Amide I and Amide II peaks are shown at wavenumber 1657 and 1537. The vibration mode in the spectral region between 1600-1700 cm^{-1} predominantly originated from the C=O stretching of Amide I group [86]. Based on the position within this spectral region, 1657 cm^{-1} represents a 20% presence of α -helix in the sample's secondary structure [86, 87]. 1537 falls within the Amide II spectral region of 1500 – 1600 cm^{-1}. This region represents N-H bending and C-N stretching of the backbone of Amide II [88]. Spectral 1537 also represent an α -helix secondary structure [87]. These peaks existed in the original pure spider silk FTIR spectrum, therefore their presence here also represents the secondary structure of spider silk in the iron spider silk film. Peak 1242 in the pure spider silk sample has become resolved with the iron spider silk sample. This could be explained by the fact that 1242 represents a random conformation, and was not a high intensity peak in the pure spider silk sample. The resolved peak in the iron spider silk sample therefore does not represent a finding of any new significance.

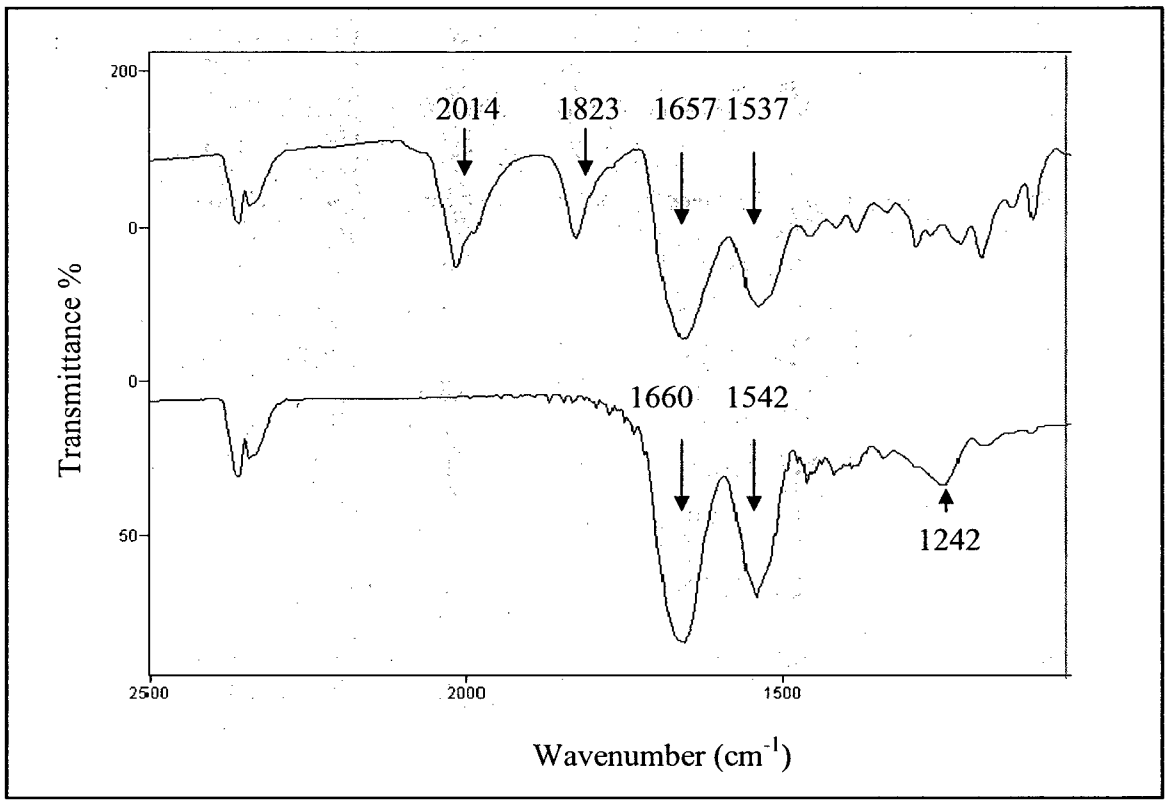

Figure 45: FTIR of iron spider silk sample. Top spectrum is iron spider silk; bottom spectrum is the pure regenerated spider silk.

The spectra peak found at 2014 cm^{-1} represents the presence of Fe-CO vibration assigned for $Fe(CO)_5$. This high intensity peak shows the existence of $Fe(CO)_5$ that was not successfully photolysed. This reaction is illustrated in Figure 46. From a molecular point of view, the Fe-CO bond will be broken by one photon at a time under UV irradiation. This type of photolysis has been shown in previous works [89]. As the photon cleaves one bond, the CO is broken free from what is now an unstable molecule of $Fe(CO)_4^-$ [90]. Two possible reactions of $Fe(CO)_4^-$ could then follow. One is that the CO will evaporate, leaving the unstable $Fe(CO)_4$ molecule to naturally decompose where the Fe and the CO can completely separate. However, due to the matrix of proteins, the CO might not be able to escape fast enough. Therefore, it is also possible that due to close proximity of the CO to the $Fe(CO)_4$, the $Fe(CO)_5$ will be reformed, as it is a more stable state for the molecules. Therefore, due to these reactions, one can expect that a specific level of $Fe(CO)_5$ will always exist within the iron spider silk film.

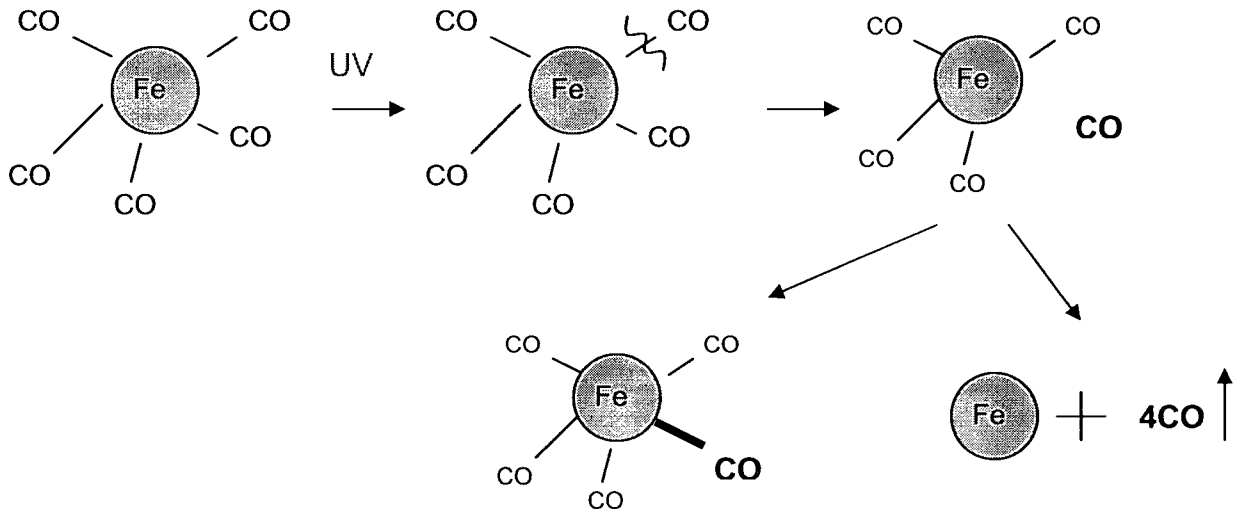

Figure 46: Photolysis of $Fe(CO)_5$ under two possible reactions

Peak 1823 lies in the region which is normally associated with bridging CO groups. [89] It suggests the presence of multiple CO bands in an unresolved envelope. The value of 1823 is very close to that of 1828, which has previously been reported for another compound, triiron dodecacarbonyl ($Fe_3(CO)_{12}$) [89]. This peak could possibly show the existence of two types of Fe bindings taking place.

First of all, if several $Fe(CO)_4^-$ molecules were formed within close proximity to each other, it is possible that they will share CO ligands with their respective neighbours to form $Fe_3(CO)_{12}$. This is shown in Figure 47(a). This could be an additional reason why a high concentration of carbon is found within the particles produced by pure $Fe(CO)_5$. [Reference to table 9]

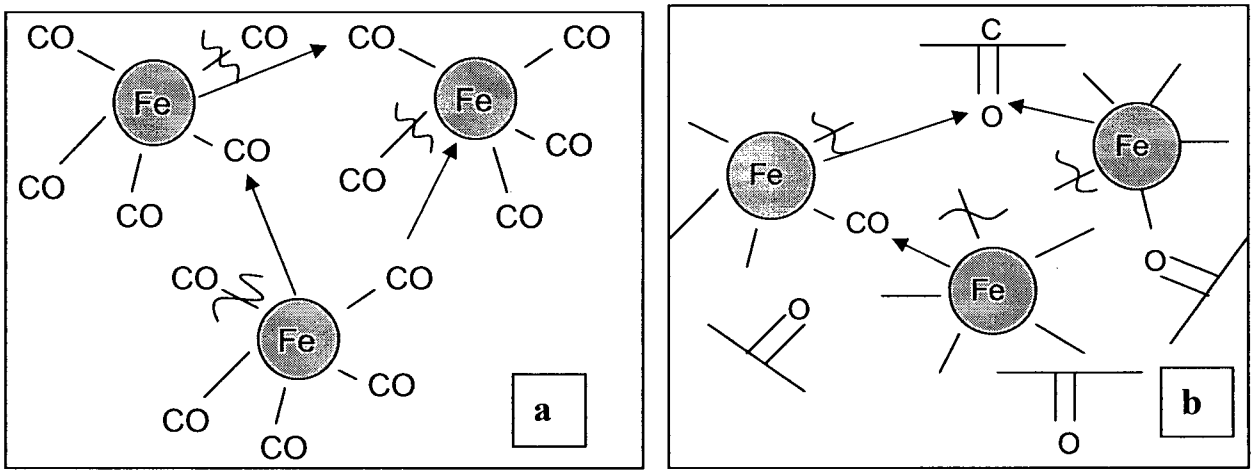

Figure 47: Two reactions for the formation of $Fe_3(CO)_{12}$ (a) Fe-CO binding through neighboring molecules (b) Fe-CO binding with neighboring amino acids

Second, C=O side groups are also found in the major spider silk amino acids such alanine and glycine [99]. Their chemical composition is shown in Figure 48 [100].

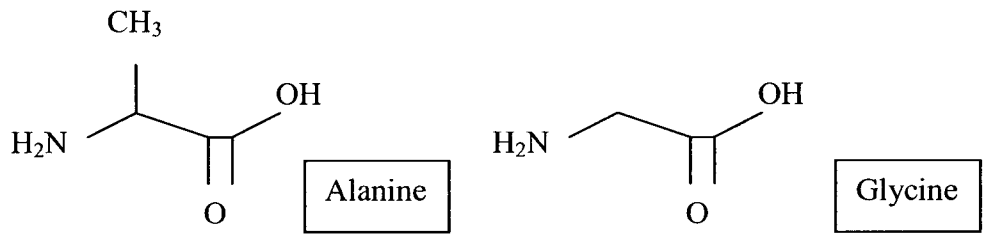

Figure 48: Structure of dominant amino acids found within spider silk

The existence of C=O side groups could provide an explanation as to why some area observed formation of iron spider silk spheres. As the spider silk dissolves in HFIP, the hydrogen bonds between the amino acids break, thus allowing the spider silk to dissolve into a solution. It is likely that $Fe(CO)_4^-$ can bind to the C=O group within the amino acids, and form $Fe_3(CO)_{12}$ with other $Fe(CO)_4^-$ molecules, as well as with amino acids. This is illustrated in Figure 47(b).

To further support the hypothesis related to peak 2014 and 1823, iron spider silk sample was tested using FTIR method. Here, spectrums were taken at different times after deposition of iron spider silk solution. Again, potassium bromide plate was used as the substrate. The results are shown in figure 49.

The peak of 2014 decreased in transmittance very quickly during the first 5 minutes of UV exposure. This shows the breaking of Fe-CO bonds within the $Fe(CO)_5$. Evaporation of $Fe(CO)_5$ could also have contributed to this decrease. Once passed the initial 5 minutes, the reaction appeared to have reached a plateau. This results confirms with the hypothesis (illustrated in figure 46) that a certain level of $Fe(CO)_5$ will always remain in the sample.

In contrast, the peak of 1823 increased in transmittance during the first 5 minutes of UV exposure. This increase supports the hypothesis (illustrated in figure 47) that formation of $Fe_3(CO)_{12}$ is likely to have occurred. After 5 minutes, the reaction appeared to also have reached a plateau. These three FTIR spectrum shows that the initial minutes of the UV exposure is a

crucial state. Once that is passed, reaction significantly slows down. This is shown by the overlapping of 5 minute spectrum with the 40 minute spectrum.

Finally, a small shift in wavenumber at the 1823 peak is shown between 1 minute and 5 minutes spectrum. Since wavenumber shifts when the sample is in different states, such as liquid, solid or gas, it is likely that the shift here is a result of the sample not being completely dried when the spectrum was taken after 1 minute of UV exposure.

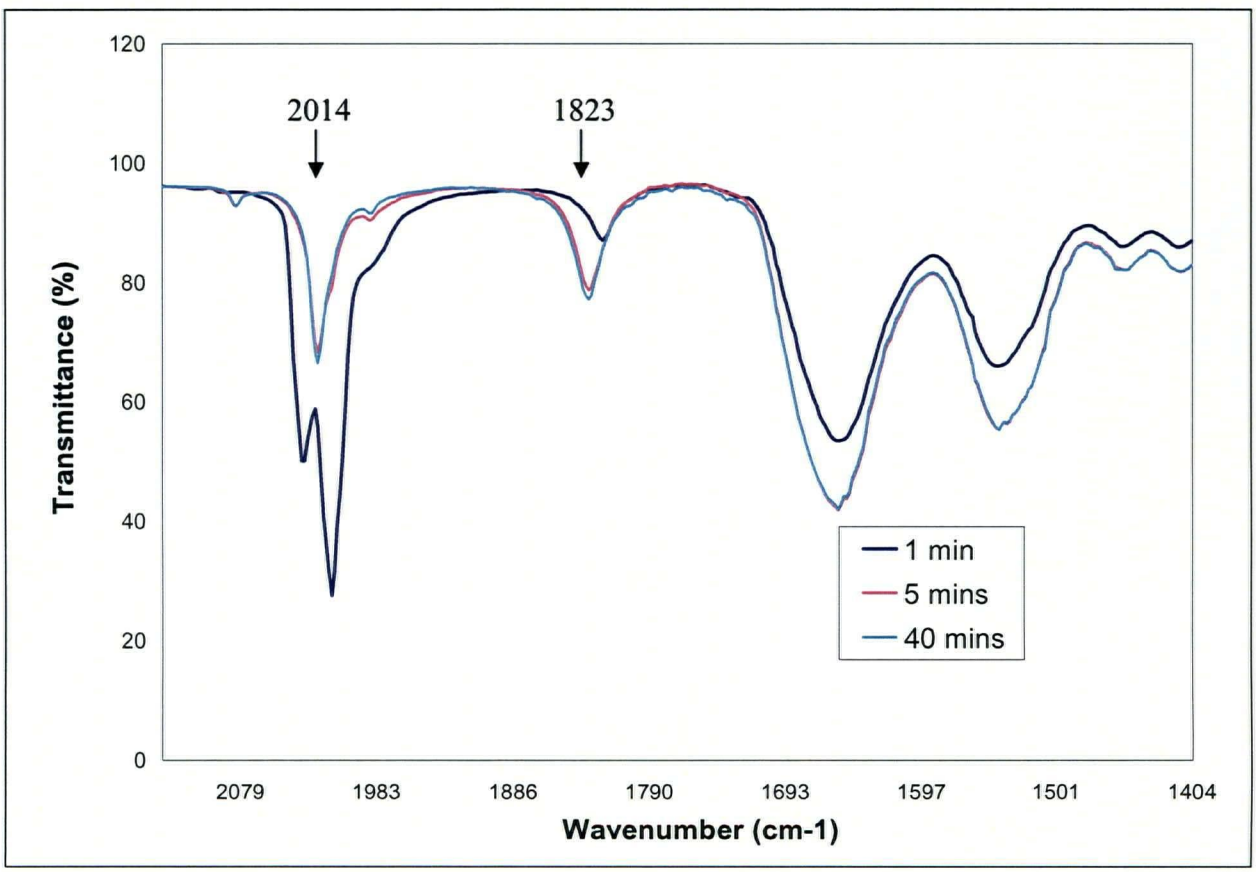

Figure 49: FTIR spectrums of iron spider silk sample after different exposure time

5.3.6 SQUID data

The purpose of this study was to embed iron oxide into a spider silk matrix. It is expected that this will result in a material that can be used under an external magnetic field. A SQUID was thus used to characterize the magnetic hysteresis of the material.

Samples with two different volume dilutions were used. The first sample uses a 1:1 v/v dilution between the $Fe(CO)_5$ and the 1% w/w spider silk solution. The second uses a 2:1 v/v dilution. Figures 50 and 51 illustrate the M vs H hysteresis plot for the respective samples.

The data from the SQUID shows that the magnetization of magnetic moments obtained from the 1:1 v/v sample is 10 times larger than that of the 2:1 v/v sample. This magnetization is, however, 10^3 times smaller than what is found in the Ni spider silk sample introduced in chapter 4. This is not surprising, as the magnetic material (Ni) content in that sample was around 14%, where as the Fe in this sample is only around 1.5 – 3 %.

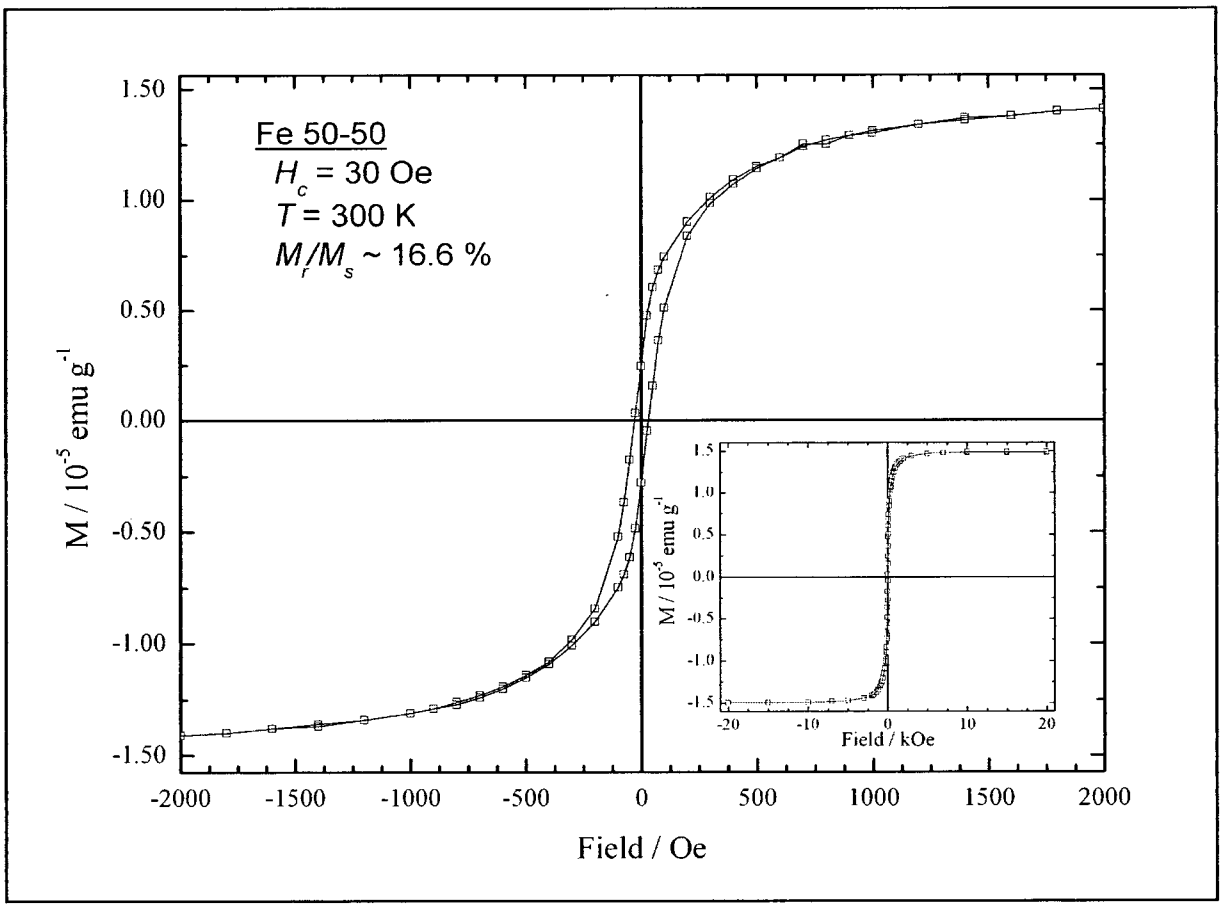

Figure 50: Hysteresis curve for 1:1 v/v iron spider silk sample

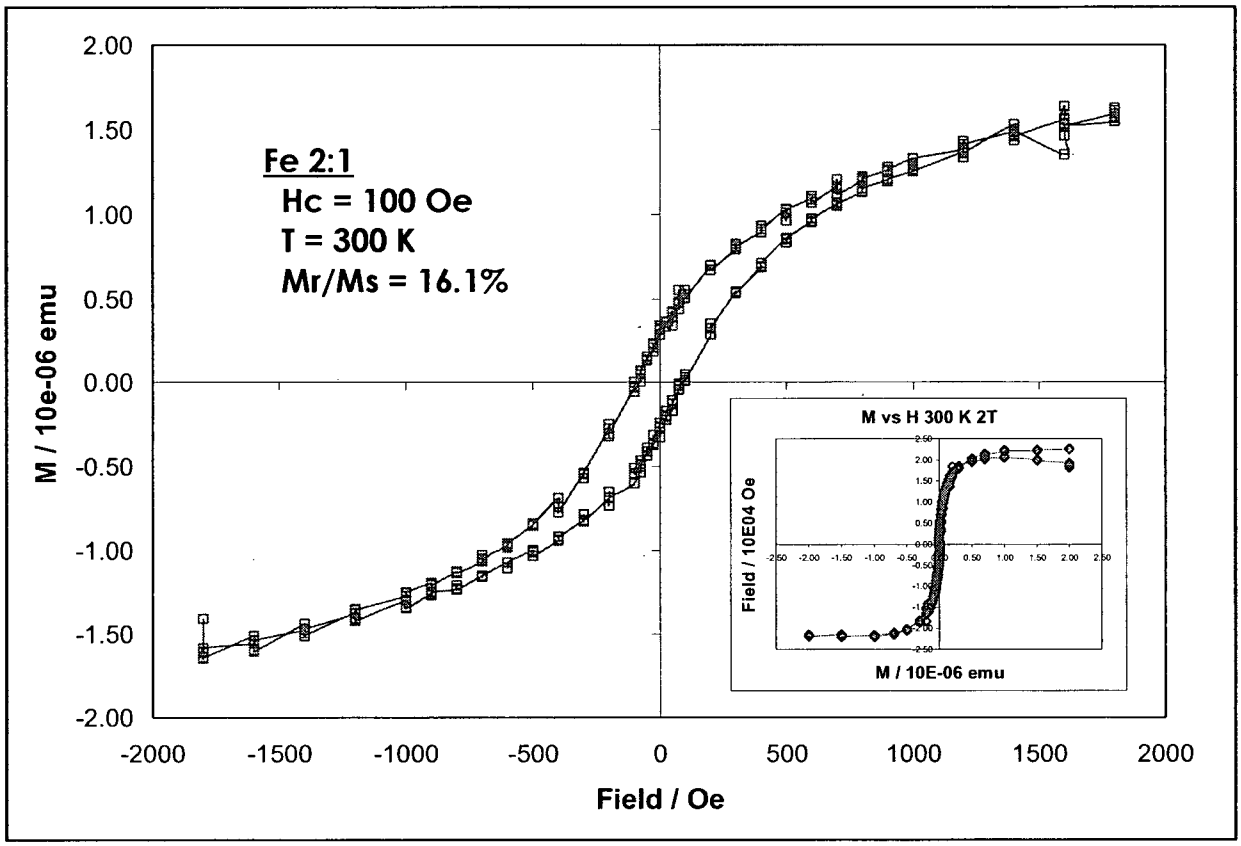

Figure 51: Hysteresis curve for 2:1 iron spider silk sample

5.4 Fe spider silk thin film (diluted spider silk solution – 0.25% w/w)

Our results allow us to come to several conclusions about spider silk. The concentration of Fe in the iron spider silk material obtained by using the current method is low, resulting in low magnetization of the material. It has previously been shown that the spheres have a higher concentration of Fe then the rest of the film. In addition, in areas where there appears to be high concentration of spider silk material, the formation of spheres is more inhibited.

Overall, this leads to the hypothesis that a lower concentration of spider silk solution should form more densely packed particles with a higher concentration of Fe. This is premised on the idea that when there is a higher concentration of spider silk in the film, the amino acids prefer to bind with themselves to form spider silk film. However, with less concentrated spider silk solution, the amino acids are more likely to bind with iron to form spheres, because smaller amounts of spider silk amino acids are available to form films.

5.4.1 Experimental method

Iron pentacarbonyl purchased from Sigma Aldrich was diluted in 1:1 v/v with 0.25%w/w spider silk solution (spider silk solution vs. $FeCO_5$). Once the two solutions were mixed, the mixture was deposited onto a silicon substrate to form a thin film. This film was then exposed under an Entela model UVG-54 handheld short wave UV lamp for 2-3 hours. Within 10 minutes of exposure to UV, the material began quickly producing cloudy smoke, demonstrating that a significant amount of material had evaporated.

5.4.2 SEM images

Figure 52 shows the material that remains on the silicon substrate. At low magnification, Figure 52(a) shows the overall look of the film that had remained on the substrate. The material mimics the look of a coffee stain, with the edges containing a higher concentration of material (and hence more spider silk material to form films). The center appears scattered with circular or cluster-like materials (Figure 52(b)). At higher magnification, Figure 52(c) shows these more circular examples. The sample cluster in Figure 52(c) appears to have a higher concentration of the brighter material on its outer rim. As pointed out on the figure, this particular samples shows spherical materials on the outer rim.

Figure 52(d) shows the second group of material. These clusters appear darker, and are generally several times larger than the circular materials described above. Spheres are much more apparent in these clusters, appearing in various sizes and locations within the cluster (as opposed to just on the outer rim). The rest of the cluster material appears to be spider silk film, similar to the area shown in Figure 52(a). Looking more closely at the areas of the substrate between the circular or the cluster like material, we can see many small particles. These are likely to be iron oxide particles. They are formed by iron atoms, perhaps in vapour form, that bind with oxygen in the air and deposit back on to the substrate.

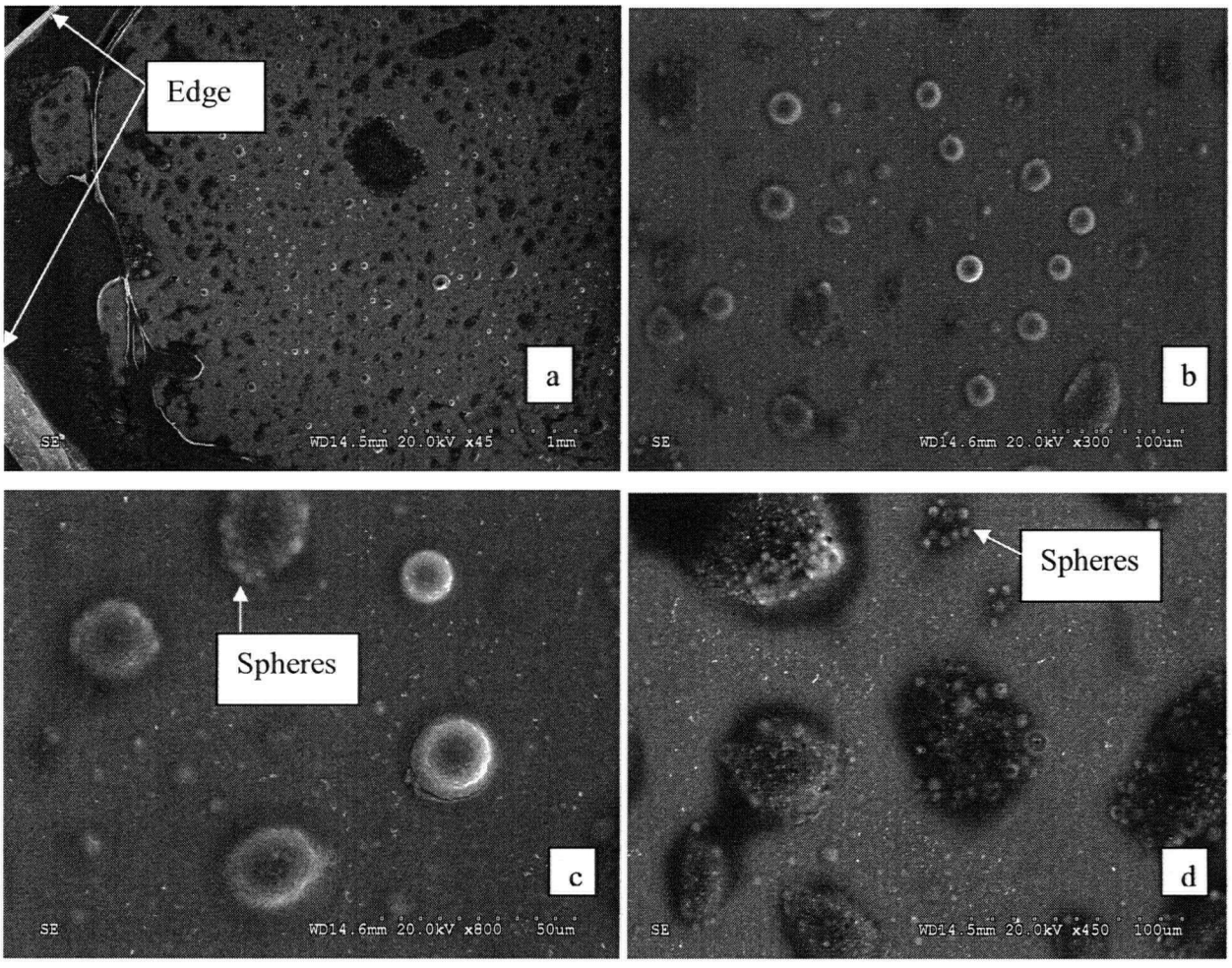

Figure 52: SEM of 0.25% spider silk solution mixed at 1:1 v/v with $Fe(CO)_5$ (a) x45k overall look of the film, edge with thin film is shown (b) islands formed on the substrate (c) circular shaped areas (d) cluster areas

5.4.3 X-ray EDS

X-ray EDS were performed on both of the clusters, as well as on the circular samples. The concentration of the main elements is tabulated in table 10.

Table 10: X-ray EDS element concentration of cluster and circular samples

	Cluster (wt%)	Circular (wt%)
Carbon	44.75	49.28
Nitrogen	13.14	17.02
Oxygen	27.68	26.43
Fluorine	0.00	0.67
Iron	**14.43**	**6.61**

Note that the iron concentration in the cluster sample is twice the amount found in the circular sample. This could correlate to the larger number of spheres in cluster material. However, in

general, the amount iron concentration found in this iron-spider silk mixture is significantly larger than ones found using 1% w/w spider silk solutions. When an X-ray EDS was performed on the film area (edge area in Figure 52(a)) alone, around 11% concentration of iron was also found. This concentration is lower than what was found previously for pure iron oxide particles (36%). Therefore, they are not pure iron oxide, but, instead, iron spider silk spheres. Overall, this experiment confirms the previous hypothesis that iron was more likely to attach to spider silk material when the spider silk concentration is lower. In addition, with a lower spider silk concentration, iron is more likely to bind with oxygen and form larger and more densely packed spheres with the spider silk proteins.

5.5 Fe spider silk thin film (higher concentration of spider silk solution 2%)

With the understanding of the iron spider silk mixture gained from this study, we now know that with a reduction in concentration, spider silk is more likely to bind with iron or an iron compound to form spheres and thin films. The final material achieved here contained approximately 6-12% of iron. On the other hand, if the formation of film is required, the concentration of the spider silk solution should be increased. Such an increase in concentration may, however, reduce the iron concentration in the new material.

5.5.1 Experimental method

Iron pentacarbonyl were diluted in 1:1 v/v with 2% spider silk solution (spider silk solution vs. $FeCO_5$). The experimental steps for formation of the film are outline in 5.4.1. In this case, no visible smoke was observed.

5.5.2 SEM images

SEM images are shown in figure 53. As the concentration of spider silk increased, a significant increase in film formation was obtained. Figure 53(a) illustrates ¼ of the film surface, where near the center of the film (top of the image) empty voids can be found. Again, a higher concentration is found along the edges of the film.

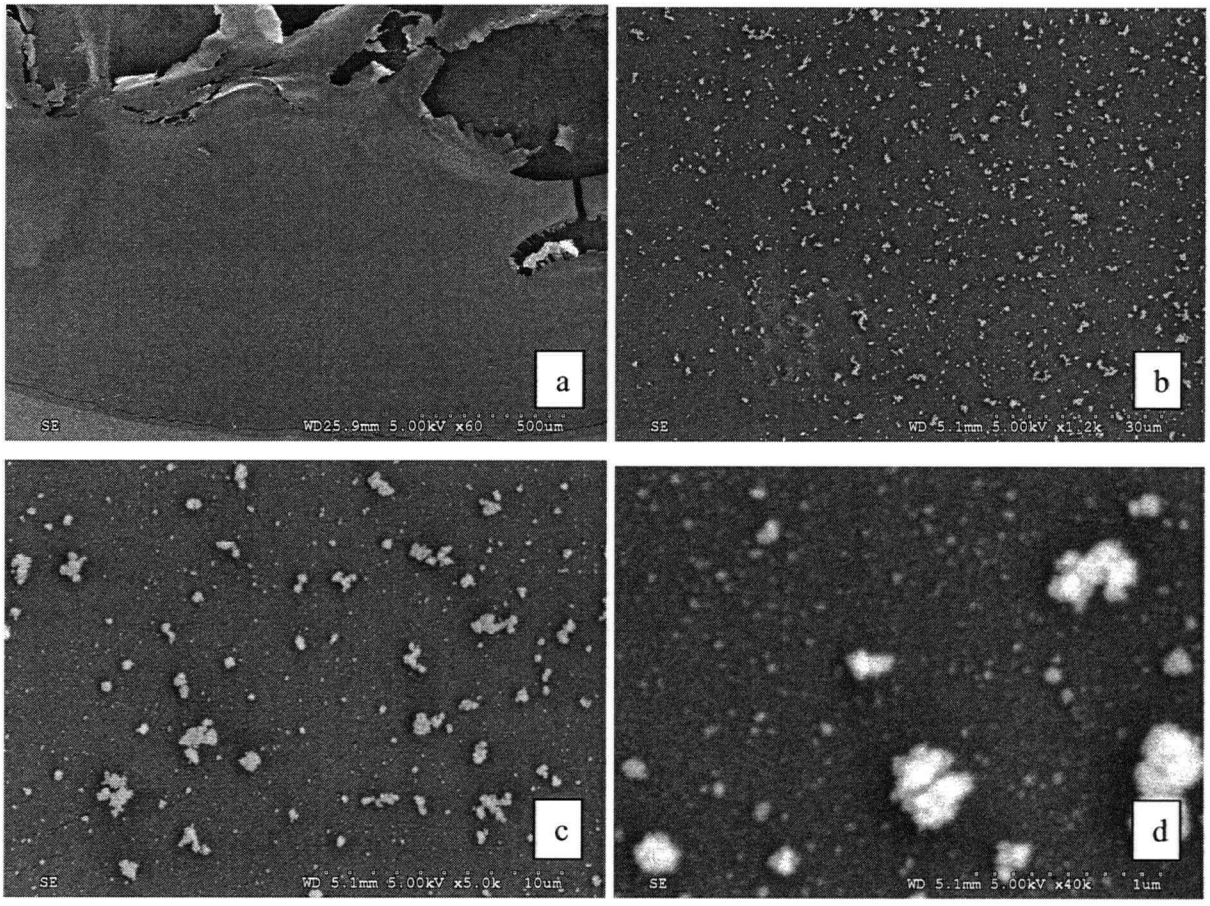

Figure 53: SEM images of spider silk film material obtained from 2% w/w spider silk solution (a) Film edge with solid film formation (b) x1.2k (c) x5k (d) x40k

When taking a closer look at the film, particles are found scattered on the surface. This can be seen in Figure 53(b) and (c). Figure 53(d) shows an image with 40k magnification. It shows small single particles ranging in diameter between of 30-100 nm. Many of these particles also bound together to form larger clusters in the range of 200-600 nm in length. These particles are similar to what was observed on the sample obtained from exposing $Fe(CO)_5$ under UV. Figure 52(d) shows some of these particles. It can be hypothesized that these particles are formed through vapour deposition. In this case, because 2% w/w spider silk solution represented a much higher concentration, it was more difficult to form a uniform mixture with $Fe(CO)_5$. Therefore, unmixed $Fe(CO)_5$ became available for forming pure iron oxide particles on top of the film surface. These particles were also found on the bare substrate area, where no iron spider silk solution was originally deposited (Figure 54). This further confirms that vapour deposition had taken place.

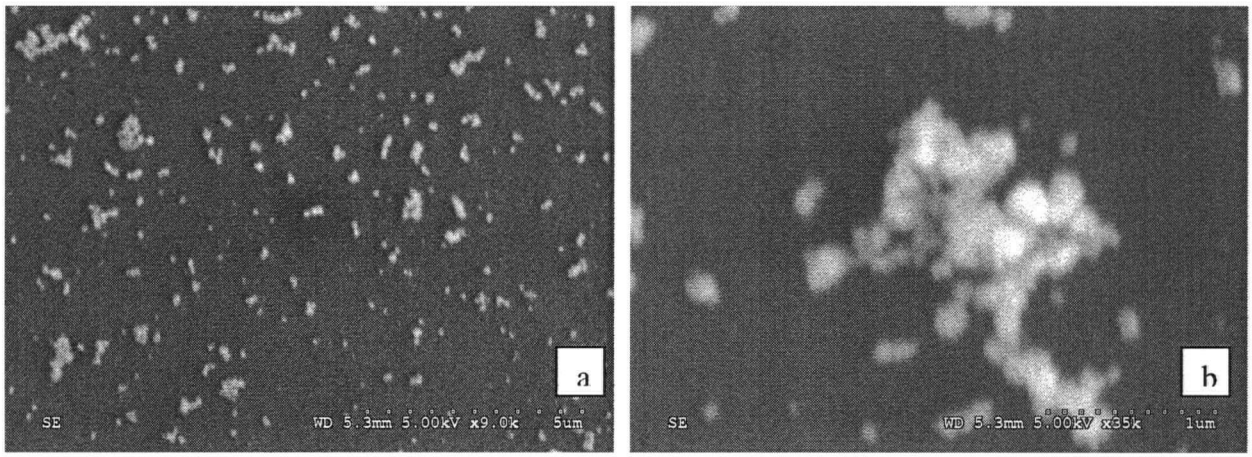

Figure 54: Particles found on bare silicon substrate outside of the film area (a) x9K (b) x35k magnification

To further examine the film, cross sectional images were taken to see whether any particles had formed within the film. This is shown in figure 55.

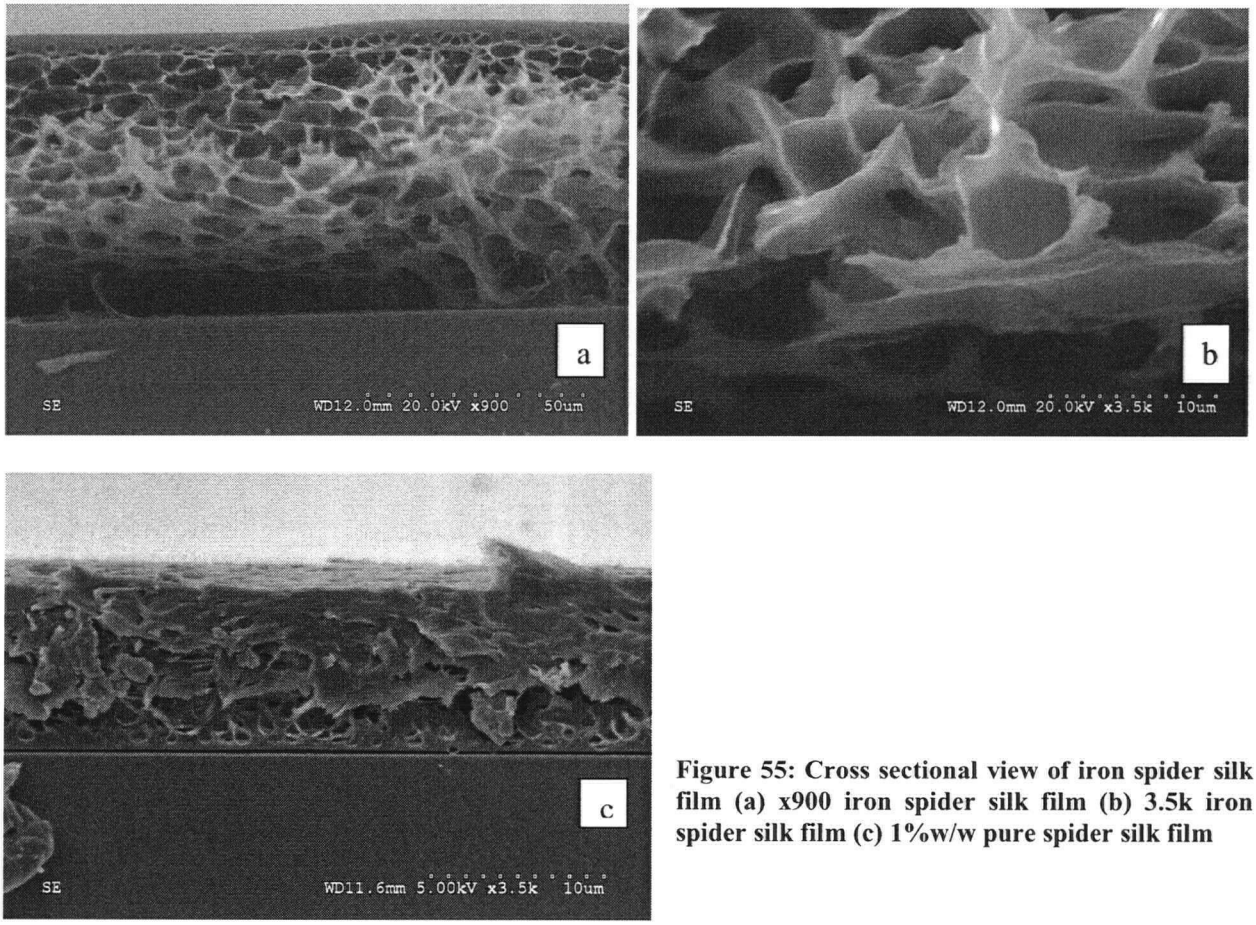

Figure 55: Cross sectional view of iron spider silk film (a) x900 iron spider silk film (b) 3.5k iron spider silk film (c) 1%w/w pure spider silk film

5.5.3 X-ray EDS

Film

An X-ray EDS was first performed on the film (see Table 11). This was performed on two different locations of the film. The iron concentration was found to be between 5.3 and 7.8 wt% in both locations. This is a reasonable finding, as some areas might have slightly more particles then others, and the volume in which the spectrum is obtained can also vary slightly.

Table 11: Two EDS tests performed on the surface of the iron spider silk film

	Concentration Test 1 (wt%)	**Concentration Test 2 (wt%)**
Carbon	37.09	47.93
Nitrogen	17.44	12.97
Oxygen	26.78	23.36
Fluorine	13.37	7.97
Iron	**5.33**	**7.76**

On silicon substrate

The particles found on the silicon substrate were examined by EDS. Table 12 shows a very high concentration of iron within the material. Table 9 had a concentration of Iron and oxygen in the 36% range and had a ratio of 1:1; in this case, iron and oxygen concentration is only around 26%. However, we can see that the amount of oxygen to iron concentration is again 1:1, this could indicate that similar type of bonding has occurred here. The existence of nitrogen possibly indicates that a small amount of spider silk is contained within the particle. While the particles also exhibit a high concentration of iron, due to finding a reasonable amount of Nitrogen, we must conclude that some or maybe all of the iron has bonded with small amount of spider silk protein. The amount of protein in this sample is significantly smaller than previous. We must also consider the fact that nitrogen and carbon are found in many organic materials, in which the substrate could have been previously contaminated by as well.

Table 12: EDS spectrum main elements found using particles formed on the silicon substrate

	Concentration (wt%)
Carbon	36.80
Nitrogen	10.99
Oxygen	25.99
Iron	**26.22**

Cross section

Using cross sectional view of the film, EDS can be performed perpendicular to the film, thus give data at different depts. The iron concentration within the film was higher in the upper layer of the film than the lower layers. This is not surprising, as the particles on the surface contribute to the concentration increase. Table 13 tabulates the wt% of main elements found in the EDS spectrum.

Table 13: EDS spectrum main elements found in the upper and lower layer of the iron spider silk film

	Upper layer (wt%)	Lower layer test 1 (wt%)	Lower layer test 2 (wt%)
Carbon	40.52	52.35	47.43
Nitrogen	17.33	26.97	31.54
Oxygen	18.89	16.21	16.55
Fluorine	18.36	2.40	3.14
Iron	**4.90**	**2.08**	**1.33**

The Fluorine concentration on the upper layer is higher than on the lower layer. Since the amino acids of spider silk do not contain fluorine, it is likely the result of some remaining unevaporated HFIP. As the HFIP escapes from the lower layer of the film, voids are formed within the material. Since the HFIP must eventually escape through outer layer, more fluorine is likely to be trapped here. This is exacerbated since, from the cross sectional images, we can see that the upper layer is less porous then the inner layers; not surprising since the surface tension of the spider silk droplet can cause the outer layer of the film to be slightly more concentrated then the inner layers. The thicker outer layer is more difficult to diffuse through, thus it creates a bottle neck for the evaporation of HFIP. This provides the opportunity for the fluorine to be trapped within the outer layer.

5.6 Summary

This chapter has demonstrated a new property of spider silk when mixed with Iron Pentacarbonyl. A simple, ambient conditioned lab fabrication process is outlined to produce iron spider silk material in different forms and iron concentrations.

The higher the concentration of spider silk, the more likely a film will form when the mixture is deposited on a silicon substrate. However, with a higher concentration in spider silk, the film's iron content decreases due to the spider silk amino acids being closer to each other in solution and thus preferring to bind with each other rather than iron. Even though the film contained small amounts of iron, particles with high iron concentration are found on the film surface, as well as on the bare substrate. It is suspected that the vapour condition in this case was able to form particles on top of the entire sample.

When the concentration of spider silk solution was reduced to 1% w/w, two phases were formed on the material. The film form was very thin, and was generally found closer to the outer edges of the film. A fibrous area was also formed where nano size iron spider silk particles with slightly higher iron concentrations could be found.

As the concentration of spider silk was reduced to 0.25% w/w, the final iron spider silk material showed islands of material in either circular, or cluster-like manner. The SEM images showed sub-surface material exhibiting spherical contours. The concentration of iron found within these islands was significantly higher than what was found in the other two iron spider silk solutions. This reconfirms the hypothesis that iron is more likely to bind with spider silk under slightly more diluted conditions. However, with visible smoke seen during the experiment, it is clear that a large amount of the material also evaporated during this experiment.

We believe this use of spider silk protein in fabricating iron spider silk material has enabled the process to be performed under less rigorous conditions. Most previous work has been performed under low temperature in high vacuum or pressure chambers. This work has opened up new applications for spider silk as a magnetic material and, at the same time, identified new behaviours that are exhibited by this incredible material that can perhaps be utilized in biomedical applications.

CHAPTER 6

Conclusion and Recommendation

The objective of this research was to study the manipulation of spider silk with MEMS applications in mind. The new understanding of spider silk brought about by this study will contribute significantly to not only the field of MEMS, but, it may also lead to new ideas for uses of spider silk as a biomaterial in general.

In this work, spider silk was manipulated in three ways, leading to the discovery of several properties of spider silk.

The first study was focused on spin coating a regenerated spider silk solution to form a film on silicon substrate. Once this was successful, nano indentation was performed to obtain mechanical properties such as elastic modulus, hardness and viscoelasticity. Such data is shown for the first time in this study.

Next, a new microfabrication technique was developed to produce a microbridge structure out of spider silk film. This microbridge was subsequently used in a fracture test to obtain a stress and strain curve. These data offer the first mechanical characterization of regenerated spider silk in a film form. The spider silk film was found to have fracture strength that is 2-10 times larger than conventional biopolymers used in MEMS. Aside from the importance of learning these mechanical properties, the new microfabrication technique offers a way to form simple microstructures from regenerated spider silk solutions that can be used in various MEMS applications, such as the creation of cantilever beams or membranes.

The purpose of the second set of experiments was to widen the applications of spider silk film. To this end, Ni micron particles and regenerated spider silk solution were successfully combined

to form a microbridge and a cantilever beam. A fracture test was performed on the microbridge to obtain its mechanical properties. As well, its ferromagnetic properties were mapped using a SQUID machine. A bending test was also performed by placing a moving permanent magnet next to the beam to measure the relationship between the external magnetic field and the beam bending. This inexpensive microstructure showcases a proof-of-concept design where magnetically actuated microsensors or drug delivery membranes could eventually be fabricated from spider silk.

The third major work spun off the concept of magnetic spider silk beams fabricated from a spider silk composite. In this case, instead of Ni particles, iron pentacarbonyl was used. A new property of spider silk was found as spider silk proteins formed nano size spheres after mixing with the iron pentacarbonyl. These spheres contained a low concentration of iron. It was found that the iron concentration could be increased significantly if the concentration of the regenerated spider silk solution was decreased. Conversely, if the concentration of regenerated spider silk solution increased, a thick film formed with low concentration of iron, and the nano spheres disappeared. This material property of spider silk bonding to iron is a new discovery that can put spider silk onto a new list of biomedical applications. Some of the potential uses could be in iron tagged imaging materials, or magnetically actuated microstructures.

In conclusion, this work has introduced spider silk as a new type of biomaterial in MEMS applications. Fabrication techniques and material characterization are clearly shown in this report. However, one must keep in mind that this is a preliminary study, and improvements in many areas are still needed. For example, the fracture testing method could be improved by using a testing tool that is similar to that of an Instrum machine. As well, difficulty was experienced in this study in controlling the size of the microbridge, which introduced error in final fracture stress calculations. Since some of the size control issues are related to water causing shrinkage in the film, perhaps a new sacrificial layer can be found to avoid using water as an etchant. Future work in this area could be focused on making smooth and controlled film, and eventually casting, molding or etching the film to make a variety of microstructures.

Furthermore, the Ni spider silk should be tested to see whether a reduction in Ni dilution can increase the elasticity of the material. Tests could also be performed on various dilutions of Ni to

observe how bending properties and material properties change. Also, since Ni is one of several ferromagnetic metals, other powder from different metals that are smaller in size should be used to find an optimal mixture that retains spider silk's mechanical properties while remaining susceptible to external magnetic fields.

Finally, for iron spider silk film and spheres, further investigation of the origin of nano size spheres is required. Relying on the preliminary FTIR data attained in this study, a hypothesis was proposed in chapter 5. However, additional FTIR data must also be obtained to map the peaks and intensity of iron spider silk film from the time immediately after mixing until the final dry film state. The condition in which the experiments were conducted can also be altered. Many previous works have obtained iron spheres coated with polymers in high pressure chambers. Perhaps using a similar method, a new type of iron spider silk film can be developed.

Overall, this project has shed some light on understanding spider silk as a film. At the same time, through out the process, many new properties and applications are introduced. This will open a new field of study in incorporating spider silk with MEMS devices.

Bibliography

[1] S. F. Y. Li, A. J. McGhie and S. L. Tang, "Comparative study of the internal structures of kevlar and spider silk by atomic force microscopy," in *40th National Symposium of the American Vacuum Society, 15-19 Nov. 1993,* 1994, pp. 1891-4.

[2] J. Scheller, K. -. Guhrs, F. Grosse and U. Conrad, "Production of spider silk proteins in tobacco and potato," *Nat. Biotechnol.,* vol. 19, pp. 573-577, 2001.

[3] A. Lazaris, S. Arcidiacono, Y. Huang, J. Zhou, F. Duguay, N. Chretien, E. A. Welsh, J. W. Soares and C. N. Karatzas, "Spider silk fibers spun from soluble recombinant silk produced in mammalian cells," *Science,* vol. 295, pp. 472-476, 2002.

[4] P. Gould, "Exploiting spiders silk," *Materials Today,* vol. 5, pp. 42-47, 2002.

[5] L. OSBORNE. (2002, June 16). Got milk. *NYT (News)* Available: http://query.nytimes.com/search

[6] A. Seidel, O. Liivak and L. W. Jelinski, "Artificial spinning of spider silk," *Macromolecules,* vol. 31, pp. 6733-6736, 1998.

[7] R. LEWIS , "SPIDER SILK - THE UNRAVELING OF A MYSTERY," *Accounts of Chemical Research,* vol. 25, pp. 392, 1992.

[8] G. Altman , "Silk-based biomaterials," *Biomaterials,* vol. 24, pp. 401, 2003.

[9] J. Stephens , "Effects of electrospinning and solution casting protocols on the secondary structure of a genetically engineered dragline spider silk analogue investigated via fourier transform Raman spectroscopy," *Biomacromolecules,* vol. 6, pp. 1405, 2005.

[10] UBC, "Chemistry 527 Course Notes," 2004.

[11] M. Elices , "Finding inspiration in Argiope trifasciata spider silk fibers," *JOM,* vol. 57, pp. 60, 2005.

[12] Blackledge, "Polarized light microscopy, variability in spider silk diameters, and the mechanical characterization of spider silk," *Invertebrate Biology,* vol. 124, pp. 165, 2005.

[13] J. M. Gosline, M. W. Denny and M. E. DeMont, "Spider silk as rubber," *Nature,* vol. 309, pp. 551-2, 06/07. 1984.

[14] S. Kubik , "High-performance fibers from spider silk," *Angewandte Chemie,* vol. 41, pp. 2721, 2002.

[15] F. Vollrath, P. Barth, A. Basedow, W. Engstrom and H. List, "Local tolerance to spider silks and protein polymers in vivo," *In Vivo,* vol. 16, pp. 229-234, Jul-Aug. 2002.

[16] N. Kojic , "Solvent removal during synthetic and Nephila fiber spinning" *Biomacromolecules,* vol. 5, pp. 1698, 2004.

[17] Y. Zhang , "Amino acid composition-dependent elasticity of spider silk," *International Journal of Modern Physics. B, Condensed Matter Physics, Statistical Physics, Applied Physics,* vol. 18, pp. 2516, 2004.

[18] G. Guinea , "Stretching of supercontracted fibers: a link between spinning and the variability of spider silk," *The Journal of Experimental Biology,* vol. 208, pp. 25, 2005.

[19] D. L. Kaplan, "Spiderless spider webs," *Nat. Biotechnol.,* vol. 20, pp. 239-240, Mar. 2002.

[20] Z. Shao and F. Vollrath, "Effect of solvents on the contraction and mechanical properties of spider silk," *Polymer,* vol. 40, pp. 1799-1806, 1999.

[21] R. W. Work, "A Comparative Study of Supercontraction of Majoy Ampullate Silk Fibers of Orb-Web-Building Spiders (Araneane)," *J. Arachnol,* pp. 299-308, 1981.

[22] Y. Liu, Z. Shao and F. Vollrath, "Relationships between supercontraction and mechanical properties of spider silk," *Nat. Mater.,* vol. 4, pp. 901-905, Dec. 2005.

[23] G. Guinea , "Self-tightening of spider silk fibers induced by moisture," *Polymer,* vol. 44, pp. 5785, 2003.

[24] J. Perez-Rigueiro, M. Elices and G. V. Guinea, "Controlled supercontraction tailors the tensile behaviour of spider silk," *Polymer,* vol. 44, pp. 3733-3736, 2003.

[25] K. N. Savage, P. A. Guerette and J. M. Gosline, "Supercontraction stress in spider webs," *Biomacromolecules,* vol. 5, pp. 675-679, 2004.

[26] Y. Yang , "Toughness of spider silk at high and low temperatures," *Advanced Materials,* vol. 17, pp. 84, 2005.

[27] S. Osaki , "Ultraviolet rays mechanically strengthen spider's silks," *Polymer Journal,* vol. 36, pp. 657, 2004.

[28] R.W. Work and P.D. Emerson. (1982), An apparatus and technique for the forcible silking of spiders. *J. Arachnol (10),* pp. 1-10.

[29] Z. Shao , "Structure and behavior of regenerated spider silk," *Macromolecules,* vol. 36, pp. 1157, 2003.

[30] D. H. Hijirida, Kinh Gian Do, C. Michal, Shan Wong, D. Zax and L. W. Jelinski, "^{13}C NMR of Nephila clavipes major ampullate silk gland," *Biophys. J.,* vol. 71, pp. 3442-7, 12/. 1996.

[31] Nelson L. Alpert, William E. Keiser, Herman A. Szymanski, *IR Theory and Practice of Infrared Spectroscopy.* ,2nd ed.New York : Plenum Press, 1970, pp. 380.

[32] NorthWestern University, Keck Interdisciplinary Surface Science Center. What is FT-IR? *2006(April),* pp. 1. Available: http://www.nuance.northwestern.edu/KeckII

[33] Cornell University, Baker Group. Nanoindentation. *2006* Available: http://www.nanoindentation.cornell.edu/home_main.htm

[34] M. R. VanLandingham, "Review of instrumented indentation," *Journal of Research of the National Institute of Standards and Technology,* vol. 108, pp. 249-265, 2003.

[35] MTS Systems Corp, "Nano Indenter XP User Manual," 2006.

[36] Xiaodong Li and B. Bhushan, "A review of nanoindentation continuous stiffness measurement technique and its applications," *Mater Charact,* vol. 48, pp. 11-36, 02/. 2002.

[37] Nanotech (nanotech@MTS.com). (2005), RE: NANO SERVICE.

[38] J. Hay. (2004), MEMS testing. 000205_APP MTS Nano Instruments, [Online].

[39] Z. Shao, F. Vollrath, J. Sirichaisit and R. J. Young, "Analysis of spider silk in native and supercontracted states using Raman spectroscopy," *Polymer,* vol. 40, pp. 2493-2500, 1999.

[40] Fukushima Yasumasa. (2000), Secondary structural analysis in the solid state for analogous sequential polypeptides of glycine-rich sequence of spider dragline silk. *Polymer Bulletin* [Online]. *45(3),* pp. 237-244.

[41] R. C. Hibbler, *Mechanics of Materials.* ,4th ed.New Jersey: Prentice Hall, 1999,

[42] R. Saha and W. D. Nix, "Effects of the substrate on the determination of thin film mechanical properties by nanoindentation," *Acta Materialia,* vol. 50, pp. 23-38, 01/08. 2002.

[43] S. Chen, L. Liu and T. Wang, "Size dependent nanoindentation of a soft film on a hard substrate," *Acta Materialia,* vol. 52, pp. 1089-1095, 2004.

[44] T. Y. Tsui, C. A. Ross and G. M. Pharr, "Nanoindentation hardness of soft films on hard substrates: Effects of the substrate," in *Proceedings of the 1997 MRS Spring Symposium, Mar 31-Apr 3 1997,* 1997, pp. 57-62.

[45] O'Hagan, Ryan (MTS Application Engineer). RE: Nano indenter - high load testing method. *E-mail communication*

[46] De Silva,Leandro Macedo Soares, V. Ebacher, D. Liu, H. McKay, T. R. Oxland and R. Wang, "Elasticity and viscoelasticity of human tibial cortical bone measured by nanoindentation," in *2005 Materilas Research Society Spring Meeting, Mar 29-31 2005,* 2005, pp. 91-96.

[47] W. C. Tang, T. -. H. Nguyen, M. W. Judy and R. T. Howe, "Electrostatic-comb drive of lateral polysilicon resonators," in *5th International Conference on Solid-State Sensors and Actuators and Eurosensors III, 25-30 June 1989,* 1990, pp. 328-31.

[48] A. Seidel, O. Liivak, S. Calve, J. Adaska, G. Ji, Z. Yang, D. Grubb, D. B. Zax and L. W. Jelinski, "Regenerated spider silk: processing, properties, and structure," *Macromolecules,* vol. 33, pp. 775-780, 2000.

[49] Z. Yang, O. Liivak, A. Seidel, G. LaVerde, D. B. Zax and L. W. Jelinski, "Supercontraction and backbone dynamics in spider silk: ^{13}C and ^{2}H NMR studies," *J. Am. Chem. Soc.,* vol. 122, pp. 9019-9025, 2000.

[50] J. P. Gong, Y. Katsuyama, T. Kurokawa and Y. Osada, "Double-network hydrogels with extremely high mechanical strength," *Adv Mater,* vol. 15, pp. 1155-1158, 2003.

[51] MIT Open Courseware, Design of Medical Devices and Implants. (2004, Chapter 8.

[52] M. R. J. Gibbs, E. W. Hill and P. J. Wright, "Magnetic materials for MEMS applications," *J. Phys. D,* vol. 37, pp. 237-244, 2004.

[53] Shan Guan, B. J. Nelson and K. Vollmers, "Electrochemical codeposition of magnetic particle-ferromagnetic matrix composites for magnetic MEMS actuator applications," *J. Electrochem. Soc.,* vol. 151, pp. 545-9, 2004.

[54] T. -. Chin, "Permanent magnet films for applications in microelectromechanical systems," in *International Symposium on Advanced Magnetic Technologies (ISAMT'99), 24-25 may 1999,* 2000, pp. 75-9.

[55] J. W. Judy and R. S. Muller, "Magnetically actuated, addressable microstructures," *J Microelectromech Syst,* vol. 6, pp. 249-56, 1997.

[56] H. Ren and E. Gerhard, "Design and fabrication of a current-pulse-excited bistable magnetic microactuator," *Sensors and Actuators A (Physical),* vol. A58, pp. 259-64, 03/. 1997.

[57] Hu, Hans. P. and Chiao, J.C., "A compact fiber optic scanner using electromagnetic actuation," in *2005 TexMEMS, VII International Conference on Micro Electro Mechanical Systems,* 2005,

[58] Hans P. Hu, Kevin D. Le , J.-C. Chiao. An optical scanner based on electromagnetically actuated optical fiber. Presented at Micromachining and Microfabrication Process Technology Conference, Photonics West Symposium.

[59] F. T. Ulaby, *Fundamentals of Applied Electromagnetics.* ,Media Edition ed.New Jersey 07458: Prentice Hall, 2001,

[60] Department of Physics and Astronomy, Georgia State Univ. HyperPhysics. [Online]. Available: http://hyperphysics.phy-astr.gsu.edu/hbase/solids/squid.html

[61] Kasap S.O., *Principles of Electrical Engineering Materials and Devices.* ,Revised Edition ed.USA: McGraw-Hill, 2000,

[62] S. A. Boppart, B. E. Bouma, C. Pitris, G. J. Tearney, J. G. Fujimoto and M. E. Brezinski, "Forward-imaging instruments for optical coherence tomography," *Opt. Lett.,* vol. 22, pp. 1618-20, 11/01. 1997.

[63] Shi-Sheng Lee, E. Motamedi and M. C. Wu, "Surface-micromachined free-space fiber optic switches with integrated microactuators for optical fiber communication systems," in *Proceedings of International Solid State Sensors and Actuators Conference (Transducers '97), 16-19 June 1997,* 1997, pp. 85-8.

[64] K. R. Cochran, L. Fan and D. L. DeVoe, "High-power optical microswitch based on direct fiber actuation," *Sensors and Actuators A (Physical),* vol. 119, pp. 512-19, 04/13. 2005.

[65] M. Herding, F. Richardt and P. Woias, "A novel approach to low-cost optical fiber switches," in *2003 IEEE/LEOS International Conference on Optical MEMS, 18-21 Aug. 2003,* 2003, pp. 141-2.

[66] Shinji Nagaoka. Jan/Feb 1999, Compact latching-type single-mode-fiber switches fabricated by a fiber-micromachinging technique and their practical applications. *IEEE Journal of Selected Topics in Quantum Electronics 5(1),*

[67] E. L. Mayes, F. Vollrath and S. Mann, "Fabrication of magnetic spider silk and other silk-fiber composites using inorganic nanoparticles," *Adv Mater,* vol. 10, pp. 801-5, 07/09. 1998.

[68] W. G. Jenks, S. S. H. Sadeghi and J. P. J. Wikswo, "SQUIDs for nondestructive evaluation," *J. Phys. D,* vol. 30, pp. 293-323, 1997.

[69] J. E. Lenz, "A review of magnetic sensors," *Proc IEEE,* vol. 78, pp. 973-89, 06/. 1990.

[70] Quantum Design. (11/07/2000), Characterization of magnetic noise in superconducting magnets when charging the magnetic field in unidirectional steps. [Online]. Available: http://qdusa.com/search/qdsearch.html

[71] Sypris Test and Measurements. Product instrument information on hall effect Gauss/Tesla meter. [Online]. Available: http://www.sypris.com/stm/content.asp?page_id=726

[72] Cotton F. Albert., Wilkinson Geoffery, *Advanced Inorganic Chemistry.* ,5th ed.USA: John Wiley & Sons, Inc, 1988,

[73] G. Sengolge, W. H. Horl and G. Sunder-Plassmann, "Intravenous iron therapy: well-tolerated, yet not harmless," *Eur. J. Clin. Invest.,* vol. 35 Suppl 3, pp. 46-51, Dec. 2005.

[74] Burke N.A.D., Stover H.D.H., Dawson F.P., Lavers J.D., Jain P.K., and Oka H. (2001, Preparation and characterization of polymer-coated magnetic nanoparticles. *IEEE Transactions on Magnetics 37(4),* pp. 2660-2662.

[75] T. Hyeon, S. S. Lee, J. Park, Y. Chung and H. B. Na, "Synthesis of highly crystalline and monodisperse maghemite nanocrystallites without a size-selection process," *J. Am. Chem. Soc.,* vol. 123, pp. 12798-12801, Dec 26. 2001.

[76] S. Sun, H. Zeng, D. B. Robinson, S. Raoux, P. M. Rice, S. X. Wang and G. Li, "Monodisperse MFe_2O_4 (M = Fe, Co, Mn) Nanoparticles," *J. Am. Chem. Soc.,* vol. 126, pp. 273-279, 2004.

[77] T. Maruyama and Y. Shinyashiki, "Iron-iron oxide composite thin films prepared by chemical vapor deposition from iron pentacarbonyl," *Thin Solid Films,* vol. 333, pp. 203-6, 11/23. 1998.

[78] N. A. D. Burke, H. D. H. Stover and F. P. Dawson, "Magnetic nanocomposites: preparation and characterization of polymer-coated iron nanoparticles," *Chemistry of Materials,* vol. 14, pp. 4752-61, 11/. 2002.

[79] Nakamoto Kazuo, *Infrared and Raman Spectra of Inorganic and Coordination Compounds.* ,5th ed.USA: Joh Wiley & Sons, Inc., 1997,

[80] Quartz Imaging Corporation. Intergrated X-ray microanalysis system for the hitachi S-2600. [Online]. Available: http://www.qrtz.com/xray_02.html

[81] SEAL laboratories. Energy disperse X-ray analysis. [Online]. Available: http://www.seallabs.com/edx.html

[82] A. Armigliato, "Thin film X-ray microanalysis with the analytical electron microscope," *J. Anal. at. Spectrom.,* vol. 14, pp. 413-418, 1999.

[83] M. Saito, T. Aoyama, T. Hashimoto and S. Isakozawa, "Transmission electron microscope sample shape optimization for energy dispersive X-ray spectroscopy using the focused ion beam technique," *Japanese Journal of Applied Physics, Part 1 (Regular Papers, Short Notes & Review Papers),* vol. 37, pp. 355-9, 01/. 1998.

[84]Rymer T.B.,*ElectronDiffraction* USA: Barnes & Nobles, Inc., 1970,

[85] Cowley John.M., *Electron Diffraction Techniques.* , vol. 1, Chester, England: International Union of Crystallography, Oxford University Press, 1992,

[86] C. Mouro, C. Jung, A. Bondon and G. Simonneaux, "Comparative Fourier transform infrared studies of the secondary structure and the CO heme ligand environment in cytochrome P-450cam and cytochrome P-420cam," *Biochemistry,* vol. 36, pp. 8125-8134, Jul 1. 1997.

[87] A. Naidja, C. Liu and P. M. Huang, "Formation of Protein-Birnessite Complex: XRD, FTIR, and AFM Analysis," *J. Colloid Interface Sci.,* vol. 251, pp. 46-56, Jul 1. 2002.

[88] K. Onoda, H. Mino, Y. Inoue and T. Noguchi, "An FTIR study on the structure of the oxygen-evolving Mn-cluster of Photosystem II in different spin forms of the S(2) state," *Photosynth Res.,* vol. 63, pp. 47-57, 2000.

[89] M. J. Clarke, A. I. Cooper, S. M. Howdle and M. Poliakoff, "Photochemical reactions of organometallic complexes impregnated into polymers: Speciation, isomerization, and hydrogenation of residual alkene moieties in polyethylene," *J. Am. Chem. Soc.*, vol. 122, pp. 2523-2531, 2000.

[90] J. M. Parnis, M. G. K. Thompson and L. M. Ashenhurst, "Matrix Isolation of Electron Bombarded Gases Containing $Fe(Co)_5$: An FTIR Absorption Study of Neutral and Anion Decomposition Products," *Journal of Physical Chemistry A,* vol. 107, pp. 7390-7395, 2003.

[91] H. -. Jin, J. Park, R. Valluzzi, P. Cebe and D. L. Kaplan, "Biomaterial Films of *Bombyx Mori* Silk Fibroin with Poly(ethylene oxide)," *Biomacromolecules,* vol. 5, pp. 711-717, May. 2004.

[92] D. Huemmerich, U. Slotta and T. Scheibel, "Processing and modification of films made from recombinant spider silk proteins," *Applied Physics A: Materials Science and Processing,* vol. 82, pp. 219-222, 2006.

[93] F. Junghans, M. Morawietz, U. Conrad, T. Scheibel, A. Heilmann and U. Spohn, "Preparation and mechanical properties of layers made of recombinant spider silk proteins and silk from silk worm," *Applied Physics A: Materials Science and Processing,* vol. 82, pp. 253-260, 2006.

[94] Moskowitz Bruce. M., *Global Earth Physics, A Handbook of Physical Constants.* American Geophysical Union, 1995.

[95] Innovation Center (2004), Continuous Dynamic Analysis and Quasi-static Measurements of spider silk, Application note 000207_APP, MTS Nano Instruments, [Online].

[96] L. Li, F. Yan and G. Xue, "Preparation of a porous conducting polymer film by electrochemical synthesis-solvent extraction method," J Appl Polym Sci, vol. 91, pp. 303-307, 2004.

[97] M. N. A. Karlsson, K. Deppert, B. A. Wacaser, L. S. Karlsson and J. -. Malm, "Size-controlled nanoparticles by thermal cracking of iron pentacarbonyl," Applied Physics A: Materials Science and Processing, vol. 80, pp. 1579-1583, 2005.

[98] Wikipedia Contributors. Wikipeida, the free encyclopedia. [Online]. 2006(June/21), Available: http://en.wikipedia.org/wiki/Iron_(III)_oxide

[99] Yong Zhang, Luru Dai and Zhong-Can Ou-Yang, "Amino acid composition-dependent elasticity of spider silk," in Progress in Statistical and Nonlinear Physics: Proceedings of the First Cross Taiwan-Strait Conference on Statistical Physics, 26-31 Aug. 2004, 2004, pp. 2516-22.

[100] S. Simon, A. Gil, M. Sodupe and J. Bertran, "Structure and fragmentation of glycine, alanine, serine and cysteine radical cations. A theoretical study," Journal of Molecular Structure: THEOCHEM, vol. 727, pp. 191-197, 2005/8/16.

[101] X. Sun and X. Dong, "Magnetic properties and microstructure of carbon encapsulated Ni nanoparticles and pure Ni nanoparticles coated with NiO layer," Mater. Res. Bull., vol. 37, pp. 991-1004, 2002.

APPENDIX A SEM images

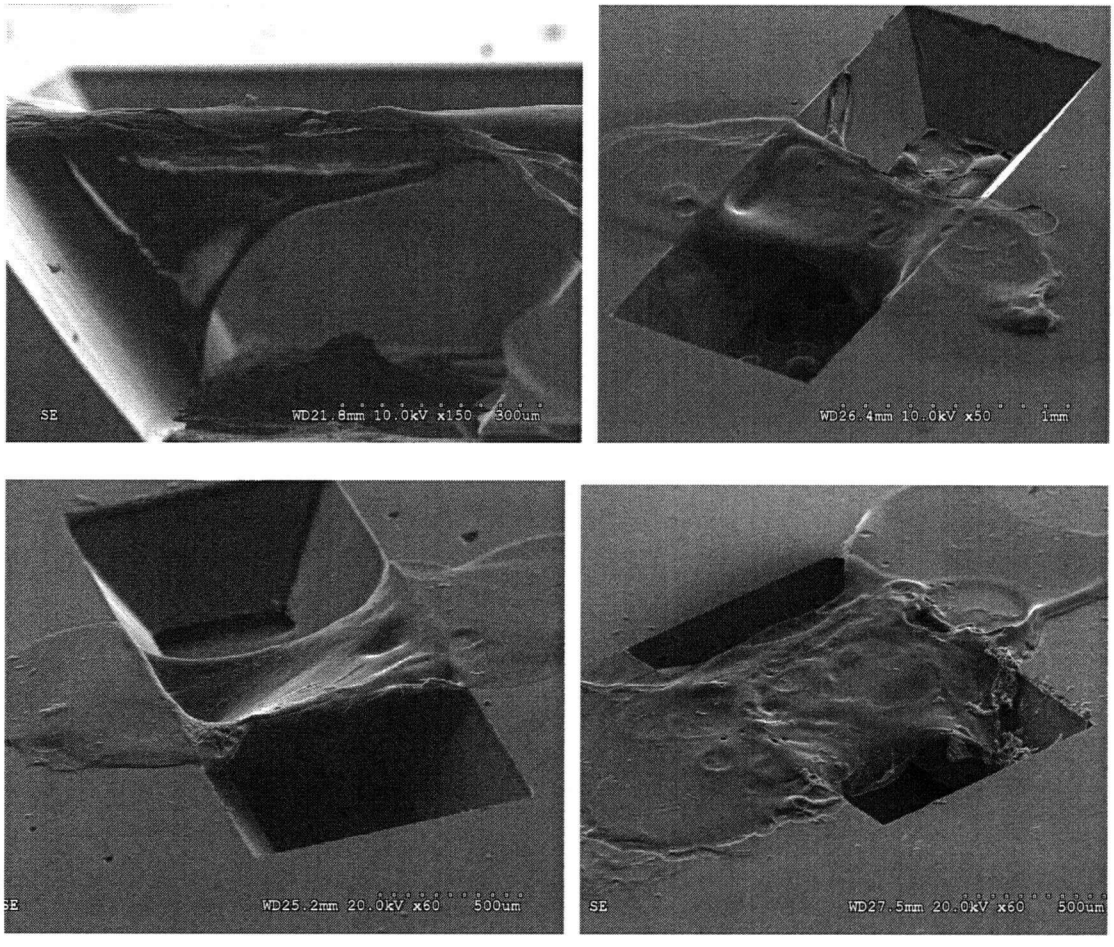

Figure 56: SEM images of beams that was not successfully fabricated. Top left: cross sectional view, estimate for thickness of the film. The rest are images of 3 separate failed attempts.

APPENDIX B Inkjet Setup

The following report is written by Ramin Saheb-Djawaher and revised by myself. Ramin was a summer student who worked on the inkjet project. He was instrumental in setting up and carrying out the experiments.

B1 Summary

This report presents and explains the inkjet setup.

The Inkjet setup involved:

- Usage of a Microfab inkjet nozzle with a 50 um orifice
- Installation of calipers onto the probe-station's XY table
- Machining a adjustable moving holding component for holding the nozzle
- Making the drive electronics for the inkjet nozzle
- Determining experimental parameters to run the inkjet nozzle

The Wire bonding machine involved:

- Learning controls and operation procedures
- Determining experimental parameters for Copper, Gold and Titanium
- Usage of a raw circuit board as the base for attaching the chips and wire bonded them

B2 Inkjet Setup

Inkjet setup was made to deposit a thin layer of Spider Silk on top of a free hanging beam. The beams was designed and fabricated through MUMPS process. Using our inkjet setup we managed to make drop-wise deposition with an accuracy of 50μm. A summary of the information we gathered on inkjet systems is given here. The focus will be issues that are not covered in Microfab's inkjet manual or their website.

B2.1 Background on Inkjet Nozzles

The following is a summary of the Microfab's technical notes found in: www.microfab.com/equipment/technotes.html

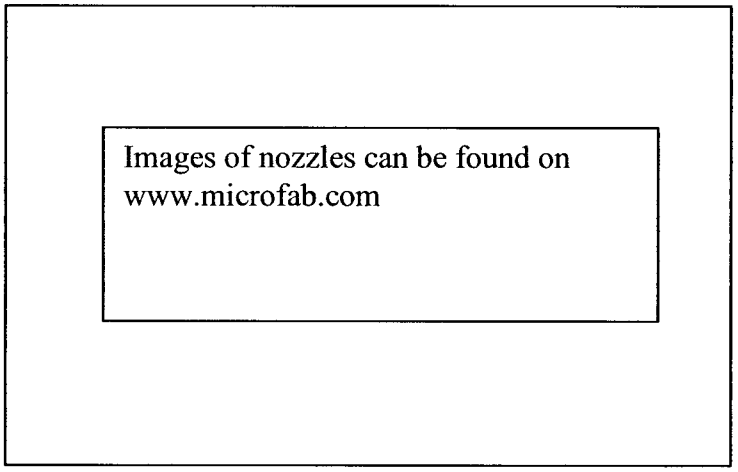

Figure 57: Microfab's Inkjet Nozzles

In Inkjet nozzles, a volumetric change in the fluid is induced by the application of a voltage pulse to a piezoelectric material that is coupled, directly or indirectly, to the fluid. This volumetric change causes pressure/velocity transients to occur in the fluid and these are directed so as to produce a drop that issues from an orifice. Since the voltage is applied only when a drop is desired, these types of systems are referred to as drop-on-demand, or "demand mode." (See Figure 57)

We used the nozzle in Drop-on-Demand (DOD) mode by applying an almost square wave pulse to the nozzle's input. The output is a drop of polymer 50μm in diameter shot at a velocity about 2-3 m/s. This nozzle is compatible with fluids that has a viscosity of 0.5-40 cp (Newtonian) and a surface tension of 20-70 dy/cm. The higher the viscosity and surface tension, the higher a voltage one needs to apply to the nozzle. Too high a voltage would introduce "satellites" in the drop formation. (See Figure 58 below)

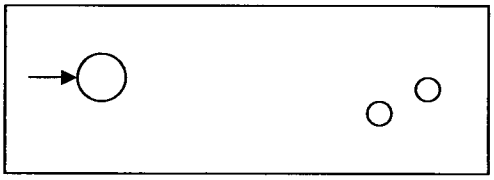

Figure 58: Satellite Formation

Variation of density does not directly affect the performance of a fluid in a demand mode ink-jet device, but it usually indicates a variation of acoustic speed and/or bulk modulus of the fluid,

both of which affect the optimum waveform timing and amplitude requirements. In practice, density, acoustic speed, and bulk modulus effects are minor.

Surface tension has a small effect on the drive voltage requirements for a device. As surface tension increases, the drive voltage required to achieve a constant drop velocity will increase. Very low surface tension can result in an increased likelihood of air ingestion, particularly at high drop velocities.

Things to note

When setting up the nozzle, the glass tip must be handled with extreme care as it is very fragile. The tip can be easily broken if the glass tip touches the bottom of the fluid reservoir during the cleaning process (backwashing). After the nozzle is properly set up as mentioned in the next section, one can make sure that the nozzle is functional by pushing some fluid through. When it is not clogged, the fluid sprays out as a *straight* and very thin line of drops. There might be some resistance while pressing on the syringe. This is completely normal; however, not too much pressure should be applied as it could shoot out the nozzle fitting from the syringe. Too much pressure might also damage the inkjet nozzle. If the drops exit the nozzle at an angle or if a lot of pressure is needed to make the fluid go through the nozzle, one can suspect that the nozzle is clogged.

It is extremely important to have a clean (filtered with 5um syringe filter) solution, otherwise the particles inside the solution would cause the nozzle to "clog". Volatile and sticky solutions are also particularly hard to deposit since the solution forms a barrier at the tip of the nozzle. To overcome problems with clogging, read the cleaning procedure on http://www.microfab.com/equipment/guide/mj_guide.html#cleaning. To overcome problems with volatile/sticky solutions, either dip the nozzle's glass tip in the same solution when idling or wipe the glass tip with a clean sheet of paper. In case the nozzle is clogged badly, look at the glass tip under a microscope. Most likely, one can see the jammed particles at the very tip. These particles can be removed using a thin (less than 50μm) gold wire (taken from the wire bonding machine) which is then pushed inside the nozzle's exit tip. The nozzle should then be backwashed for a couple of minutes. The capillary glass inside the aluminum casing can be

cleaned using a syringe cleaning wire. This wire can be directly pushed into the nozzle from the fluid entrance.

For testing purposes, Isopropyl Alcohol (IPA) is suggested. IPA can safely be used to clean the nozzle as well. If dye needs to be added to desired solution, be sure to filter the solution and shake it before use.

B2.2 Holding Setup

The Inkjet nozzle is attached to an aluminum fitting that connects it to a syringe (the fluid reservoir). The magnetic base holder holds the fitting in a vertical manner and is positioned on the microscope's work bench. This configuration can is illustrated in Figure 59.

Figure 59: Holding Setup

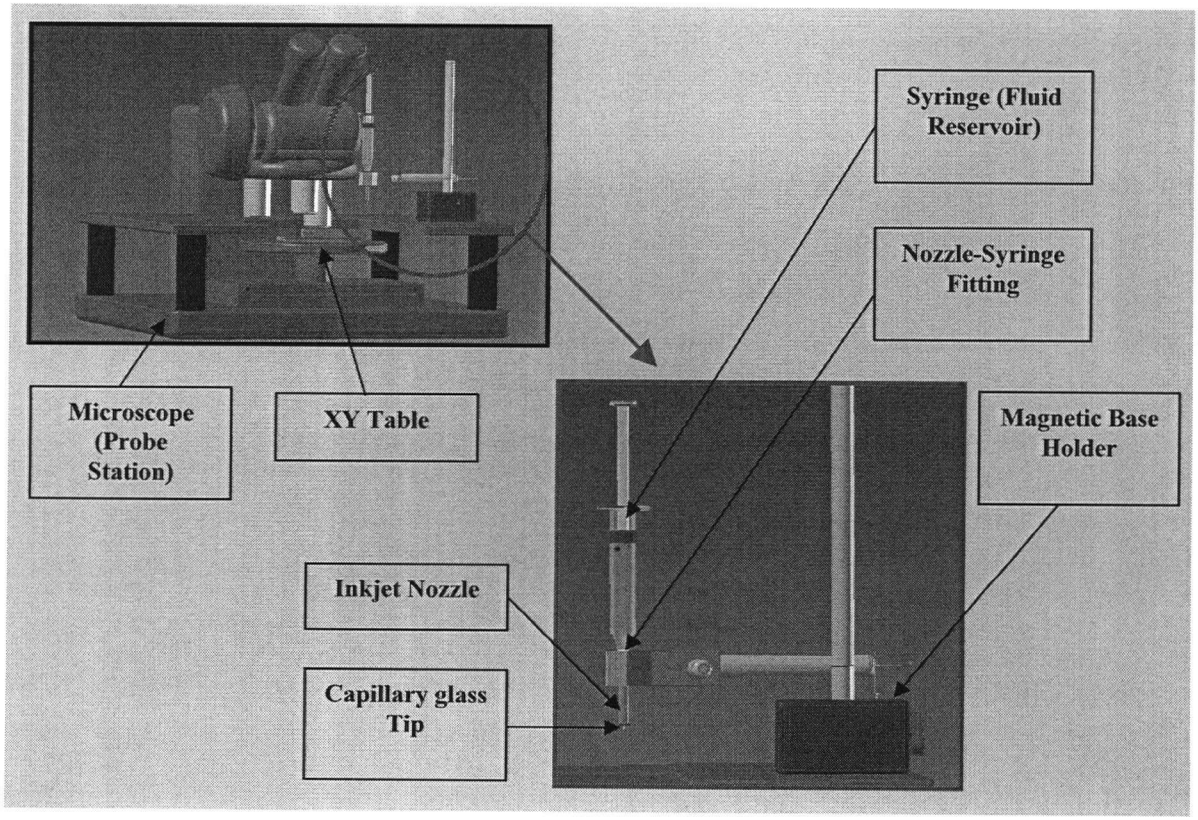

The fluid fitting can be connected to the magnetic base via a tweezers-shaped part. The tweezers-shaped part can be opened or closed by manipulating the bolt in the center.

B2.3 Electrical Setup

The electrical setup consists of a signal generator, amplifier, oscilloscope and power supply. The desired wave form generated by the signal generator is amplified by a factor set by the power supply voltage; the resultant amplified signal can then be observed on the oscilloscope.

To run the inkjet nozzle, a waveform depicted below must be supplied as described in the nozzle's user manual. See Figure 60 below. In our setup, we only used the positive (bold lines) side of the signal since the negative portion has not significant effects (as suggested by Microfab).

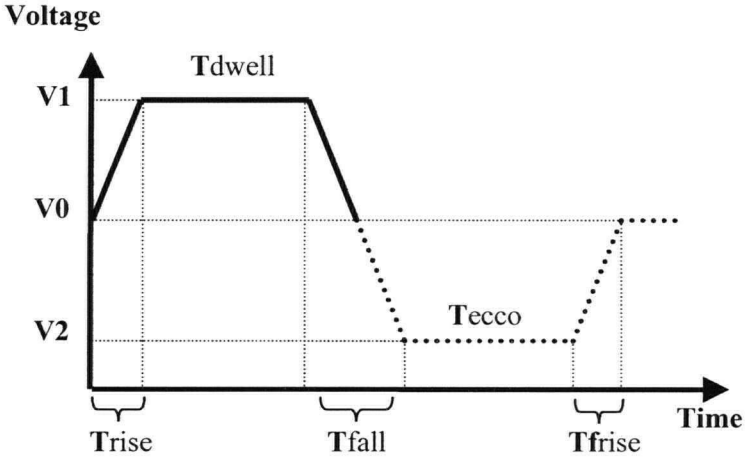

V1	0 to 100 Volts
V2	-100 to 0 Volts
Trise	1 - 300 µs
Tdwell	3 - 800 µs
Tfall	1 - 150 µs
Tecco	3 - 800 µs
Tfrise	1 - 300 µs
Frequency	1Hz – 20 KHz

Figure 60 : Signal Waveform

The *Sensortech* SA- 10 amplifier is too slow for operation of this nozzle, so we had to design an amplifier with higher bandwidth.

The datasheet of the nozzle indicates that the rise time should be 5 µsec for a 50 Volts voltage rise. So, a slew rate of 10 V/µsec is required. According to *Sensortech*, the slew rate of the SA-10 amp is 3.8 V/µsec. The custom amplifier which utilizes a Fairchild TIP 122 Darlington transistor has a much higher slew rate of 25 V/µsec, which is more than sufficient. The schematic of the custom amplifier is given below (Figure 60). As you can see, this is not the usual way to connect a this type of transistor. This amplifier works well for high voltage and high impedance loads (small capacitive loads like the inkjet nozzle) and is quite non-linear. It is

designed to handle only square waves; however, it would amplify linearly if the input amplitude is small. Remember that you need to input the inverted signal to the amplifier.

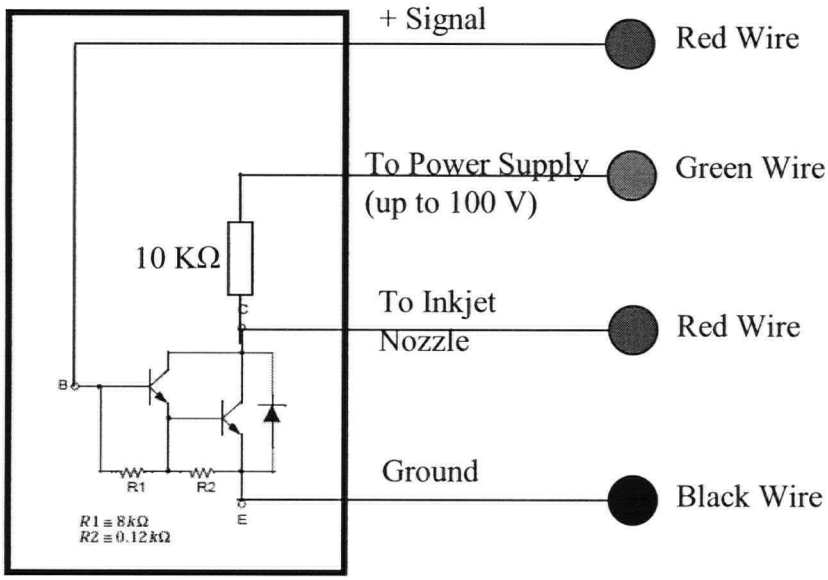

Figure 61: Custom Amplifier

The whole wiring of electrical setup is depicted below:

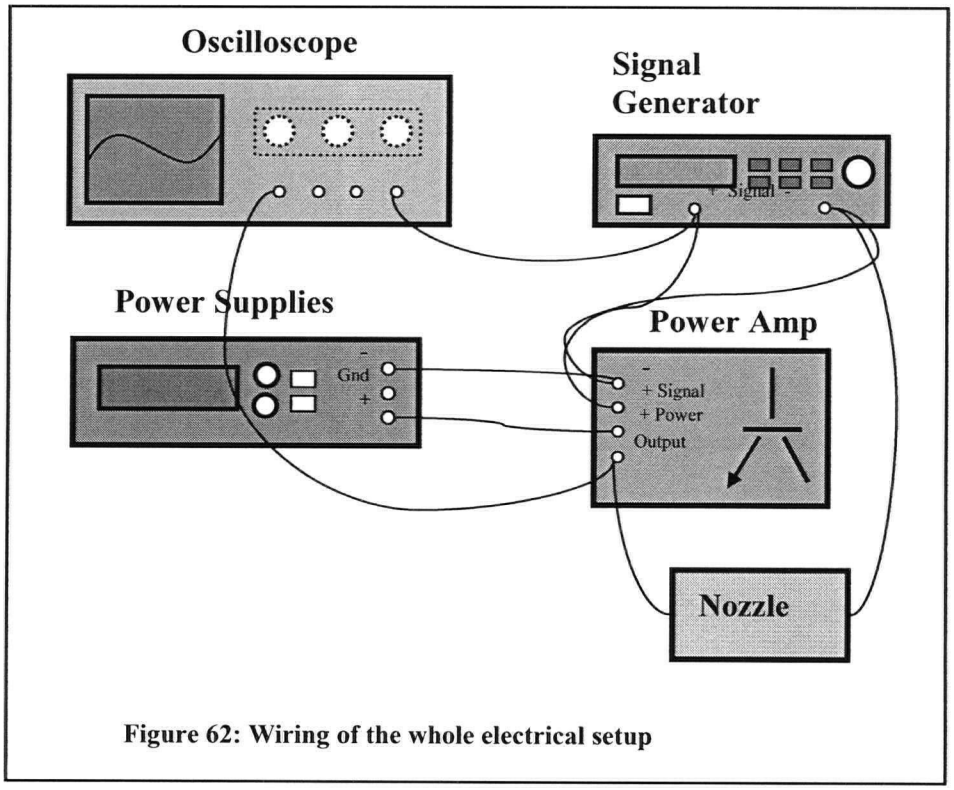

Figure 62: Wiring of the whole electrical setup

Some performance graphs are depicted below:

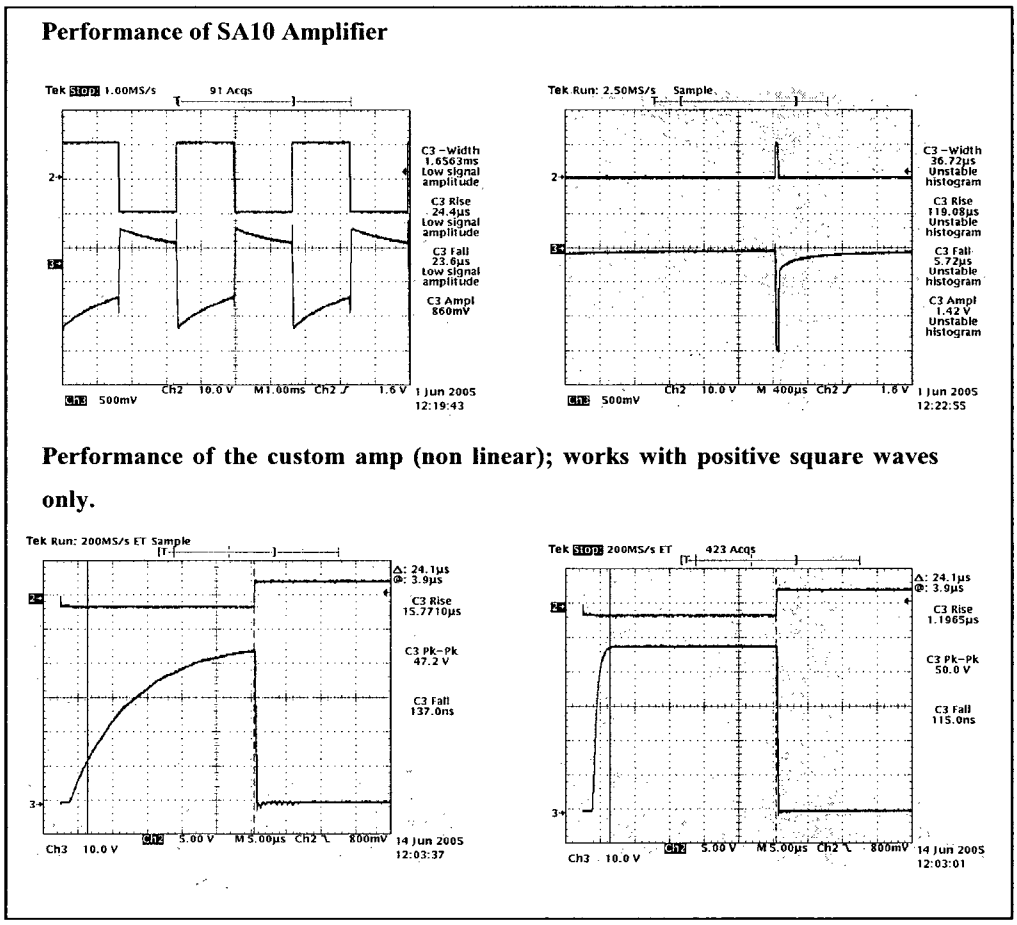

Figure 63: Performance graph of the amplifier

The input form has the following characteristics:

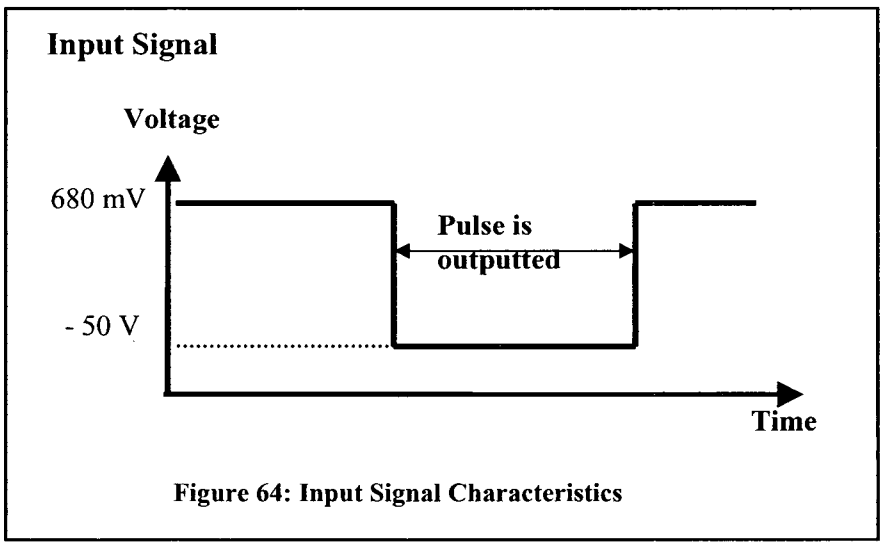

Figure 64: Input Signal Characteristics

B2.4 Positioning with Calipers

Since our setup is just a prototype, the design of the positioning table based on inexpensive commercial components. There is a pretty accurate positioning table installed on the probe station, so all I needed was a means to measure the position. Two digital calipers were purchased from EBay (cost: 60$ for both) and they were attached to the positioning table. The calipers are accurate to 25.4 μm (10μm resolution) in each direction. In order not to damage the Probe Station, we super glued the calipers to the positioning table. When using the positioning table of the probe station, be sure not to push the table out of the calipers limits since this would damage the calipers. Remember to turn off the calipers after each use.

B2.5 Operation Sequence

Follow the give sequence below to run the inkjet nozzle:

1. Go through the cleaning procedure to make sure that the nozzle is clean. Attach the inkjet nozzle to the threaded side of the Aluminum fitting.
2. Make desired solution, which must be homogenous and *filtered.*
3. Using a syringe, take at least 0.2 mL of the solution. Connect the syringe to the Aluminum fitting and then attach it to the magnetic stand. Position the magnetic stand on the Probe Station so that it doesn't interfere with the microscope's instruments/controls.
4. While the inkjet nozzle disconnected from electrical power, push on the syringe to see if a straight line of drops is shooting out of the nozzle's tip. If you have a hard time seeing the drops, hold a piece of clean paper under the nozzle; you should be able to see the wetted areas. Wait until the pressure is reduced and the nozzle stops shooting out drops. If you can not see drops, go through the cleaning procedures to make sure that the nozzle is not clogged.
5. Turn on the signal generator, power supply and oscilloscope. Make sure the wires are connected properly as mentioned in the "Electrical Setup" section. Choose desired wave form on the signal generator (can use saved settings) and check if the desired output is seen on the scope.
6. Attach the output wires of the amplifier to the inkjet nozzle. You should hear the sound of the nozzle vibrating. By holding a small piece of paper under the nozzle one can see if it is depositing. If it is depositing, make necessary voltage and pulse width adjustment to

get the drops to hit on the same spot. If it is not depositing, change voltage and the pulse width of the power supply; wipe the tip of the nozzle every time you change the settings. Jumping to different frequencies also helps to get the nozzle to deposit.

7. Turn on the calipers and reset them.
8. Switch the signal generator to burst mode (20 drops at each trigger event) and put a microscope slide (sample glass slide) on the positioning table. Hit the 'trigger' button of the signal generator a few times. Try to find the center of the drops under the microscope. Note down the calipers' measurements. Now, every time you need to deposit at a specific spot, just find it under the microscope and then move it back under the nozzle by the measurements written down. Now, the nozzle would deposit on the desired spot.
9. After you are done with the nozzle, clean the nozzle as well as the Aluminum fitting.

B2.6 Experimental Parameters

Experiments with IPA revealed the following:

Freq	318 Hz
Pulse Width	33 μsec
Voltage	63 Volts at power supply

Experiment with 0.5% w/w spider silk in HFIP revealed the following:

Freq	318 Hz
Pulse Width	53 μsec
Voltage	77 Volts

Figure 64 shows some snapshots of sample inkjet drops on a microscope glass slide.

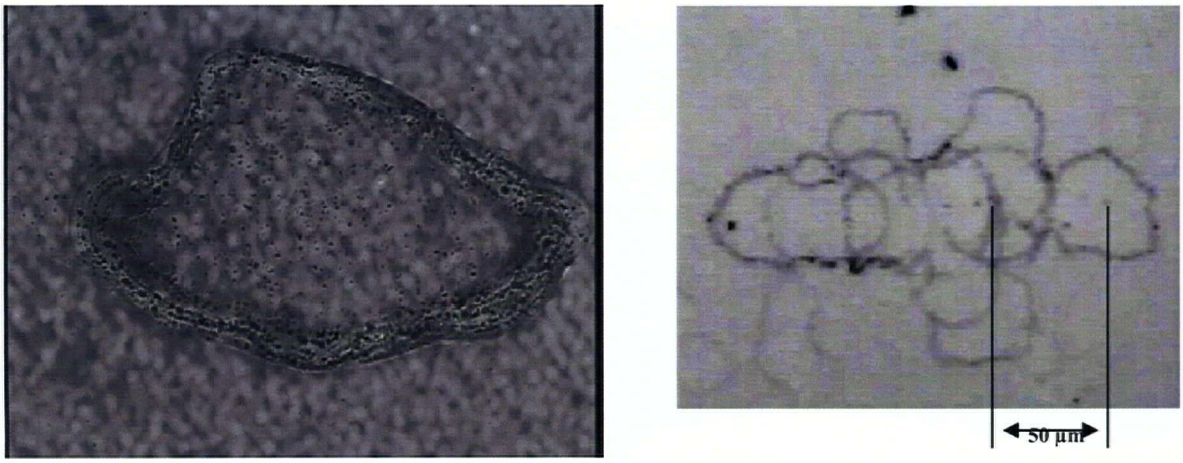

Figure 65: Snapshots of sample inkjet drops. Left: Snapshots of 800 drops of spider silk deposited over a length of 200 um (10 drops at each 10 um for four times) Right: Eight single IPA drops distanced 50 um from each other. From this snap shot we concluded that the drops are 50 um in diameter.

The original goal of the project is to deposit the spider silk on to cantilever beams shown in Figure 66. However, spider silk clog very quickly as it is allowed to be in contact with air. Therefore, large amount of raw spider silk is required to optimize the parameters involved in the experiments. Therefore, this study was terminated. However, as shown in Figure 65, drop can be successfully made from ink drop methods, it is a matter of optimization and abundance of resource before it can be successfully performed. Figure 66 is a picture of the wired bonded cantilever beams.

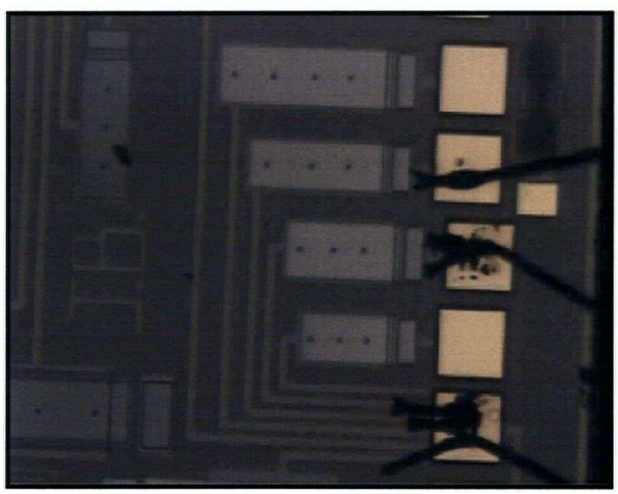

Figure 66: Wire Bonding Sample Picture

APPENDIX C

Magnetic Unit Conversions

Table 14: Magnetic conversion factors

Magnetic Term	Symbol	SI unit	CGS Unit	Conversion Factor
Magnetic induction	B	Tesla (T)	Gauss (G)	I T = 10^4 G
Magnetic Field	H	Am^{-1}	Oersted (Oe)	1 A m^{-1} = 4π x 10^{-4} Oe
Magnetization	M	Am^{-1}	Emu cm^{-3}	1 Am^{-1} = 10^{-3} emu cm^{-3}
Magnetic polarization	J	T	G	1 T = $10^4/4\pi$ emu cm^{-3}
Magnetic moment	m	Am^2	Emu = G cm^3	1 Am^2 = 10^3 emu
Magnetic moment per unit mass	σ	Am^2kg^{-1}	Emu g^{-1}	1 Am^2kg^{-1} = 1 emu g^{-1}

Information within this table is obtained from *A hand book of physical constants.* [94]

APPENDIX D

Iron wt% Calculation for Iron Spider Silk Solution

Given 100 ml of final mixed solution of 1:1 v/v dilution, 50 ml will be 1% w/w spider silk, and the other 50% will be $Fe(CO)_5$. Since spider silk mass is only 1%, we can approximate the 50 ml of spider silk solution to be pure HFIP.

Total mass of 50 ml of HFIP = 50 cc x 1.596 g/cc = 79.8 g

Relative density of $Fe(CO)_5$ is 1.5.
Total mass for $Fe(CO)_5$ = 1.5 g/cc x 50 cc = 75 g

Molar mass of $Fe(CO)_5$ is 195.9 g/mol. Molar mass of Fe is 56.
Therefore iron wt% in $Fe(CO)_5$ = 56/195.9 = 28.59%

Iron content in the final solution = 28.59% x 75g = 21.44 g
Finally, iron wt% in the final solution = 21.44 / (75 + 79.8) = 13.9%